

ISSN 1913-1844 (Print)
ISSN 1913-1852 (Online)

MODERN APPLIED SCIENCE

**Vol. 4, No. 3
March 2010**



Canadian Center of Science and Education®

Editorial Board

- Abdul Talib Bon Universiti Tun Hussein Onn Malaysia, Malaysia
- Ahmad Mujahid Ahmad Zaidi Universiti Tun Hussein Onn Malaysia, Malaysia
- Alessandra Crosato Delft University of Technology, the Netherlands
- Guy L Plourde University of Northern British Columbia, Canada
- J S Prakash Sri Bhagawan Mahaveer Jain College of Engineering, India
- Jiantao Guo The Scripps Research Institute, United States
- Justin Madigan Intel, United States
- K.V. Ramana Rao University of Rajasthan, India
- Lim Hwee San Universiti Sains Malaysia, Malaysia
- Musa Mailah Universiti Teknologi Malaysia, Malaysia
- Panagiotis Vlamos Ionian University, Greece
- Peter Kusch Bonn-Rhein-Sieg University of Applied Sciences, Germany
- Rajiv Pandey Indian Council of Forestry Research and Education, India
- Sarhan Musa Prairie View A&M University, United States
- Srikanth Pilla Stanford University, United States
- Stefanos Dailianis University of Patras, Greece
- Suchada Chanprateep Chulalongkorn University, Thailand
- Sujatha. C.H Cochin University of Science and Technology, India
- Susan Sun Canadian Center of Science and Education, Canada
- Sutopo Hadi University of Lampung, Indonesia
- Thomas Schwengler Qwest Communications and University of Colorado, United States
- Wichian Sittiprapaporn Mahidol University, Thailand
- Xin Fei Lawrence Berkeley National Laboratory & University of Utah, United States



Contents

Electrochemical Oxidation of Sulfide Ions on Platinum Electrodes <i>F. M. Al Kharafi, A. Y. Saad, B.G. Ateya & I.M. Ghayad</i>	2
Analysis and Supplement with the Mechanism of Electrosynthesizing Benzofuran Derivatives <i>Yunhui Li, Jie Zhou, Xiuxia Gao, Feifei Wang & Yupeng Wang</i>	12
Isotope Technique (^{14}C , ^{131}I) for Safety Analysis of Domestic Solid Waste Disposal Site in Jakarta, Indonesia- A Case Study <i>Syafalni, I. Abustan & M. Tadza Abdul Rahman</i>	20
Positioning Control of Unmanned-plane based on Regional Feature Matching <i>Jianghong Li, Liang Chen & Yuanhu Cai</i>	28
Retrieval of SST Algorithm Coefficients at South China Sea <i>Ng Hou Guan, Mohd. Zubir Mat Jafri & Khiruddin Abdullah</i>	34
Predicting Model of Traffic Volume Based on Grey-Markov <i>Yinpeng Zhang</i>	46
Studies on Some Aspects of Jet Mixers I: Hydrodynamics <i>K.Saravanan, N. Sundaramoorthy, G. Mohankumar & N. Subramanian</i>	51
The Operator of Genetic Algorithms to Improve its Properties <i>Aijun Li</i>	60
Induction Sintering of %3 Cu Contented Iron Based Powder Metal Parts <i>Uğur ÇAVDAR & Enver ATİK</i>	63
Comparison of Two Different Yarn Evenness Test Methods <i>Dairong Zhang & Ling Cheng</i>	71
Application of Artificial Neural Networks for Emission Modelling of Biodiesels for a C.I Engine under Varying Operating Conditions <i>R.Manjunatha, P. Badari Narayana & K. Hema Chandra Reddy</i>	77
Optimal Solutions of Production Inventory Control Problem <i>Zhiguang Zhang</i>	90
The Study of X-Ray Fluorescence Spectrum of Potsherd in New Stone Age in Zhaotong <i>Kunli Fu, Changfen Ding, Qiao Lu, Delan Wu & Bocheng He</i>	95
Development of Multi-Purpose Nonwoven Filter Medium for Automobile <i>Binghui Wang</i>	99
Bohr Theory in the Atomic Physics <i>Haiyan Li</i>	106
Control on Pore Structure and Strength of Tubular Carbon Membrane by Introducing Additives <i>Lijie Liu & Yong Tan</i>	110



Electrochemical Oxidation of Sulfide Ions on Platinum Electrodes

F. M. Al Kharafi, A. Y. Saad, B.G. Ateya & I.M. Ghayad (Corresponding author)

Chemistry Department, Faculty of Science, Kuwait University, Kuwait

P.O. Box: 5969, Safat 13060, Kuwait

Tel: 96-5-2498-7142 E-mail: ighayad@yahoo.com

The research is funded by Research Administration of Kuwait University, Grant Numbers SC04/04.

Abstract

This paper treats the electrochemical oxidation of sulfide ions on platinum using cyclic voltametry. An electrolyte of 3.5% NaCl containing sulfide ions was used as the testing medium. The effects of scan rate, concentration of sulfide ions and temperature on the cyclic voltamograms were investigated.

Cyclic voltamograms show small currents in the absence of sulfide ions. In the presence of sulfide ions, the magnitude of the anodic currents in the forward sweep is much more than these in the reverse sweep. Cyclic voltamograms show three features appear in the forward sweep at potentials of -0.1, 0.475 and 1.0 V vs Ag/AgCl, respectively. Peaks currents are increased upon the increase of either the scan rate or temperature. These peaks are explained to show the possible formed species and the possible electrochemical oxidation reactions at the electrode surface.

Keywords: Electrochemical oxidation, Platinum, Sulfide ions, Cyclic voltametry

1. Introduction

Hydrogen sulfide, H₂S, is a dangerous pollutant that promotes the corrosion of metallic materials and is toxic to humans. It is listed by the Environmental Protection Agency as an extremely hazardous (U.S. Environmental Protection Agency 1988). It contaminates massive volumes of natural water bodies and industrial waste water streams [Radford et al., 1994; Luther III et al., 1989; Cutter et al., 1989; Xu et al., 2000; Cutter et al., 1999]. A prominent example of a sulfide polluted natural water body is the geothermal fluids that encountered during the drilling of wells for the production of oil and gas and for the recovery of geothermal energy (Darely et al., 1988; Garverick 1994; Kagel 2008; Clauser 2006). Various lines of treatment have been proposed for the removal of sulfide ions from contaminated waters, including biological treatment (Park 2008)], adsorption (Daley et al., 1997), oxidation (Anani et al., 1990; Miller et al., 2005). Electrochemical desulfurization (oxidation) of these contaminated waters provides an environmentally friendly alternative, in view of the fact that it utilizes electrons instead of chemicals.

The electrochemical oxidation of sulfide ions has been the subject of much interest in connection with the possible use of H₂S as a fuel in fuel cells (Li, et al. 2006), the current and potential oscillations occurring during electrochemical oxidation (Chen et al., 2004; Miller et al., 2005, Miller, et al. 2006), gas sensors (Mohtadi, et al. 2005), wastewater (Ateya et al., 2007; Ateya et al., 2009) ...etc. Anodic oxidation of sulfide ions can yield a variety of products e.g. elemental sulfur, polysulfide, thiosulfates and sulfates. Determination of the selectivity of anodic reactions and the concentrations of formed species are major tasks that are yet to be achieved.

The objective of this work is to study the electrochemical oxidation of sulfide ions on polycrystalline platinum electrode using cyclic voltametry.

2. Experimental

2.1 Corrosion cell and electrodes

Measurements were performed using a double jacketed polarization cell (100 ml) with an Ag/AgCl reference electrode (E = 0.197 V (SHE)) and a platinum wire counter electrode. The working electrodes were polycrystalline platinum sheets of thickness 0.25 mm (Alfa, 99.99%) with rectangular shape and an area of 1.5 cm². The exposed surface of each electrode was polished successively down to 0.3 and 0.05 μm alumina and cleaned for using acetone in an ultrasonic bath for 10 min. All The potential of the working electrode was scanned from cathodic towards anodic potentials using a Gamry (PC4/750 Potentiostat/Galvanostat/ZRA).

2.2 Chemicals and reagents

Measurements were performed in an electrolyte of 3.5% (0.58 M) NaCl containing different concentrations of sodium sulfide. This supporting electrolyte maintains the ionic strength of the electrolyte nearly constant and hence minimizes double layer effects on the kinetic parameter. The test solutions were prepared from deionized water, NaCl (BDH) and Na₂S (BDH). The concentration of sulfide ions was determined iodometrically. In view of the values of pK₁ and pK₂ of H₂S (7 and 14, respectively), the predominant species in this electrolyte is HS⁻ at pH values from 9 to 12. The temperature of the test electrolyte was controlled by flowing hot water around the cell through its double jacketed walls.

2.3 Testing methods

The platinum electrodes were tested using cyclic voltametry method. The potential of the working electrode was scanned from cathodic towards anodic potentials using a Gamry (PC4/750 Potentiostat/Galvanostat/ZRA). Potentiostatic experiments were also performed. The electrodes surfaces were examined using an X-ray photoelectron spectrometer, FISONS Instruments, Model ESCA–Lab 200 (VG Instruments).

3. Results and Discussion:

Cyclic voltammograms of polycrystalline platinum were measured in 3.5% NaCl solution in the absence and in the presence of sulfide ions. Measurements were carried out under different conditions of sulfide ion concentrations, scan rates and temperatures. Results are presented below.

3.1 Effect of sulfide ion

Figure (1) illustrates the cyclic voltammogram (CV) of the platinum electrode in the absence and in the presence of sulfide ions. The range of potentials for this CV was chosen to avoid hydrogen and oxygen evolution. This figure reveals some important features:

- 1) The anodic currents measured in the absence of sulfide ions are negligibly small compared to those measured in its presence, at all potentials. This indicates that the anodic currents shown in figure (1) are indeed resulting from the oxidation of the sulfide ions.
- 2) In the presence of sulfide ions, only anodic currents are measured in the forward sweep while the magnitude of currents in the reverse sweep is negligibly small. This indicates that the products of the anodic reaction in the forward sweep do not undergo reduction in the reverse sweep and have passivated the platinum surface.
- 3) Three features appear in the forward sweep, marked a, b and c at potentials of -0.1, 0.475 and 1.0 V, respectively. While features a and c are readily defined, feature b is less clear.

As can be noticed from figure (2) which represents a consecutive CV's of platinum electrode in a solution of 3.5% NaCl containing 0.15 M HS⁻ at scan rate 10 mV s⁻¹ and 25°C, the value of the current of the first peak is not changed indicating that the formed layer at this potential is not affected markedly by the number of cycles. While the second peak markedly decreased, which may be due to the consuming of active species nearby the surface of the working electrode stepwise and at the mean time, the platinum surface was passivated at the first cycle and its electrochemical ability was decreased due to more sulfur formed at this potential (b). This is also the reason for the disappearance of the peak (c), which is related also to the formation of sulfur species.

Figure (3) illustrates the effect of sulfide ion concentration on the cyclic voltammogram of platinum electrode in 3.5% NaCl at room temperature. The formations of three peaks were gradually disappeared by decreasing the HS⁻ concentration and the appearance of the well defined reduction peak in the reverse direction was noticed. In this case the passivity of platinum electrode was decreased by the gradual decrease of HS⁻ ion concentration.

3.2 Effect of scan rate

Figure (4) illustrates the effect of the scan rate on the cyclic voltammograms of polycrystalline platinum in 3.5% NaCl solution containing 0.15 M HS⁻. It can be noted that there are increases of the values of all peaks current (I_p) with the increase of scan rate (ν). The scan rate dependence of all peaks current, I_p, and peaks potential, E_p, are shown in Figures (5-6), respectively. There is a linear relationship in the plots between I_p versus ν^{1/2} and I_p versus log ν which indicates that the oxidation reaction involves an irreversible electron transfer and is under diffusion control (Ateya et al., 2007).

3.3 Effect of temperature

Figure (7) shows the effect of temperature on the cyclic voltammograms of poly crystalline platinum in 3.5 % NaCl solution containing 0.15 M HS⁻ at a scan rate 10 mVs⁻¹. As can be seen, all peaks currents are increased due to the increasing of the rate of the oxidation reaction. Furthermore, the three peaks are formed at less positive potential values i.e. more readily to be occurred.

Arrhenius plots of the results shown in figure (7) are displayed in figure (8). The Arrhenius equation for many electrode reactions in aqueous solutions is given below (Laidler 1993):

$$i = A \exp(-\Delta H^\ddagger/RT) \quad (2)$$

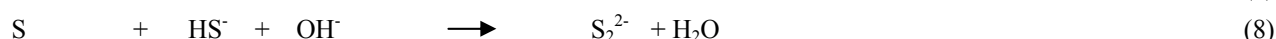
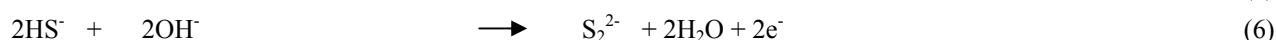
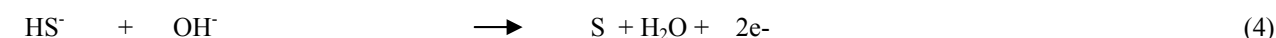
where ΔH^\ddagger is the enthalpy of activation and A is the pre-exponential factor, which includes the entropy of activation, ΔS^\ddagger , since the free energy of activation is related to ΔS^\ddagger by this equation: $\Delta G^\ddagger = \Delta H^\ddagger - T\Delta S^\ddagger$, then equation 2 becomes:

$$i = A \exp(-\Delta G^\ddagger/RT) \quad (3)$$

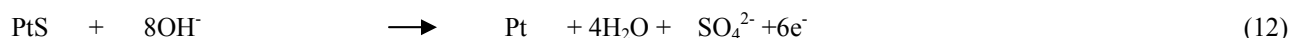
From the slope of straight lines in figure 8, ΔG^\ddagger can be measured for each peak. ΔG^\ddagger values of 12.7, 9.23 and 11.37 KJ mol⁻¹ are obtained for the first, second and third peaks respectively. The low values of ΔG^\ddagger indicate the ease of occurrence of electrooxidation reactions at these potentials. The lowest activation energy is given by the second peak which is shown below to be the starting potential of sulfur deposition.

3.4 Proposed Mechanism of sulfur electrodeposition

The following anodic reactions are expected to occur in the sulfide system, resulting in the formation and removal of sulfur layer (Feng et al., 2005; Kapusta et al., 1987; Mohtadi et al., 2005; Ramsbramanian 1975):



In view of the values of pK₁ and pK₂ of H₂S (7 and 14, respectively), the predominant species in this electrolyte is HS⁻ at pH values from 9 to 12. By sweeping the electrode potential towards more positive (figure 1), a small shoulder at point (b) is formed which may be due to the starting point of the deposition of elemental sulfur. The starting of formation of white thin layer adherent to the electrode surface was observed exactly at this potential. Such formation causes the reduction in the size of effective surface of the Pt electrode. The formation of large peak afterward at point (c) (see figure 1) can be explained on the basis of the oxidation of the deposited sulfur according to the equation (12) to form soluble sulfate ions. The phenomenon of periodic formation and dissolution of sulfur element on the Pt electrode could be represented as follows:



The above mechanism is substantiated by XPS performed on the electrodes surface after potentiostatic experiments. Many XPS spectra of polycrystalline platinum polarized at different potentials in sulfide polluted salt water were measured. An illustrative example of these spectra is shown in figure (9). It shows XPS spectrum of platinum electrode polarized at a potential of 1.0 V for 60 minutes containing 0.15 M HS⁻. A sharp S2p peak appears at 163.2 eV (referred to C1s at 284.6 eV), which is characteristic of the presence of elemental sulfur (S) on the electrode (Wagner 1990). As can be seen in figure (9), a small shoulder appears at 169.2 eV which indicates the presence of sulfate (SO₄²⁻) ions. This is due to the partial oxidation of deposited sulfur at 1.0 V.

4. Summary and Conclusions

Cyclic voltamograms of polycrystalline platinum show negligibly small currents in the absence of sulfide ions compared to those measured in its presence, at all potentials. These anodic currents are indeed resulting from the oxidation of the sulfide ions. The magnitude of currents measured in the reverse sweep is much less than those measured in the forward sweep which reveals that the reaction products in the forward sweep have passivated the platinum surface. Three current peaks appear in the forward sweep at potentials of -0.1, 0.475 and 1.0 V, respectively. The first peak indicates the possibility of the formation of platinum sulfide and poly sulfide. The second peak may be due to the starting point of the deposition of elemental sulfur. A white thin layer adherent to the electrode surface starts exactly at this potential. The third peak can be explained on the basis of the oxidation of the deposited sulfur to form soluble sulfate ions.

References

Anani, A., Mao, Z., White, R. E., Srinivasan, S. & Appleby, A. J. (1990). Electrochemical production of hydrogen and sulfur by low-temperature decomposition of hydrogen sulfide in an aqueous alkaline solution. *J. Electrochem. Soc.*, 137-2703.

- Ateya, B. G., Alkharafi, F. M., Alazab, A. S. & Abdullah, A. M. (2007). Kinetics of the electrochemical deposition of sulfur from sulfide polluted brines. *J. App. Electrochem.*, 37, 395-404.
- Ateya, B. G., Alkharafi, F. M., El-Shamy, A.M., Saad, A. Y. & abdalla, R. M. (2009). Electrochemical desulfurization of geothermal fluids under high temperature and pressure. *J. App. Electrochem.*, 39, 383-389.
- Chen, A. & Miller, B. (2004). Potential oscillations during the electrocatalytic oxidation of sulfide on a microstructured Ti/Ta₂O₅-IrO₂ electrode. *J. Phys. Chem. B*, 108, 2245-2251.
- Clauser, C. (2006). Geothermal Energy, In: K. Heinloth (ed), Landolt-Börnstein, Group VIII: *Advanced Materials and Technologies*, Vol. 3: Energy Technologies, Subvol. C: Renewable Energies (493-604), Springer Verlag, Heidelberg-Berlin.
- Cutter, G. A. and Krahforst, C. F. (1989). Sulfide in surface waters of the western Atlantic Ocean. *Geophys. Res. Lett.*, 15, (12) 1393-1396.
- Cutter, G. A., Walsh, R. S. & de Echols, C. S. (1999). Topical Studies in Oceanography. *Deep-Sea Res II*, 46, 991-1010.
- Darely, H. C. H. & Gray, G. R. (1988). *Composition and Properties of Drilling and Completion Fluids*, 5th ed., Gulf Publishing Company, Houston (p.477).
- Daley, M. A., Mangun, C. L., DeBarr, J. A., Riha, S., Lizzio, A. A., Donnals, G. L. & Economy, J. (1997). Adsorption of SO₂ onto oxidized and heat-treated activated carbon fibers (ACFs). *Carbon*, 35, 411-417.
- Feng, J., Gao, Q., Xu, L. & Jichang Wang, J. (2005). Nonlinear phenomena in the electrochemical oxidation of sulfide. *Electrochemistry Communications*, 7, 1471-1476.
- Garverick, L. (1994). *Corrosion in the Petrochemical Industry*, ASM International, Metals Park, Ohio (p. 259).
- Kagel, A. (2008). *The State of Geothermal Technology*, Part II: Surface Technology, The Department of Energy, Washington, D. C. (p 5).
- Kapusta, S., Viehbeck, A., Willhel, S. M. & Hackerman, N. (1987). The anodic oxidation of sulfide on platinum electrodes. *J. Electroanal. Chem.*, 153, 157-174.
- Laidler, K. J. (1993). *The World of Physical Chemistry*, Oxford University Press, Oxford. Li Zhong, Ming QI, Guolin WEI, Jingli LUO and, Chuang, K. (2006). An Intermediate-temperature H₂S Fuel Cell with a Li₂SO₄-based Proton-conducting Membrane. *Chinese Journal of Chemical Engineering*, 14 51-55.
- Luther III, G. W. & Tsamakis, E. (1989). Concentration and form of dissolved sulfide in the toxic water column of the ocean. *Mar. Chem.*, 27, 165-177.
- Mao, Z., Anani, A., White, R. E., Srinivasan, S. & Appleby, A. J. (1991). A Modified Electrochemical Process for the Decomposition of Hydrogen Sulfide in an Aqueous Alkaline Solution. *J. Electrochem. Soc.*, 138, 1299.
- Miller, B. & Chen, A. (2005). Effect of concentration and temperature on electrochemical oscillations during sulfide oxidation on Ti/Ta₂O₅-IrO₂ electrodes. *Electrochimica Acta*, 50, 2203-2212.
- Miller B., & Chen, A. (2006). Oscillatory instabilities during the electrochemical oxidation of sulfide on a Pt electrode. *J. Electroanal. Chem.*, 588, 314-323.
- Mohtadi, R., Lee, W. K., Van Zee, J. W. (2005). The Effect of Temperature on the Adsorption Rate of Hydrogen Sulfide on Pt Anodes in a PEMFC. *Applied Catalysis B: Environmental* 56, 37-42.
- Mikhailovsky, S. V. & Zaitsev, Y. P. (1997). Catalytic properties of activated carbons I. Gas-phase oxidation of hydrogen sulphide. *Carbon*, 35, 1367-1374.
- Park, Y. G. (2008). Removal Study of Hydrogen Sulfide Using Natural Second Metabolites. *Biotechnology and Bioprocess Engineering*, 13, 325-331.
- Radford, J. & Cutter, G. A. (1994). Biogeochemistry of dissolved hydrogen sulfide species and carbonyl sulfide in the western North Atlantic. *Geochim. Cosmochim. Acta*, 58, 5421-5431.
- Ramsubramanian, N. (1975). Anodic behavior of platinum electrodes in sulfide solutions and the formation of platinum sulfide. *J. Electroanal. Chem.*, 64, 21-37.
- U.S. Environmental Protection Agency (1988). *Extremely Hazardous Substances*, vol. 1 A-L, Noyes Data Corporation, Park Ridge, New Jersey, USA.
- Wagner, C. D. (1990). Auger and X-Ray Photoelectron Spectroscopy. In D. Briggs and M. P. Seath, *Practical Surface Analysis* (p.595), Vol. 1, 2nd ed., John Wiley & Sons, New York.

Xu, Y., Shonnen, M. A. A., Nordstram, D. K., Cunningham, K. M. & Ball, J. W. (2000). Sulfur geochemistry of hydrothermal waters in Yellowstone National Park, Wyoming, USA. II. Formation and decomposition of thiosulfate and polythionate in Cinder Pool, *J. Volcanology and Geothermal Research*, 97, 407-423.

Figures Captions

Figure 1. Cyclic voltammograms (1st cycle) of 3.5 % NaCl solution without (solid line) and with (dashed line) 0.15 M HS⁻ on polycrystalline platinum at scan rate 10 mV s⁻¹ at 25°C.

Figure 2. Consecutive cyclic voltammograms of 3.5 % NaCl solution containing 0.15 M HS⁻ on polycrystalline platinum at scan rate 10 mVs⁻¹ at 25°C.

Figure 3. Effect of scan rate on the cyclic voltammograms of 3.5% NaCl solution containing 0.15 M HS⁻ on polycrystalline platinum at 25°C.

Figure 4. Relation between scan rate (v) of the cyclic voltammograms and the peak currents of 3.5 % NaCl solution containing 0.15 M HS⁻ on polycrystalline platinum at 25°C.

Figure 5. Relation between scan rate (v) of the cyclic voltammograms and the peak potentials of 3.5 % NaCl solution containing 0.15 M HS⁻ on polycrystalline platinum at 25°C.

Figure 6. Effect of HS⁻ ions concentration on the cyclic voltammograms (1st cycles) of 3.5 % NaCl solution on polycrystalline platinum at scan rate 10 mVs⁻¹.

Figure 7. Effect of temperature on the cyclic voltammograms (1st cycles) of 3.5 % NaCl solution containing 0.15 M HS⁻ on polycrystalline platinum at scan rate 10 mVs⁻¹.

Figure 8. Arrhenius plot of the different peaks of the cyclic voltammograms in Figure (7).

Figure 9. XPS spectrum of a polycrystalline platinum electrode after potentiostatic polarization at 1.00 V (Ag/AgCl) for 1 hour in presence of 3.5 % NaCl solution containing 0.15 M HS⁻ at 25°C.

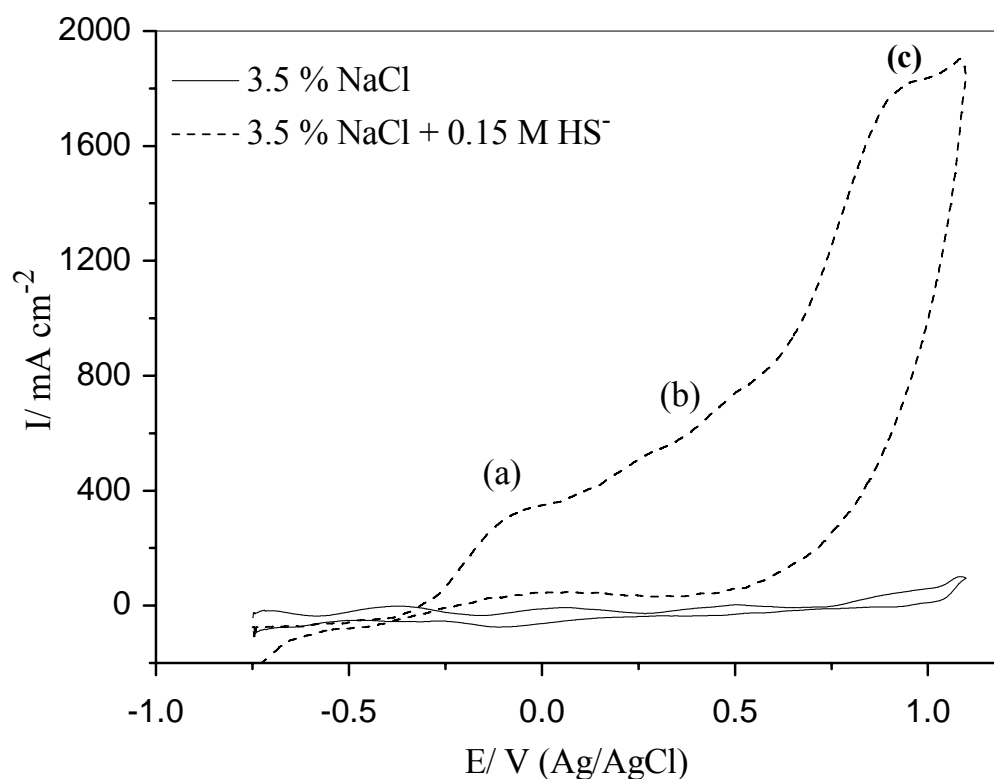


Figure 1. Cyclic voltammograms (1st cycle) of 3.5 % NaCl solution without (solid line) and with (dashed line) 0.15 M HS⁻ on polycrystalline platinum at scan rate 10 mV s⁻¹ at 25°C.

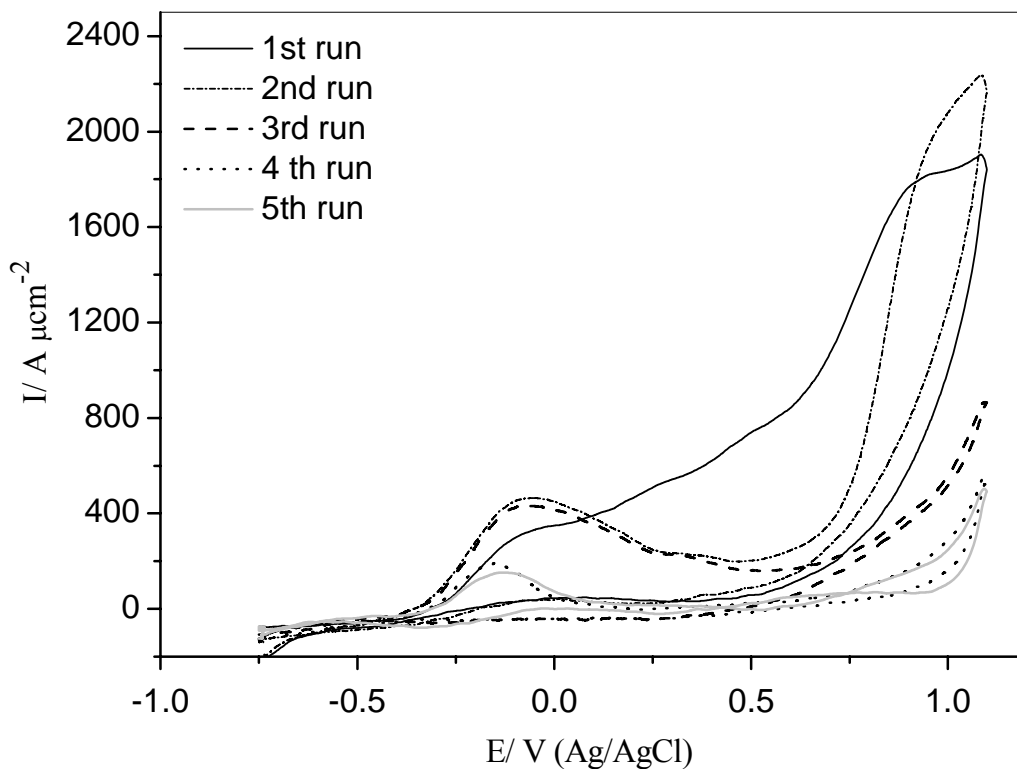


Figure 2. Consecutive cyclic voltammograms of 3.5 % NaCl solution containing 0.15 M HS⁻ on polycrystalline platinum at scan rate 10 mVs⁻¹ at 25°C.

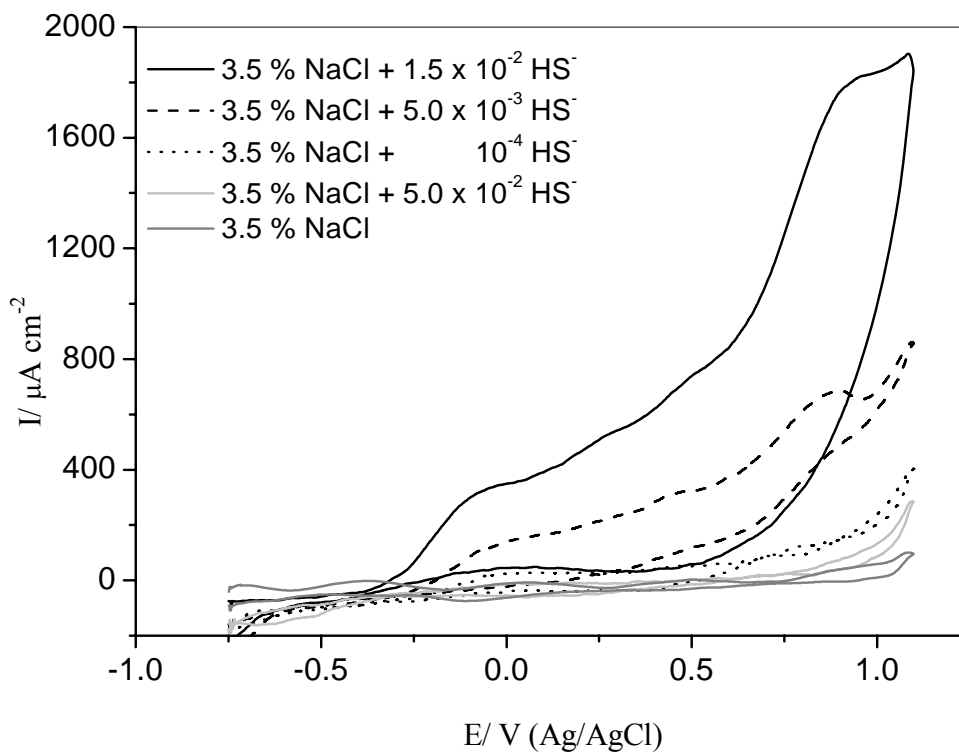


Figure 3. Effect of HS⁻ ions concentration on the cyclic voltammograms (1st cycles) of 3.5 % NaCl solution on polycrystalline platinum at scan rate 10 mVs⁻¹.

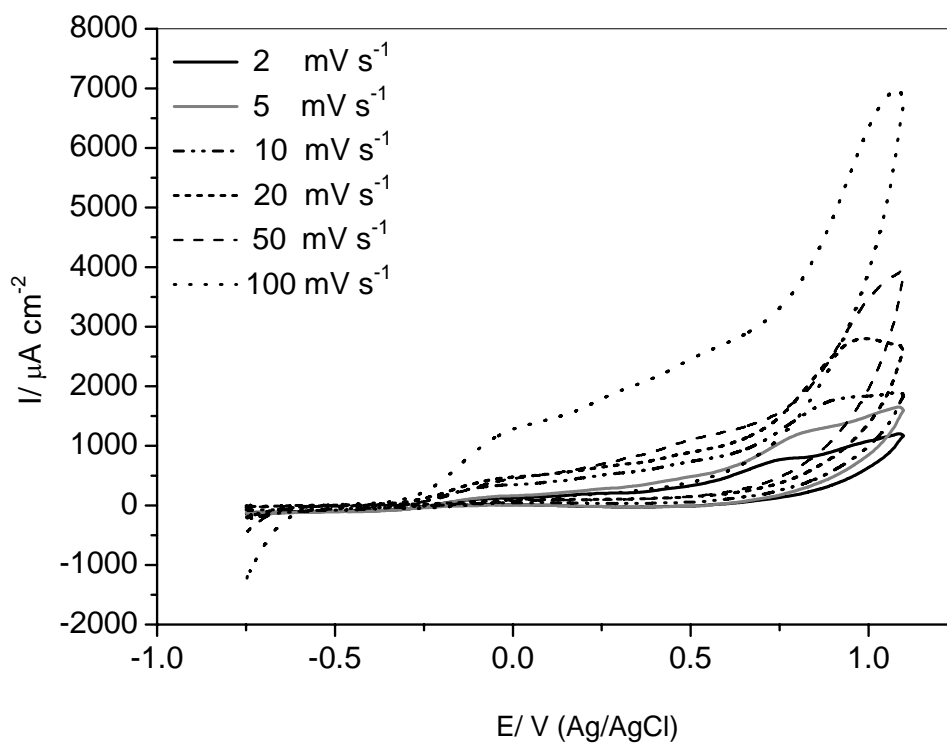


Figure 4. Effect of scan rate on the cyclic voltammograms of 3.5% NaCl solution containing 0.15 M HS⁻ on polycrystalline platinum at 25°C.

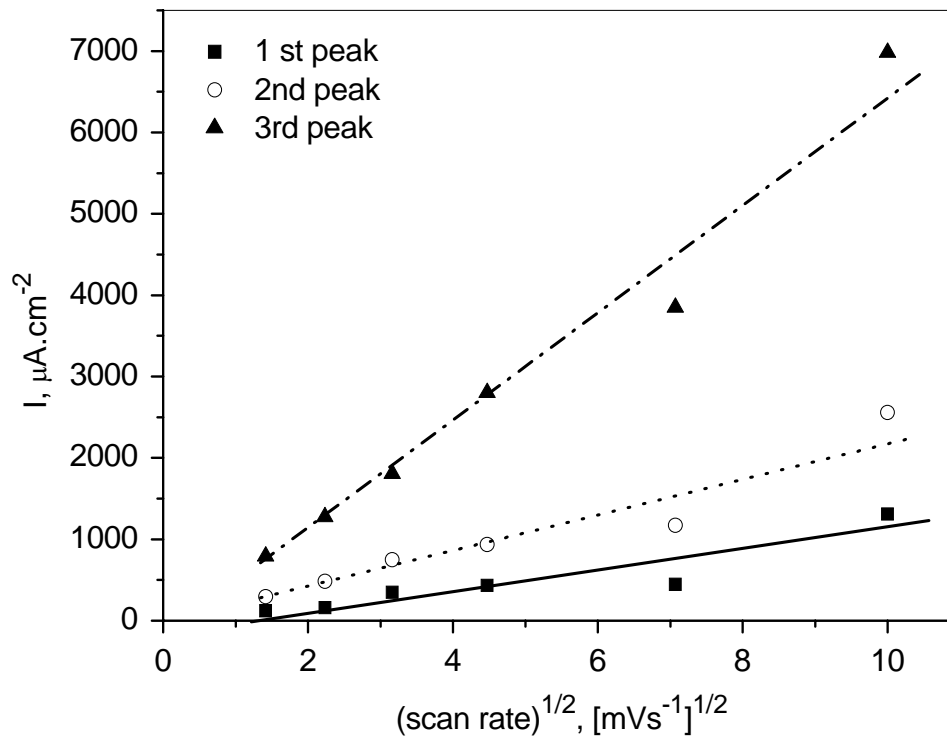


Figure 5. Relation between scan rate (v) of the cyclic voltammograms and the peak currents of 3.5% NaCl solution containing 0.15 M HS⁻ on polycrystalline platinum at 25°C.

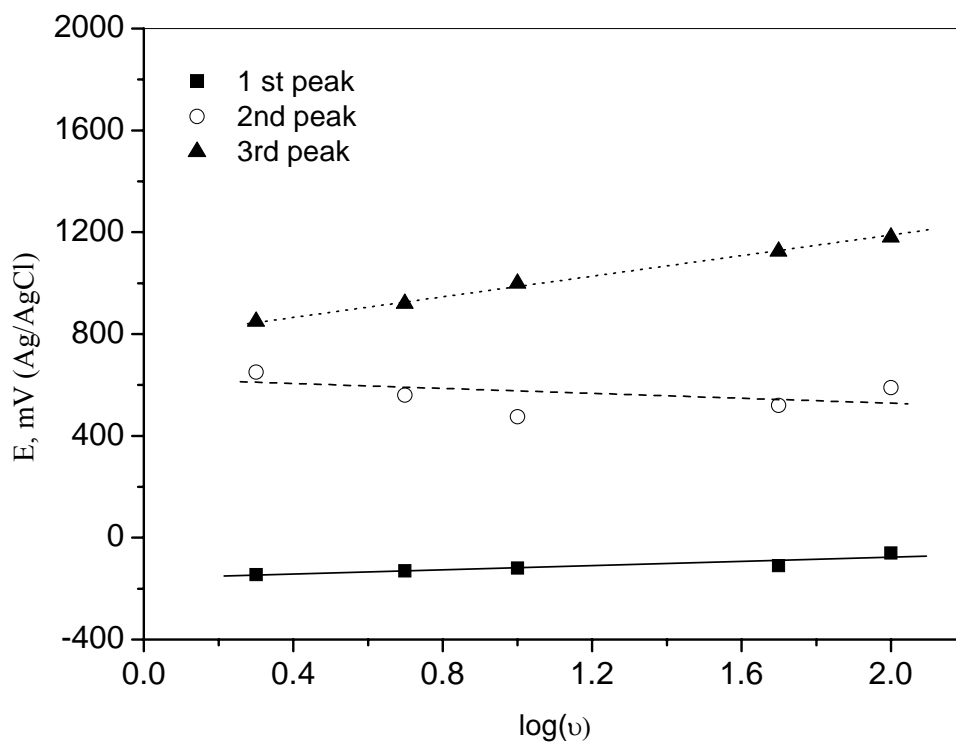


Figure 6. Relation between scan rate (v) of the cyclic voltammograms and the peak potentials of 3.5 % NaCl solution containing 0.15 M HS⁻ on polycrystalline platinum at 25°C.

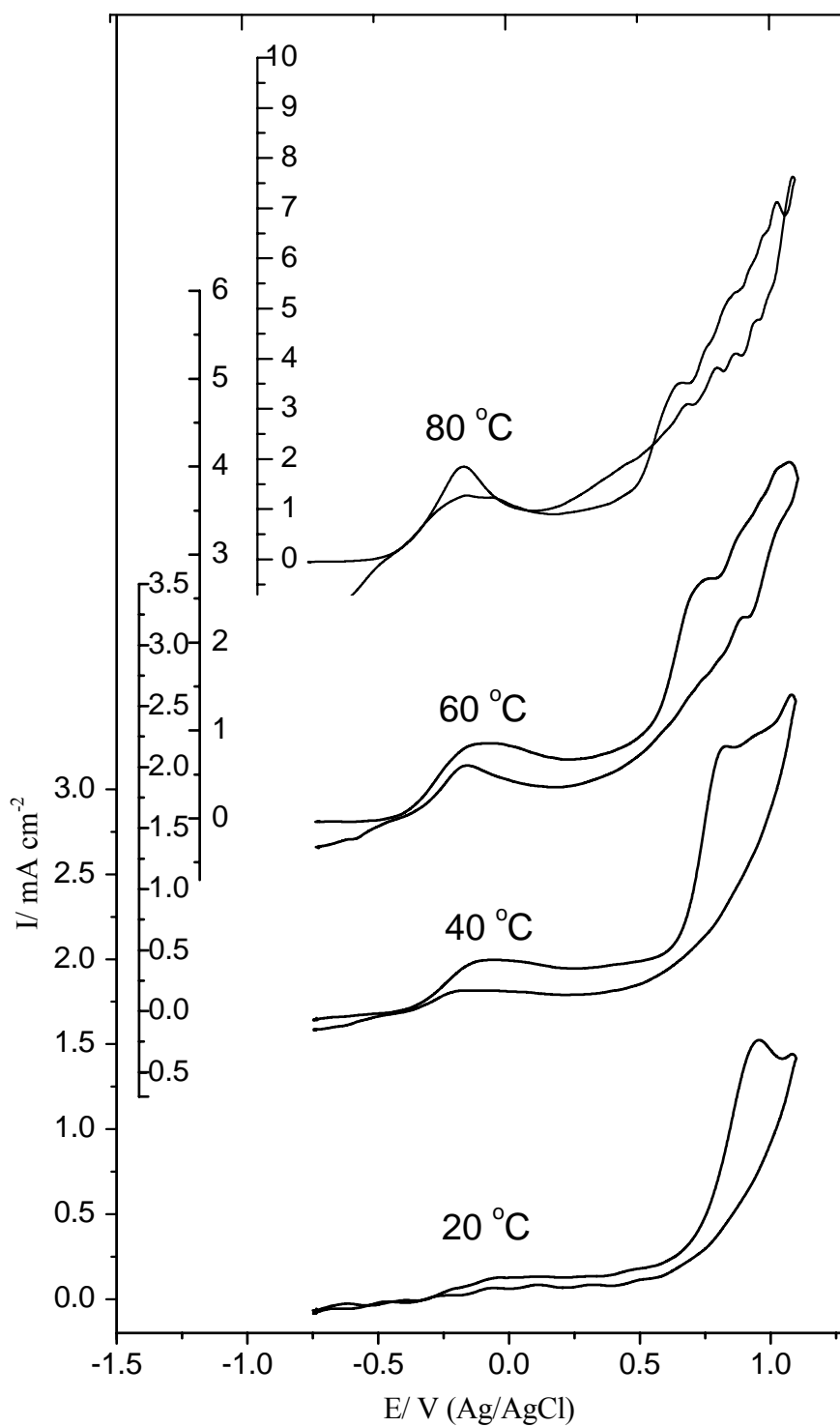


Figure 7. Effect of temperature on the cyclic voltammograms (1st cycles) of 3.5 % NaCl solution containing 0.15 M HS⁻ on polycrystalline platinum at scan rate 10 mVs⁻¹.

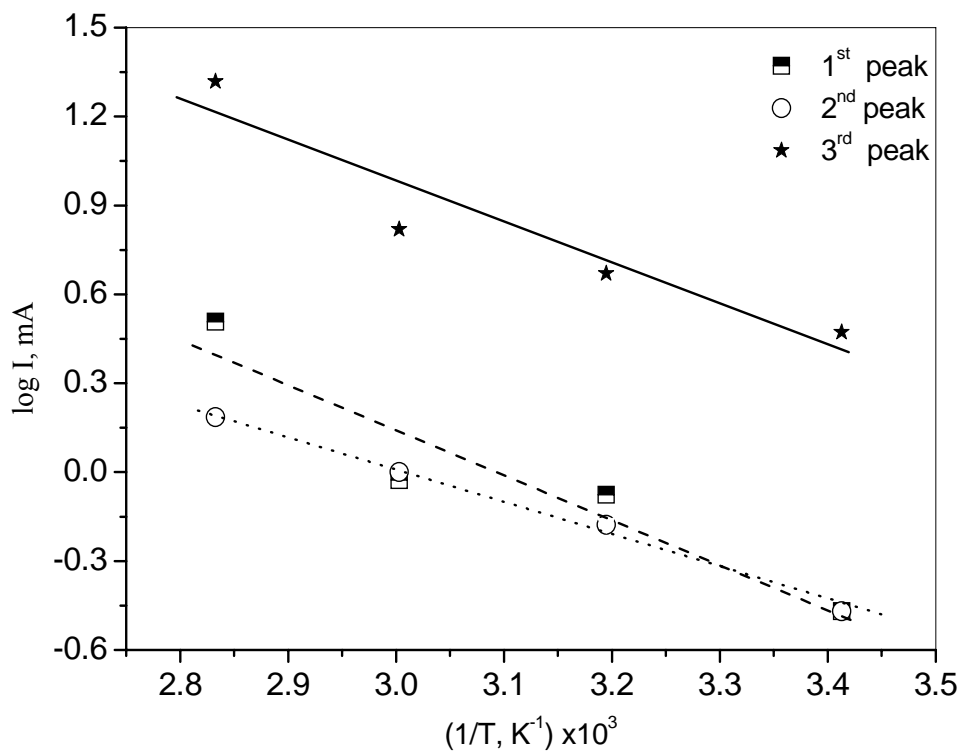


Figure 8. Arrhenius plot of the different peaks of the cyclic voltammograms in Figure (7).

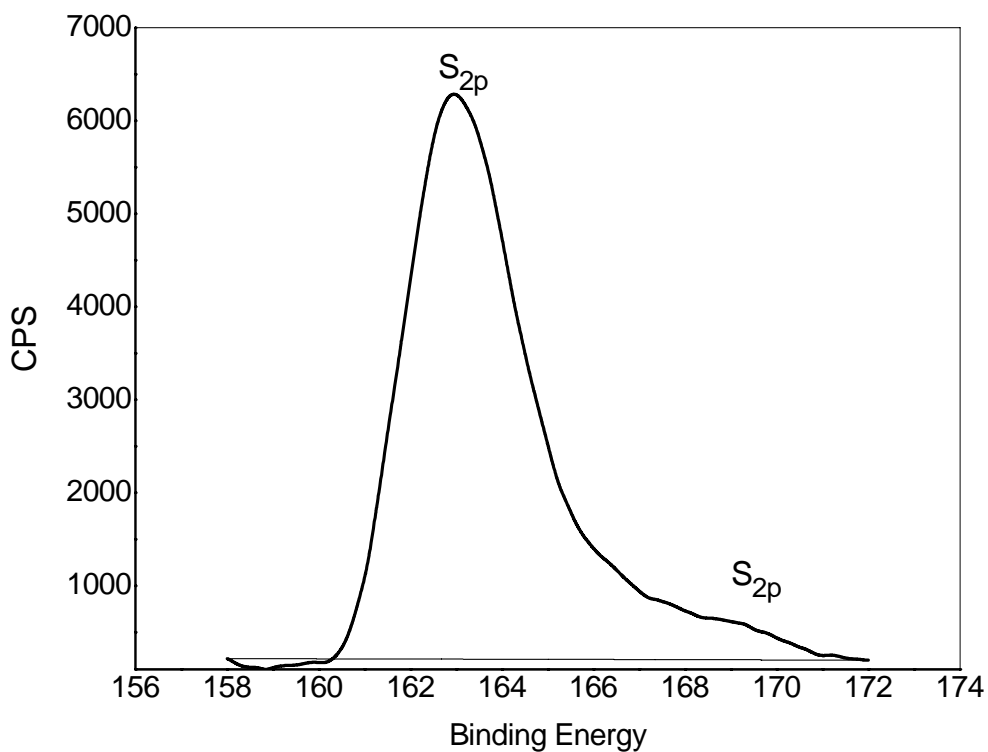


Figure 9. XPS spectrum of a polycrystalline platinum electrode after potentiostatic polarization at 1.00 V (Ag/AgCl) for 1 hour in presence of 3.5 % NaCl solution containing 0.15 M HS⁻ at 25°C



Analysis and Supplement with the Mechanism of Electrosynthesizing Benzofuran Derivatives

Yunhui Li, Jie Zhou, Xiuxia Gao, Feifei Wang & Yupeng Wang

School of Chemistry and Environmental Engineering

Changchun University of Science and Technology

Changchun 130022, China

E-mail: liyh@cust.edu.cn

Abstract

Davood Nematollahi et al. have successfully electrosynthesised a series of benzofuran derivatives in the presence of nucleophile agents. Base on their experimental result, we analyzed the electron density of the intermediate during benzofuran derivatives synthesis and reached the same conclusions as that of Davood Nematollahi et al. Therefore, the method of electron density analysis is proven to be correct and expected to have a wide applications. But after we analyzed the electron density of 2-aldehyde-p-quinone(1a) and 3-carboxyl-o-quinone(7a), we have different opinions with theirs. The electron density of C-6 position of the 2-aldehyde-p-quinone lower than the that of C-5 position leads to the final product 6 when electrochemical oxidation of the 2,5-dihydroxybenzaldehyde. For 2,3-dihydroxybenzoic acid case, since the competition between the carboxyl of the C-2 position and the carboxyl of the C-1' position in the 3-carboxyl-o-quinone and the hydrogen transferred to the carboxyl of the C-1' position, there will be a rearrangement before the next electrochemical oxidation and the final product 21 will be formed.

Keywords: Electroorganic, Rearrangement, Electron density

1. Introduction

Benzofuran derivatives constitute a major group of the nature's collection of biologically active heterocycles. (Nematollahi, D., 2007, p.3646-3651). They are usually important constituents of plant extracts used in traditional medicine (Csekei, M., 2004, p.285-291). and effective as antitumor agents(Hayakawa, I., 2004, p.3411), antidepressants (Gaszner, P., 2006, p.14), antihypertensives and cytotoxic(Banskota, A. H., 2000, p.1277-1279.).

A series of benzofuran derivatives have been electrosynthesised in the presence of nucleophile agents using cyclic voltammetry and controlled-potential coulometry methods by Davood Nematollahi et al. (Nematollahi, D., 2000, p.208-214. Afkhami, A., 2005, p.5633-5640. Fakhari, A. R., 2007, p.3894-3898. Fakhari, A. R., 2005, p.205-210.Nematollahi, D., 2004, p.591-595).To synthesize new benzofuran derivatives Davood Nematollahi et al. studied the electrochemical oxidation of benzenediols in aqueous solutions and in the presence of a variety of nucleophiles derived from CH acids.(a)Nematollahi, D., 2003, p.1639-1644 (b)Nematollahi, D., 2004, p.2637-2640 (c)Nematollahi, D., 2004, p.31-37).

In this direction, they investigated the electrochemical oxidation of catechols in the presence of α -diketone such as acetylacetone(Nematollahi, D., 2005, p.638-644) and dimedone. (Nematollahi, D., 2007, p.3646-3651. Nematollahi, D., 2003, p.1639-1644). As a lot of works and studies have been done, they concluded the similar mechanisms of electrochemical oxidization followed with the Michael addition reactions in the electrosynthesis of the parent-starting molecule showed as Scheme 1.

After we studied the mechanics and data of experiments by Davood Nematollahi et al. in details, we are mysterious about some questions:1) would do the nucleophile agents attack the same position of the carbon of the intermediates while the R^2 is different, such as methoxy and carboxyl, and R^1 is same:2) if is there an effect of R^2 on the position where the nucleophile agents attack and how about the effect. Based on these questions, we analyze the electron density of the intermediates and proved our ideas with the aid of the calculation and the data reported.

2. The analysis of the electron density

Davood Nematollahi et al. reported that 3-methoxy-o-quinone is attacked in C-5 position by 2-mercaptobenzoxazole leading to the formation of 5-(Benzo[d]oxazol-2-ylthio) -3-methoxybenzene-1,2-diol (Nematollahi, D., 2005,

p.7769–7772). They successfully illustrated that the process as Scheme 2 is disadvantage for the reaction.

We studied the process by the analysis of the electron density of the 3-methoxy-o-quinone. Initially, the electron cloud of carbon of benzene is set as the standard and signed as δ . Then the carbon of 3-methoxy-o-quinone (2d) is assigned with a number which is shown as Figure 1(A).

Since connecting the oxygen directly, the electron cloud of C-1, C-2, C-3 position is lower than δ and signed as δ^- . There is a conjugated structure among the C-1, C-6, C-5 as Figure 1(B) shown which leads the higher electron cloud of C-6 position than δ (signed as δ^+). While the electron cloud of C-5 should be δ^- . Since the connection of C-3, C-4, C-5 and C-6 is similar to the butadiene, the electron cloud of C-4 should be δ^- . As a result, an graphics of electron cloud of 3-methoxy-o-quinone is shown as Figure 1(C). Then it would be found that the electron density of C-5 position is lower than that of the C-4 position according to Figure 1(C). The nucleophile agent attacks the carbon of lower electron density firstly, and the C-4 position is forbidden to be attacked, Scheme 2 would not happen during the process. Our conclusion is consistent with the result of Davood Nematollahi et al. which means that the method in the analysis of electron density is reasonable.

The electrochemical oxidation of 2,5-dihydroxybenzaldehyde(1) in the presence of 3-hydroxy-1H-phenalen-1-one has also been reported¹. But there is no reasonable explanation why the 2-aldehyde-p-quinone is attacked in the C-5 position, not the C-6 position in the reference. Therefore, we analyze the electron density of carbons in benzene rings of 2-aldehyde-p-quinone.

Every carbon of the intermediate 2-aldehyde-p-quinone is assigned with a number and shown as Figure 2(A). Assuming that the electron density of the C-5 and the C-6 would be equal at first, then their electron density would be affected by the neighbor carbons which are in the three conjugated structures shown as Figure 2(B), Figure 2(C), Figure 2(D) respectively.

In Figure 2(B), the C-2 position shows δ^- and the C-3 position shows δ^- . Because of the effect of the steric hindrance of the carboxyl of the C-1', the C-3 position is difficult to be attacked by the nucleophile agent. The C-5 position and C-6 position should be affected by the electron density of the C-1 and the C-4 shown as Figure 2(C), Figure 2(D) respectively.

In Figure 2(C), there would be two reasonable situations: a) the C-6 showing δ^- and the C-5 showing δ^- ; b) the C-6 showing δ^- and the C-5 showing δ^- . In Figure 2(D), the case a) should be the only reasonable situation. If the C-5 showing δ^- , then the C-3, C-4, C-5 all showing δ^- result in the unstable structure. So the C-6 shows δ^- and the C-5 shows δ^- as Figure 2(E) and the electron density of C-6 position is lower than that of the C-5 position. Then the nucleophile agent intends to attack the C-6 position first conduce the final product 6 shown as Figure 3(B).

For further proving our conclusion, the σ value of ¹H NMR in the C-a position and C-b position shown as Figure 3(A), Figure 3(B) respectively are calculated by the following exponential formula(1):

$$\sigma = 7.26 + \sum S \quad (1)$$

Where S is the sum of the chemical shifts for the substituents.

And the σ value of ¹³C NMR of the hydrogen in the C-a position and C-b position is also calculated as the sum of a series of constants by the following equation(2):

$$\sigma = 128.5 + \sum A \quad (2)$$

Where A is the sum of the chemical shifts for the substituents.

The calculated and experimental results are shown in Table 1:

Comparing the calculation value with the experimental data, it will be found that the δ value of ¹H NMR and ¹³C NMR of C-b is much closer to the experimental data, so the structure of Figure 3(B) is more reasonable. Therefore, it is logical to propose the process shown as Scheme 3. Since we consider the ring of furan equal to the combination of a methoxy and an ethyl when we calculate, there is a small difference between the calculated value and the experimental data.

3. Mechanism Analysis –Intramolecular Rearrangement

The electrochemical oxidation of 2,3-dihydroxybenzoic acid in the present of 3-hydroxy-1H-phenalen-1-one has been reported by Davood Nematollahi et al. (Nematollahi, D., 2007, p.3646-3651). After we studying the data of characterization of the products in the reference, we find that there is much similarity between the product 13 (the structure is shown as Figure 5(A)) and the product 20d (the structure is shown as Figure 6(A)). Their experimental data shows as Table 2 and Table 3 (In order to forbid confusion, we use the 13 and 20d signed by Davood Nematollahi et al. here).

Compare with the σ value of ^1H NMR of the product 13 and the product 20d according to Table 2, we find that the σ value are same at 7.25, 9.07, 10.39 and uniform at 7.81~8.60 (where there are six apex in the 13 and at the homologous position there is a broad apex in the 20d). The difference of the aldehyde of the 13 and the carboxyl of the 20d reflects at 13 and 12.92. It is reasonable to conclude that the position of the hydrogen on the 13 and 20d is uniform. According to Table 3.

The comparison of the σ value of ^{13}C NMR of the product 13 and the product 20d is shown as Table 3. The σ value are same at 99.1, 111.9, 116.7, 120.3, 125.2, 125.3, 127.5, 127.8, 129.6, 130.6, 132.5, 132.6, 135.8, 141.8, 146.5, 149.1, 159.8, 168.2. The experimental data between 13 and 20d reflect that the position of carbon on them are uniform. Combining with the conclusion of Table 2, we draw the conclusion that 13 and 20d have the same structure. So it is reasonable to present the structure as Figure 4(B) shows.

For further proving our conclusion, the σ value of ^1H NMR and ^{13}C NMR in the C-c and C-d position is calculated with the equation (1) and equation (2). The calculated and experimental results are shown in Table 1. According to the calculation value and the experimental data, it will be found that the δ value of ^1H NMR and ^{13}C NMR of C-d is much closer to the experimental data, so the structure of Figure 4(B) is more reasonable.

The carbon of 3-carboxyl-o-quinone is assigned with a number which is shown in Figure 5(A) and the structures that main effect the electron density of the C-4 position and the C-5 position are shown as Figure 4(B) and Figure 4(C) respectively.

Similar analysis of the electron density is taken and we find that the electron density of the C-4 and the C-5 position are all showing as δ . But because of the effect of the steri hindrance of the carboxyl of the C-1', the C-4 position is difficult to be attacked by the nucleophile agent. So there is an advantage that the nucleophile agent attacks the C-5 position.

Since there is a di-carboxyl conjugated with the C=C of C-3 and C-4 position shows as Figure 5(C), the following hydrogen transfer has two reasonable ways shows as Figure 6(A), Figure 6(B) respectively. When the hydrogen transfers to the C-3 position, it should move to the carboxyl of C-1' position because the carboxyl and the hydroxyl in the C-1' position are conjugated. It is advantaged to form 9b. So the process shows as Figure 6(B) is dominant.

It is unstable that there is two hydroxyl at the same carbon of 9b and one hydroxyl will leave making the transfer of hydrogen between the C-4 position and the C-1' position. Then the hydroxyl on the C-1' position attacks the C-4 position and the two atoms became close with each other and the C-O bond formation. As the hydroxyl is connected to the C-4 position, there is a 1,6- σ transfer between the C-1 position and the C-1' position because there is a resuming aromaticity tendency. After a molecule of water attacks the C and leaves a proton, the intermediate 16a is formed. The final product 21 is formed after the electrochemical oxidation of the 16a and an subsequent intramolecular cyclization. The details are shown as Scheme 4.

Compared with 6 (the structure shows as Figure 3(B)) and 21 (the structure shows as Figure 4(B)), we find that the two construction are consistent. With the consideration of discussion above, the process of Scheme 3 and Scheme 4 agreed with the experimental data.

4. Conclusion

Base on the experimental data of Davood Nematollahi et al., we draw the same conclusion by analyzing the electron density of the 3-methoxy-o-quinone and prove that the analysis method is correct. The electron density of C-6 position of the 2-aldehyde-p-quinone is lower than the C-5 position bringing the final product 6 when electrochemical oxidation of 2,5-dihydroxybenzaldehyde. For 2,3-dihydroxybenzoic acid case, there is a intramolecular rearrangement before the subsequent electrochemical oxidation reaction because of the nuclephic agents attacks the C-5 position and the final product (21) get.

Acknowledgment

The analysis is on the boot of the Mechanisms and the data of the electrosynthesis of the benzofuran derivatives that the papers Davood Nematollahi reported. Thanks for their factuality and the experimental data.

References

- Afkhami, A., Nematollahi, D., Madrakian, T. & Khalafi, L. (2005). Investigation of the electrochemical behavior of some catecholamines in the presence of 4-aminobenzoic acid. *Electrochimica Acta.*, 50(28), 5633–5640.
- Banskota, A. H., Tezuka, Y., Midorikawa, K., Matsushige, K. & Kadota, S. (2000). Two Novel Cytotoxic Benzofuran Derivatives from Brazilian Propolis. *J. Nat. Prod.*, 63, 1277-1279.
- Csékei, M., Novák, Z., Timári, G. & Kotschy, A. (2004). The 'one-pot' preparation of substituted benzofurans. *Arkivoc*, 285-291.
- Fakhari, A. R., Nematollahi, D. & Moghaddam, A. B. (2005). Electrochemical study of catechols in the presence of

- 4,6-dihydroxy-2-methylpyrimidine . *J. Electroanal. Chem.*, 577(2), 205-210.
- Fakhari, A. R., Nematollahi, D., Shamsipur, M. & Makarem, S. et al. (2007). Electrochemical synthesis of 5,6-dihydroxy-2-methyl-1-benzofuran-3-carboxylate derivatives. *Tetrahedron Letters.*, 63, 3894-3898.
- Gaszner, P., Miklya, I. (2006). Major depression and the synthetic enhancer substances, (-)-deprenyl and R-(-)-1-(benzofuran-2-yl)-2-propylaminopentane. *Prog. Neuro-Psychopharmacol. Biol. Psychiatry*, 30, 14.
- Hayakawa, I., Shioya, R., Agastuma, T., Furokawa, H. & Sugano, Y. (2004). Thienopyridine and benzofuran derivatives as potent anti-tumor agents possessing different structure-activity relationships. *Bioorg. Med. Chem. Lett.*, 14, 3411.
- Nematollahi, D., Amani, A. & Tammari, E. (2007). Electrosynthesis of Symmetric and Highly Conjugated Benzofuran via a Unique ECECC Electrochemical Mechanism: Evidence for Predominance of Electrochemical Oxidation versus Intramolecular Cyclization. *J. Org. Chem.*, 72 (10), 3646–3651.
- Nematollahi, D., Tammari, E. (2005). Electroorganic Synthesis of Catecholthioethers. *J. Org. Chem.*, 70 (19), 7769–7772.
- Nematollahi, D., Forooghi, Z. (2003). ECEC and ECE-Type Mechanisms in Electrochemical Oxidation of 4-Substituted Catechols in the Presence of 4-Hydroxy-6-methyl-2-pyrone. *Electroanalysis*, 15(20), 1639-1644.
- Nematollahi, D., Habibi, D., Rahmati, M. & Rafiee, M. (2004). A Facile Electrochemical Method for Synthesis of New Benzofuran Derivatives. *J. Org. Chem.*, 69(7), 2637–2640.
- Nematollahi, D., Rafiee, M. (2004). Electrochemical oxidation of catechols in the presence of acetylacetone. *J. Electroanal. Chem.*, 566(1), 31-37.
- Nematollahi, D., Rafiee, M. (2005). Diversity in electrochemical oxidation of dihydroxybenzoic acids in the presence of acetylacetone. A green method for synthesis of new benzofuran derivatives. *Green Chem.*, 7, 638-644.
- Nematollahi, D., Golabi, S.M. (2000). Investigation of the electro-methoxylation reaction: Part 1. Electrochemical study of 4-tert-butylcatechol and 3,4-dihydroxybenzaldehyde in methanol. *J. Electroanal. Chem.* 481(2), 208–214.
- Nematollahi, D., Tammari, E., Sharifi, S. & Kazemib, M. (2004). Mechanistic study of the oxidation of catechol in the presence of secondary amines by digital simulation of cyclic voltammograms. *Electrochimica Acta.*, 49(4), 591-595.

Table 1. Comparison of the σ value of ^1H NMR and the ^{13}C NMR by calculation and experiments

	the result of calculation		experimental data
^1H NMR	C-a	6.67	7.25
	C-b	6.95	7.25
	C-c	6.32	7.25
	C-d	7.24	7.25
^{13}C NMR	C-a	109	116.7
	C-b	116	116.7
	C-c	103.8	116.6
	C-d	116.2	116.6

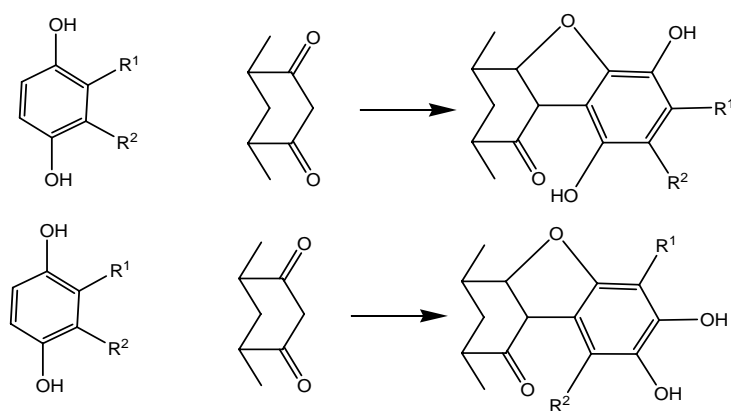
Table 2. Comparison of ^1H NMR of the product 13 and the product 20d

The sign of the formula of the product the molecular		the experimental data of ^1H NMR
13	$\text{C}_{20}\text{H}_{10}\text{O}_5$	7.25(s,1H, aromatic),7.81 (t, $J=7.4$ Hz, 1H,aromatic), 7.91 (t, $J=7.3$ Hz, 1H, aromatic),8.28, 8.35(dd, $J=8.2$ Hz, $J=6.4$ Hz,2H,aromatic), 8.44 (d, $J=7.6$ Hz, 1H, aromatic), 8.57 (d, $J=7.1$ Hz,1H,aromatic),9.07(s,1H, OH),10.40 (s, 1H, OH),13 (broad, 1H,aldehyde)
20d	$\text{C}_{20}\text{H}_{10}\text{O}_6$	7.25(s,1H, aromatic),7.88-8.60 (broad, 6H, aromatic), 9.07 (broad, 1H, OH),10.39 (broad, 1H, OH), 12.92 (broad,1H, acid)

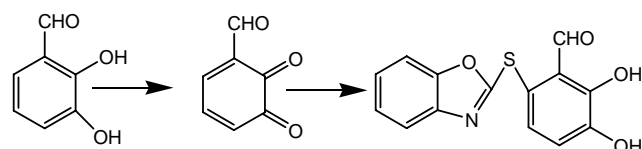
Table 3. Comparison of ^{13}C NMR of the product 13 and the product 20d

The sign of the formula of the product the molecular		the experimental data of ^{13}C NMR
13	$\text{C}_{20}\text{H}_{10}\text{O}_5$	99.1,111.9,116.7,120.3,125.2,125.3,127.5,127.8,129.6, 130.6,132.5,132.6,135.8,141.8,146.5,149.1,159.8,168.2
20d	$\text{C}_{20}\text{H}_{10}\text{O}_6$	99.1,111.9,116.6,116.8,120.3,125.1,125.4,127.5,127.8, 129.6,130.6,132.5,132.6,135.8,141.8,146.5,149.1,159.9, 168.2,179.1

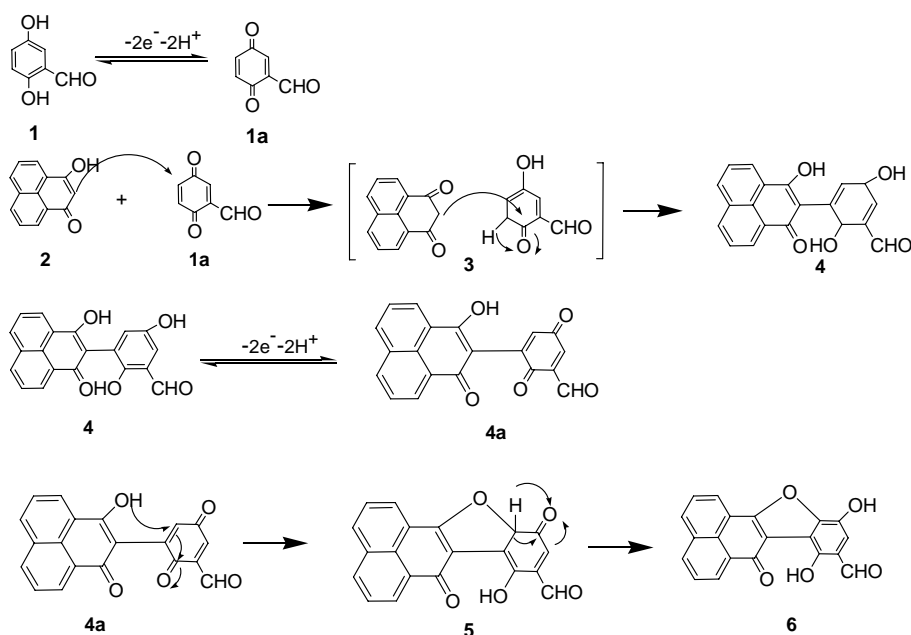
SCHEME 1



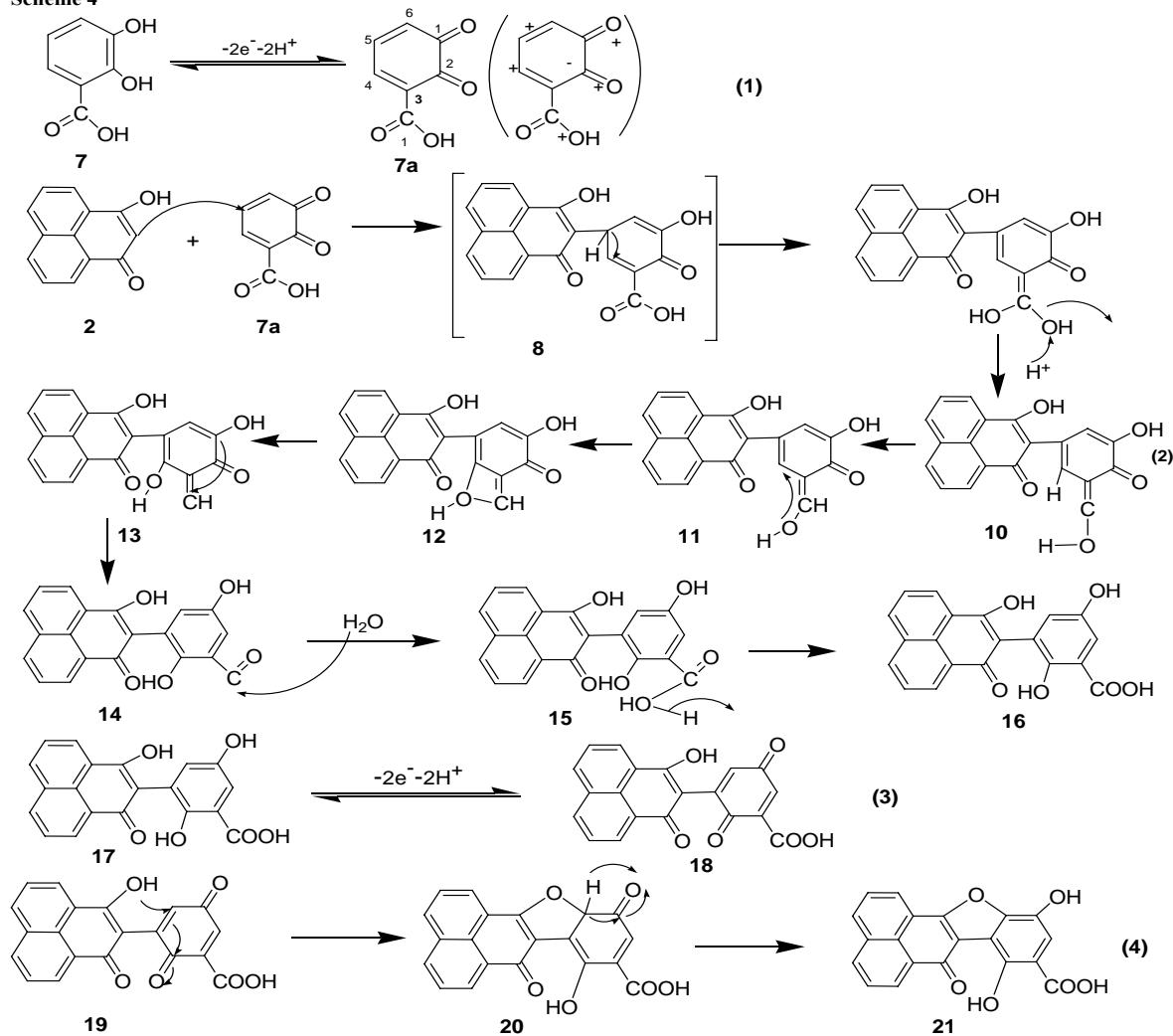
SCHEME 2



SCHEME 3



Scheme 4



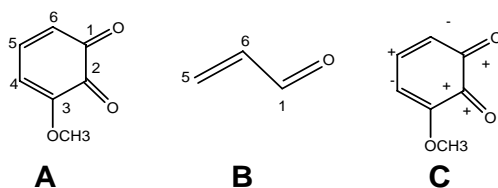


Figure 1. The number assigned and the electron density of the carbon of 3-methoxy-o-quinone

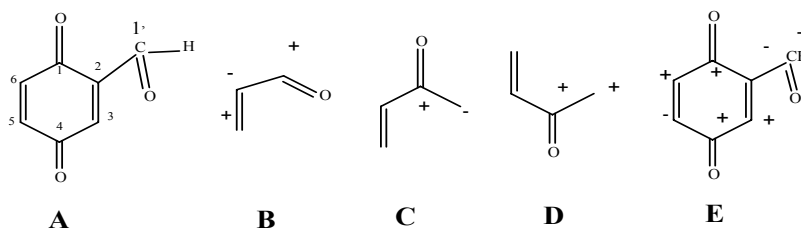


Figure 2. The number assignment and the electron density of the 2-aldehyde-p-quinone

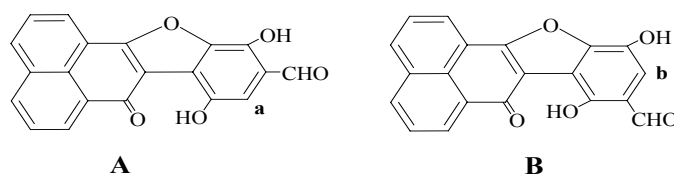


Figure 3. The finally product of electrosynthesis 2,5-dihydroxy-benzo aldehyde
(A) Davood Nematollahi reported (B) our result

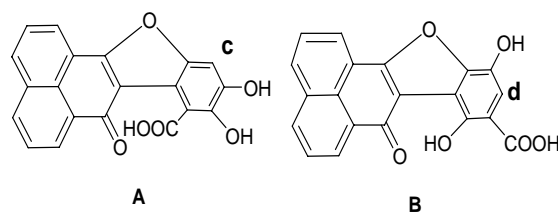


Figure 4. The finally product of electrosynthesis 2,3-dihydroxybenzoic acid
(A) Davood Nematollahi reported (B) our result

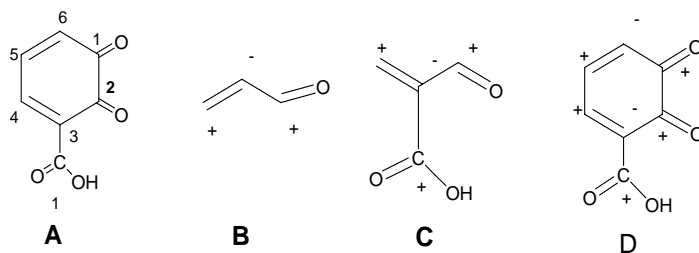


Figure 5. The number assignment and the electron density of 3-carboxyl-o-quinone

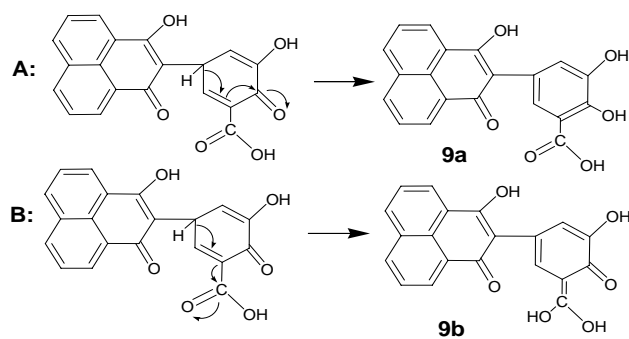


Figure 6. The two ways of the hydrogen transfer between the caboxyls of the C-2 position(A) and the C-1' position(B)



Isotope Technique (^{14}C , ^{131}I) for Safety Analysis of Domestic Solid Waste Disposal Site in Jakarta, Indonesia- A Case Study

Syafalni (Corresponding author) & I. Abustan

School of Civil Engineering, Universiti Sains Malaysia

Seri Ampangan, 14300 Nibong Tebal, Pulau Penang, Malaysia

Tel: 60-4-599-6291 Fax: 60-4-541-009 E-mail: cesyafalni@eng.usm.my

M. Tadza Abdul Rahman

Malaysian Nuclear Agency

Abstract

Bekasi is one of city around Jakarta which has been developed for the last 10 years. In the south of Bekasi placed sanitary landfill area for domestic solid waste of Jakarta Metropolitan as a Disposal Site. The objective of the present study is to evaluate the location of Bantar Gebang Bekasi solid waste disposal site for safety analysis. The geohydrological parameters are determined by using isotopes techniques (^{14}C , ^{131}I) to study the shallow groundwater characteristics of the site. From the results of ^{14}C the direction of groundwater movement is found to be from South to the North and turned to North West of Jakarta at Jakarta Center. From radiotracer method (^{131}I) the direction of shallow groundwater in the rainy is observed to be from the disposal site to the surrounding area and the Ciketing canal which flows to the North. For the dry season from the disposal site to the surrounding area. The results from environmental isotopes and hydrochemistry analysis indicate that the pollutants from the site have given an impact to the surrounding area of disposal site which was shown by migration of nitrate. It is recommended that the decision maker should give high priority to the geology, geohydrology and environmental pollution studies for consideration of disposal site for the safety of sanitary landfill.

Keywords: Isotope, Safety, Disposal

1. Introduction

There is worldwide a growing awareness and concern of governments, communities and industry about the risks to people and the environment from the location and operation of sanitary landfill and disposal sites for domestic solids waste. The identification, assessment and management of health and environmental risks are now recognized as essential elements for orderly economic and social development (Lederman, 2007). The development of the city will increase the demand to clean water according to demand of the town. At the same time that is also happened by improvement of contamination of surface and ground water, especially shallow ground water which is resulted by human activities.

Environmental safety analysis represent processes considering environmental condition and participate society in course of decision making from development of a project or an activity. Research by using isotopes technique for environmental safety analysis of a waste disposal site covers predicting the origin, direction, and rate of shallow groundwater movement with the aid of mathematical model. A few researches on investigation of groundwater pollution by using isotopes techniques are available in the literature. Fritz et al. (1976) has developed environmental isotope method of ^{18}O and deuterium as movement indicator of leachate water from sanitary landfill. Shivanna et al. (1998) applied the isotopes technique to investigate groundwater pollution in India. In Frankfurt, Germany, Begey et al. (1995) using radioactive tracer ^{131}I to determine hydrodynamic parameter. And for Tandia et al. (1998) research about origin, process and migration nitrate compounds in the aquifers of Dakar region, Sinegal.

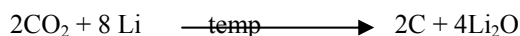
The development carried out in Bekasi district at the last 20 years may followed by growing demand of water to the area. In general the water demand is usually met directly from underground using small and big capacities of pump. The location of disposal site for domestic solid waste Jakarta Metropolitan has been operation since 1987. One of the serious problems is movement of polluted water containing dangerous pollutants from the disposal site to shallow and

groundwater system around the location. Therefore, the decontamination technique as a remedy and early protection of shallow ground water can be applied for the present disposal site. In the present research environmental safety analysis using isotopes technique carried out for the site by using isotopes approach (^{14}C , ^{131}I) and mathematical model for pollutant transport. The objective of the study is to evaluate the location of Bantar Gebang Bekasi solid waste disposal site for safety analysis in order to protect the shallow groundwater around the disposal site from leachate water pollutant.

2. Methodology

2.1 ^{14}C -Dating analysis

Analysis of C-14 is performed by converting BaCO_3 into C_6H_6 in a benzene synthesis unit. The Chemical reactions are:



The radioactivity of C-14 in benzene compound is measured by a normal procedure with liquid scintillation counter. Thus, the observed ^{14}C distribution in the BEKASI is expressed in percentage of modern carbon, i.e. the carbon content in 1 gram modern carbon of 1950 (13.56 ± 0.06 dpm) with oxalic acid standard RM49. The age of groundwater is evaluated by using formula (Clark et al., 1997):

$$t = 8267 \ln \text{Co}/\text{C} \quad (1)$$

where, C = the value of % modern carbon of the sample and

Co = the initial carbon-14 content

The ^{14}C values calculated for adjusted age is obtained by correction of Co, i.e. :

$$\text{Co} = \left[\frac{100 (\delta - \delta_c)}{\delta_G - \delta_c - \epsilon} \right] \times (1 - 2\epsilon/1000) \quad (2)$$

where, δ is the C-13 content of carbonate species dissolved in sample, δ_c is that of aquifer carbonate, δ_G is that of the soil CO_2 at the time of recharge and ϵ is the fractionation factor between bicarbonate and soil CO_2 . The value adopted for the calculation are $\delta_c = 0$, $\delta_G = -25 \pm 1\%$, $\epsilon = 8 \pm 0.5\%$

2.2 Method of Single Well

Measurements of directions and velocity of groundwater flow are conducted by using single well technique in which the boreholes of 3 inches diameter are made as injection and measurement points. Experiments are conducted by injection of ^{131}I tracer of quantity 1 mCi, in the form of KI, soon followed by counting of the location background. Then the measurement of tracer can be done after it is mixed in the well for about 1 day. Counting of tracer response is done by using gamma scintillation detector (NaI(Tl)). It consists of a collimator (Figure 1) with a scale and a flow meter in order to measure the total count from the borehole. For every borehole, counting is conducted to the North, South, West, East, North-West, North-East, South-West, and the South-East directions. Measurement of Darcy velocity is done by measuring the change of concentration or activity of radiotracer ^{131}I at the same well at certain time by using the same instrument (Syafalni et al. 1997).

Measurement of Darcy velocity (filtration velocity) by dissolution method is based on the decreasing of concentration at certain time as mathematically:

$$v_f = \frac{\pi r_1^2 \alpha t \ln \text{Co}/\text{C}}{\alpha} \quad (3)$$

in which

$$\alpha = \frac{4K_1}{\{K_1[1+(r_1/r_2)^2] + K[1-(r_1/r_2)^2]\}} \quad (4)$$

where:

v_f = filtration velocity

r_1 = inside well radius

r_2 = outside well radius

C_0 = initial concentration $t=0$

C = tracer konsentrasi at time t

t = time

K_f = hydraulic conductivity screen

K = hydraulic conductivity aquifer layer

For calculation of K_f (cm/detik) for plastic screen can be done empirically using 0,1f. And f concerning the percentage of opening screen. When value of $K \ll K_f$ so that K was neglected and the value of α is not influenced by the hydraulic conductivity of aquifer (International Atomic Energy Agency, 1983).

2.3 Method of Double Well

The double well method can be used for determination of characteristics of aquifer by pumping it to one particular well and injection of radiotracer ^{82}Br or ^{131}I to the other well. The degradation of water level and the response of radiotracer are observed at regular intervals. The radiotracer is injected at receiver borehole and the response was observed at the other borehole by using counting scintillation system (NaI(Tl)). From the result of water level, pumping time and response of radiotracer is evaluated for determination of aquifer characteristics such as effective porosity and dispersivity coefficient by using pollutant transport model and by Dupuit equation (Todd, 1980).

3. Results and Discussion

3.1 Bekasi groundwater flow direction

The experiments have been conducted for a period from January 2001 to July 2002 using carbon dating ^{14}C , ^{18}O , and ^2H along with analysis of hydrochemistry for Bekasi area and its surroundings and evaluation of geohydrology data. The results show that the groundwater of this area has 4 layers of aquifer and the direction of groundwater flow is from the South to North and from the North, turn to the left (North-West direction) as shown in isoage-contour of Bekasi groundwater (Figure 2). The analysis of hydrochemistry presented by Ruchiyat et.al.(1997) using ions Ca^{+2} , Mg^{+2} , Na^+ , K^+ , HCO_3^- , SO_4^- , and Cl^- also shows that the origin of Bekasi groundwater is from South Bekasi. The results indicate that the location of disposal site will contribute to a very wide contamination in the North (which covers North Bekasi and North Jakarta) and mainly in part of East Jakarta that have relation with Bekasi groundwater. It has already been found from the evaluation of the location safety assessment, that the decision of the above site was made without considering the origin of groundwater, groundwater movement, and migration of leachate of solid waste coming from biological decay of domestic waste of Jakarta and without considering geology aspects or environmental hydrogeology contamination of the area (Syafalni et al., 2001, 2002, 2003).

3.2 Shallow groundwater flow direction

The results of radiotracer method (^{131}I) that supported by environmental isotope method (^{18}O , ^2H) and analysis of hydrochemistry (ion Ca^{2+} , Mg^{2+} , Na^+ , K^+ , Fe^{3+} , HCO_3^- , SO_4^- , Cl^- , and NO_3^-) could predict the direction of movement of shallow groundwater around disposal site Bantar Gebang Bekasi as well as the mixing processes by leachate. The results indicate that the migrations of ion have extended about 3 km toward North of disposal site. The NO_3^- migration is accelerated by existence of Ciketing channel through disposal site to the North which perhaps will affect shallow ground water in this area. This area is a ground water recharge of Bekasi which is evaluated from protection zone of ground water (Syafalni et al. 2003).

From radiotracer method (^{131}I) with single well and double well techniques it is found that shallow ground water moves locally at three locations namely, Desa Sumur Batu, Desa Cikiwul and Desa Ciketing. The shallow groundwater movement of Sumur Batu, which is located North of disposal is to North-West at rainy season and to South-East at dry season. Desa Cikiwul which is located west of disposal site show opposing movement with that of Sumur Batu. Desa Ciketing shows same movement direction at both the seasons, that is to South-West (Figures 3.a and 3.b). The above results indicate that movement of shallow groundwater in the disposal area is influenced by solid waste accumulation at the site and exploitation of groundwater around it by industrial and domestic wells which also can cause leachate water flowing out of disposal site. This situation is very critical as the surrounding area of disposal site represent dynamic and expanding area.

Moreover the migration and movement of pollutant in this area could be simulated by using classic method and computer program by using disposal characteristics data (Table 1). The simulation results show good agreement with the realistic shallow groundwater movement of this area.

Hence it can be concluded that, there is significant dispersion of pollutants from the disposal site to its surroundings. If proper remedial actions are not taken, in the long run, these pollutants will contaminate the groundwater of Bekasi and north- east of Jakarta.

4. Safety analysis of disposal site

Protection of ground water from contamination is the key objective of disposal siting. The following short-term activities are required to be conducted as part of disposal siting:

- 1) Geodesy and infrastructure of location: covering mapping, land status, system of transportation and building, study of energy resources and water resources.
- 2) Geology and mechanics of land covering; identify of layers and structure of land, study of stability of surface and subsurface, and measuring of characteristic of land for each layer
- 3) Hydrology and geohydrology covering study of surface, study of leakage and ground water, inclusive of old age groundwater determination.
- 4) Research of migration with tracer to evaluate natural barrier
- 5) Supporting activity (meteorology measurement).

The long-term activities required include monitoring of ground water level, measurement of pollutant movement around Disposal site, meteorology measurement, and study of prevention and treatment of pollutants from disposal system. These requirements are not yet fulfilled for Disposal system at Bantar Gebang, Bekasi.

5. Conclusion

The isotopes technique (^{14}C and ^{131}I) is successfully applied to study the ground water characteristics of a typical waste disposal site near Jakarta, Indonesia. The results of ^{14}C dating are also supported by single and double well method for calculation of pollutant movement in the study area. The following conclusions may be drawn from the result analysis:

- 1) Ground water of Bekasi comes from the South of disposal site and moves to the North and then turns to North-West at centre of Jakarta.
- 2) The movement of shallow groundwater around the disposal site is highly influenced by hydrology and groundwater exploitation by domestic, and industrial wells.
- 3) The decision maker of the disposal site is advised to give high priority to geohydrology, environmental geohydrology contamination and to determine the location of Disposal site on the basis of environmental safety analysis.
- 4) Shallow groundwater of disposal site and the surrounding area have been contaminated by leachate water which is proved by ^{18}O , ^2H , hydrochemistry, and nitrate content in the area of investigation.

Acknowledgment

We would like to acknowledge our colleagues at CAIRT, National Atomic Energy Agency, Dr. H Md. Azamathulla (REDAC, Universiti Sains Malaysia) for discussion and suggestion and USM Shorten Grant (304.PAWAM.6035265) for supporting the publication.

References

- Begey B. M. and Cargnellutti, M. (1995). Groundwater model for management and remediation a highly polluted aquifer (organo-chlorine) in urban area, using radioactive tracers (^{131}I) for hydrodynamic parameters and dispersivity measurement. *Isotopes in Water Resources Management (Proc. Sym. Vienna, 1995)*. IAEA, Vienna, (2):229-248.
- Clark I. D., P. Fritz. (1997). *Environmental Isotopes in Hydrology*, Lewis Publishers, New York.
- Fritz P., Matthes., G., and Brown., R.M. (1976). Deuterium and Oxygen-18 as indicators of leachwater movement from a sanitary landfill, *Interpretation of Environmental Isotope and Hydrochemical Data in Groundwater Hydrology, (Proc. of an Advisory Group meeting, Vienna, 1975)*. IAEA, Vienna: 131-142.
- International Atomic Energy Agency. (1983). *Guidebook on nuclear techniques in hydrology*. Technical Report Series No. 91. IAEA. Vienna.
- Luis Lederman (2007). Guidelines for integrated risk management in Large Industrial Area. IAEA. Vienna.
- Ruchijat S., and Syamsul Hadi. (1997). Penelitian potensi air tanah daerah Jonggol- Bekasi, Jawa Barat. DGTL Dep. Pertambangan & Energi. Bandung.
- Shivanna K., S.V. Navada, K. M. Kulkarni, U.K. Sinha, S. Sharma. (1998). Application of isotopes techniques to investigate groundwater pollution in India, *Application of isotope techniques to investigate groundwater pollution*, IAEA-TECDOC-1046, Vienna: 167-184.
- Syafalni, Satrio, Indrojono and Darman. (1997). Teknik Radioperunut untuk mempelajari karakteristik air tanah dangkal di PPTA Pasar Jumat. *Risalah Pertemuan Ilmiah APISORA*. PAIR-BATAN. Jakarta
- Syafalni, M. Sri Saeni, Satrio and Djiono, (2001). Penelitian daerah imbuhan air tanah Bekasi dengan teknik hidrisotop. *Risalah Pertemuan Ilmiah APISORA*, PAIR-BATAN. Jakarta.

Syafalni, M. Sri Saeni, Soedodo Hardjoamidjojo and Hidayat Pawitan. (2002). Metode isotop alam untuk studi asal usul dan migrasi polutan nitrat dalam air tanah dangkal Tempat Pembuangan Akhir (TPA) Bantar Gebang Bekasi. *Majalah BATAN*, Vol XXXV. No.3/4, Jakarta.

Syafalni, M. Sri Saeni, Soedodo Hardjoamidjojo, Hidayat Pawitan and Satrio. (2003). Studi air tanah cekungan Bekasi dengan metode hidroisotop. *Risalah Pertemuan Ilmiah APISOR*. PAIR-BATAN, Jakarta.

Tandia A. A., C. B. Gaye, A. Faye. (1998). Origin, process and migration nitrate compounds in the aquifers of Dakar region, Sinegal, *IAEA-TECDOC-1046*.

Todd, D. K. (1980). *Groundwater Hydrology*. (2nd ed.), John Wiley & Sons, New York.

Table 1. The result of shallow groundwater characteristics at Bantar Gebang Disposal Site (February and May 2002)

Locations	Flow directions		Darcy velocity (m/s)		Hydraulic conductivity (m/day)	Dispersivity (α_L) (m)	Effective Porosity (n_{eff})
	February 2002	May 2002	February 2002	May 2002			
Desa Sumur Batu (A)	North-West	South- East	6.72×10^{-8}	1.84×10^{-8}	2.264	0.5157	0.137
Desa Cikiwul (B)	South- East	West	1.03×10^{-7}	9.8×10^{-8}	8.061	0.5864	0.124
Desa Ciketing Udik(C)	South-West	South-West	1.18×10^{-7}	1.27×10^{-7}	14.515	0.55	0.131

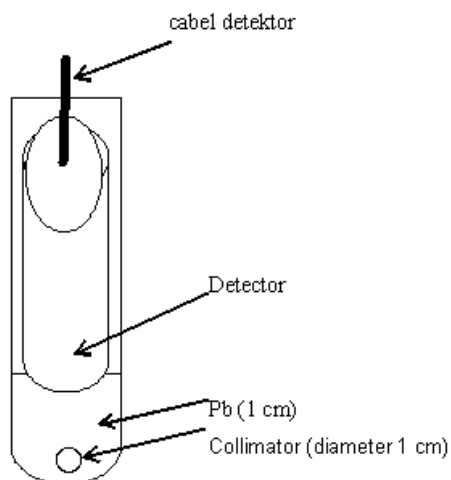


Figure 1. The Single well techniques for groundwater flow measurements

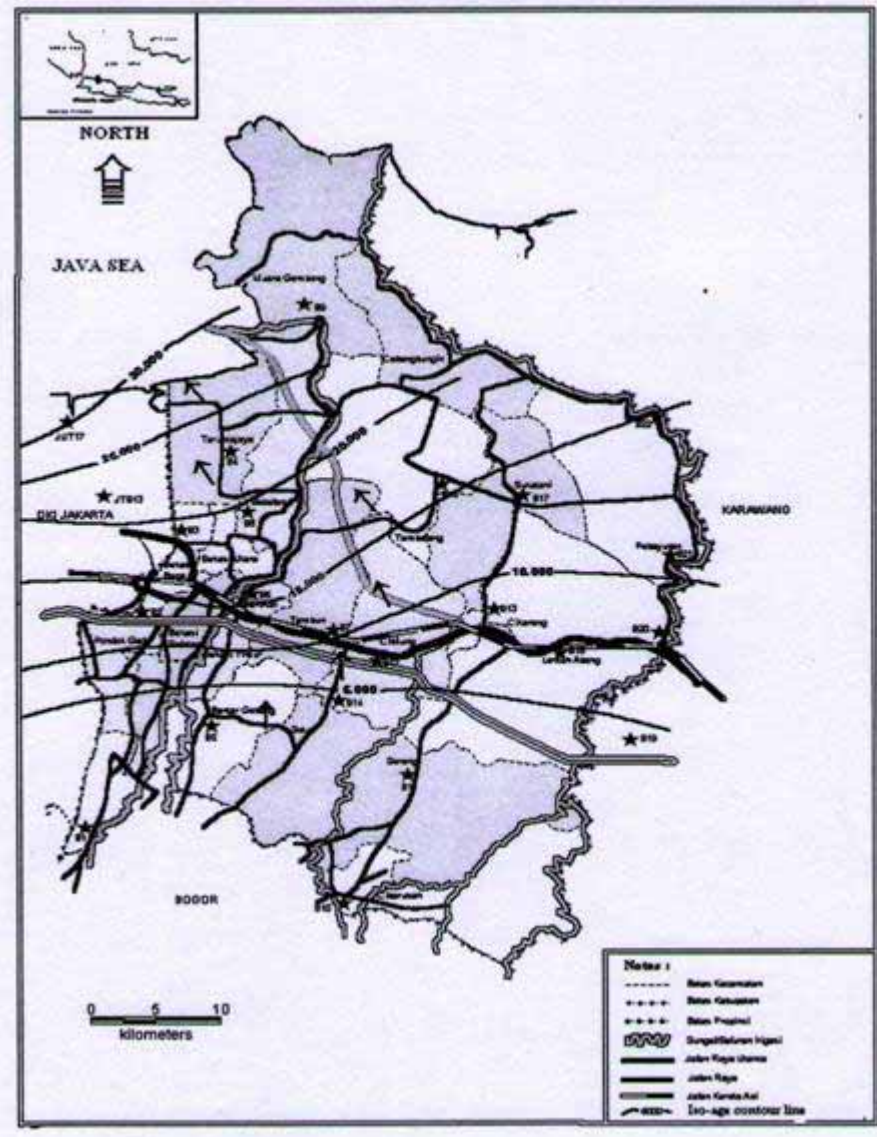


Figure 2. Iso-age map for Bekasi groundwater (Syafalni et al. 2001)

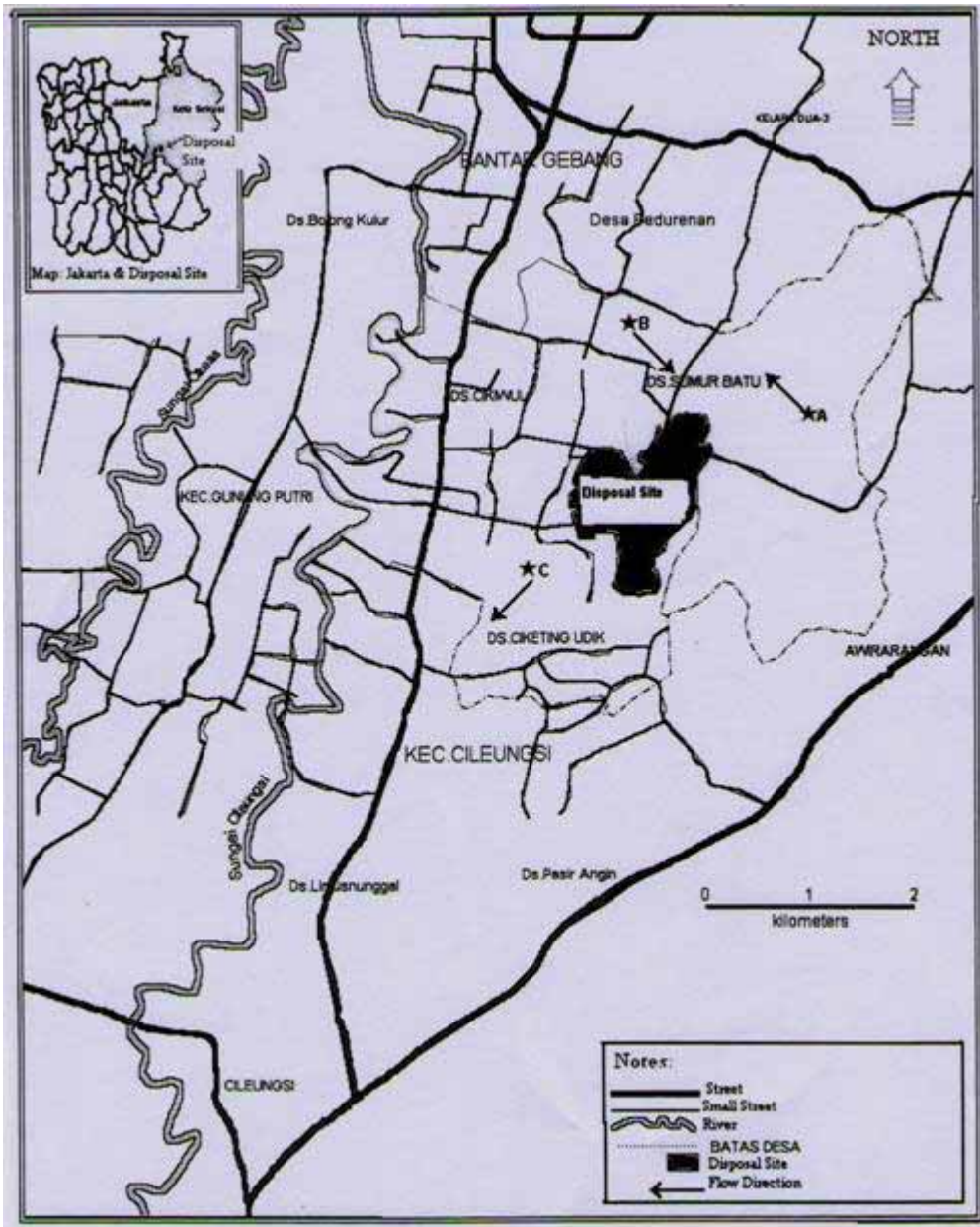


Figure 3a. Shallow groundwater flow directions at rainy season (February 2002)

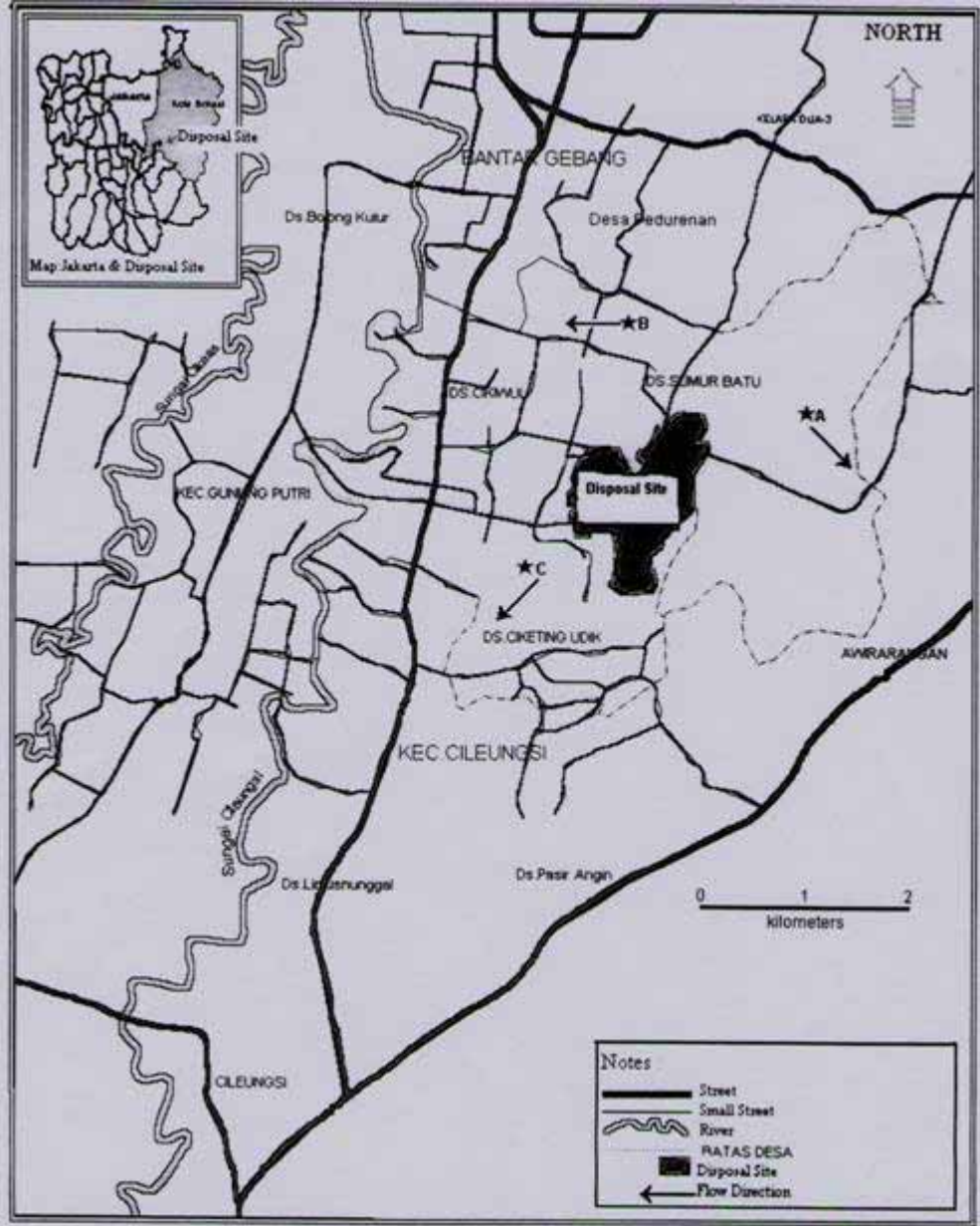


Figure 3b. Shallow groundwater flow directions at dry season (May, 2002)



Positioning Control of Unmanned-plane based on Regional Feature Matching

Jianghong Li

School of Power and Energy, Northwestern Polytechnical University

Xi'an 710072, China

Tel: 86-29-8846-0464 E-mail: jhli@nwpu.edu.cn

Liang Chen

School of Power and Energy, Northwestern Polytechnical University

Xi'an, Shaan'xi 710072, China

Tel: 86-29-8846-0464 E-mail: xbgdxxs@163.com

Yuanhu Cai

School of Power and Energy, Northwestern Polytechnical University

Xi'an 710072, China

Tel: 86-29-8846-0464 E-mail: caiyh@nwpu.edu.cn

Abstract

Positioning control of UAV is one of the research areas of autonomous navigation. Regional feature matching algorithm is commonly used in the positioning control of UAVs. This paper proposes a regional feature matching algorithm, in which edges and gray-levels within image regions are extracted. The correspondences between regional features are then obtained in terms of invariant moments and chain-code representation of regions. The transformation parameters are estimated based on the centers of gravity of regions. Experimental results show the effectiveness of the proposed algorithm using salient regional features.

Keywords: UAV, Image matching, Edge, Regional features

1. Introduction

The aerial imaging system of UAV usually captures some salient regions (e.g., pool, square, farm field .etc). These regions have stable and prominent characteristics, and similar image features (e.g., grey-levels, textures, edges, etc.). In addition, they often have regular geometrical shape and the area of each region is often in a certain range. An image recorded by aerial imaging system of UAV usually contains a small number of regional features. The regional features and the relative positions between regions can be used for matching images in positioning control of UAV. In this paper, we propose a regional feature matching algorithm, in which the regional features are extracted at first (square, region center of gravity, shape, invariant rectangular) and then the centers of gravity of regions are utilized as control points to estimate the transformation parameters between images.

2. Proposed Algorithm

There are two major problems in regional feature matching, i.e., (1) how to reliably extract the salient regional features and describe them. The real physiognomy with much interference is very complex so that the regional feature extraction is not an easy task. (2) How to use the features to achieve accurate estimation. In order to extract regional features, regions are required to be segmented from the image using image segmentation technique. Here we segment the image into different regions according to unique means so that such regions have no intersection and each region has consistent gray-levels. The details of image segmentation are described as follows:

The image

$$\{f(x, y) | 0 \leq x \leq \max(x), 0 \leq y \leq \max(y)\} \quad (1)$$

is segmented into sub-regions f_1, f_2, f_3, \dots which satisfy the following requirements:

$$\bigcup_{i=1}^N f_i(x, y) = f(x, y) \quad (2)$$

namely, all the sub-regions constitute a whole image and f_i is a connected region.

$$f_i(x, y) \cap f_j(x, y) = \emptyset \quad (3)$$

means that there is no intersection between two sub-regions. f_i satisfies homogeneity requirement. The proposed algorithm combines the advantages of two segmentation methods, i.e., region growing and edge extraction, to achieve good image segmentation especially for complicated scene. Moreover, the proposed algorithm employs hierarchical search method based on image pyramid structure to improve the efficiency. The major steps of the proposed algorithm are shown in Figure 1. Specifically, the proposed algorithm first builds the pyramid structure, extracts the thick edges in the image, doing distance transform to edge image and choosing the obvious region, using the grey and edge as constraint to process region growth and getting region feature, calculating the region geometric feature and building the corresponding relation among region features, applying least square method to estimate the converted parameter in wide size which uses the region center of gravity as control point, choosing the sub-region with abundant features doing relevant matching to optimize parameter in thin size, at last getting the image change parameter.

3. Regional feature extraction

Image segmentation is not an easy task especially when the scene is quite complex. Single segmentation algorithm cannot gain satisfying segmentation result, and the combination of several segmentation algorithms is a key point of recent research. The region growing method is simple and robust, but it's a serial processing method. Therefore, its efficiency is low and the segmentation results are hard to control. Edge extraction is also a commonly used image segmentation method and consists of two main steps: edge detection and edge closing. Although edge extraction is effective, however, it's hard to find ideal close edges. This section describes the proposed image segmentation method that combines the advantages of region growing and edge extraction. The region growing mainly contains two parts: identification of seed point and growing rule. Usually, the seed point is identified by using some specific gray-level value, but it is hard to control the growing process. Because edge extraction can provide a rough segmentation result, it is able to control the region growing if region growing is confined to a finite region surrounded by edges. Using distance transform can choose the region with large area and highlight the important region feature. Furthermore, region growing is not only constrained by gray-level information, but also by edge characteristics. The segmentation process is summarized in Fig. 2.

Fig.3 shows an aerial image taken by UAV and Figure 4 depicts the edges extracted from the image shown in Fig.3.

Fig.5 shows the result of image edge processed by distance transform, in which, the larger the gray value is, the larger the value of both the distance change and the specific area of the region. Fig.6 (a) demonstrates the candidate regions obtained from Fig.5 and Fig.6(b) shows the large regions in distance transform, which are formed by deleting the edges and the regions with small areas from Fig.6(a).

Fig.7(a) depicts the regions obtained by processing the candidate regions using region growing and rejecting the regions with small area after growing. Fig. 7(b) shows the boundaries of extracted regions.

After applying morphological processing to the image shown in Fig.7(a), the final result of extraction is shown in Fig.8.

4. Estimation of Transformation parameters

This section uses two real aerial images with known-parameters to test the effectiveness of the proposed algorithm. These two images cover similar scene with different resolutions. Fig.9 is a real-time image with size 172*190, and Fig.10 is the referenced image with size 224*242.

The parameters selected in our experiments are: distance $L=3$, region area $S>30$, region growth $\mu=2$, distance constraint $d_t=1$. The above parameters are empirically chosen based on several experiments. Doing matching calculation to the extracted region features (the parameters applied in feature matching are: threshold of combined moment $T^d=0.07$, threshold of chain-code relevance T^c is 0.8) gets 7 corresponding regions, Table 1 shows the coordinates of the center of gravity of regions. The estimates of transformation parameters are: rotation factor is 21.0414 degree and proportion factor is 1.3444. The transformation equation of real-time image to referenced image is:

$$\begin{cases} x' = 47.9559 + 1.2548x - 0.4827y \\ y' = -44.3442 + 0.4827x + 1.2548y \end{cases} \quad (4)$$

RMS-Root Mean-Square Errors is a commonly used judge standard in matching accuracy, which is defined as:

$$\text{RMS} = \sqrt{\frac{\sum_{i=1}^N [(x' - x)^2 + (y' - y)^2]}{N}} \quad (5)$$

$$\begin{cases} x' = t_x + x \cos \theta - y \sin \theta \\ y' = t_y + x \sin \theta + y \cos \theta \end{cases} \quad (6)$$

In this paper, we use RMS to measure the matching accuracy. Table 2 lists the matching errors of the centers of gravity of corresponding regions. It is seen from Table 2 that the average matching error of all the 7 control points is 1.2883, the maximum error of a single point is 1.9206, which proves the matching algorithm has excellent matching accuracy.

5. Conclusions

This paper proposes a image matching algorithm based on region features for positioning control of UAV and its accuracy has been proved by experiment. Furthermore, a regional features extraction method using edge and image grey information as constrain is proposed which applies region growing and extracts the region with comparatively large area. Experiments have proved the algorithm can be used in solving the extraction of regional features of complicated scene.

References

- Goshtasby, G. C. Stockman and C. V. Page. (1986). A region-based approach to digital image registration with subpixel accuracy. *IEEE Trans. on Geoscience and Remote Sensing*, 1986, 24(3): 390-399.
- Hui Li, B. S. Manjunath and S. K. Mitra. (1995). A contour-based approach to multisensor image registration. *IEEE Trans. on Image Processing*, 1995, 4(3): 320-334.
- J.P. Fan, D.K.Y. Yau, A.K. (2001). Elmagarmid and W.G. Aref. Automatic image segmentation by integrating color-edge extraction and seeded region growing. *IEEE Trans. on Image Processing*, 2001, 10: 1454-1466.
- R. Adams and L. Bischof. (1994). Seeded region growing. *IEEE Trans. on PAMI*, 1994, 16: 641-647.
- S. Dinggang and H. S. Horace. (1999). Discriminative Wavelet Shape Descriptors for Recognition of 2-D Patterns. *Pattern Recognition* 1999, 32: 151-165.
- S.A. Hojjatoleslami and J. Kittler. (1998). Region growing: a new approach. *IEEE Trans. on Image Processing*, 1998, 7(7): 1079-1084.
- Xiaolong Dai and S. K. Khorram. (1999). A teature-based image registration algorithm using improved chain-code representation combined with invariant moments. *IEEE Trans. on Geoscience and Remote Sensing*, 1999, 37(5): 2351-2362.
- Zhang yujin. (2000). *Graph engineering (above): graph process and analysis*. Beijing: Tsinghua University Press, 2000.
- Zhong kongde. (1996). *Signal processing*. Beijing: Tsinghua University Press.

Table 1. corresponding control point

Control point pair	Real-time image		Referenced image	
	x	y	x'	y'
1	74.6599	169.3019	59.2050	202.2111
2	56.3765	143.1000	50.0167	162.7242
3	57.1597	126.4958	58.7467	141.6800
4	65.1743	98.3527	81.4457	109.5950
5	106.2676	171.5282	99.1567	220.5187
6	72.2512	50.0171	113.0793	53.9287
7	87.6023	89.4678	114.6169	110.2338

Table 2. RMS error of control point

Control point	1	2	3	4	5	6	7
X	0.7097	0.3959	0.1281	0.8143	0.6558	1.3926	0.0742
Y	1.9206	0.2957	0.2919	0.9321	1.6638	0.6363	0.0291
RMS	1.2883						

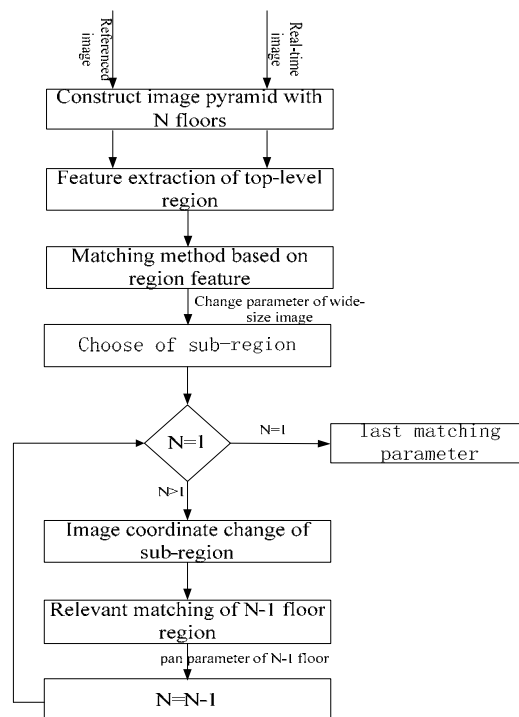


Figure 1. algorithm processing

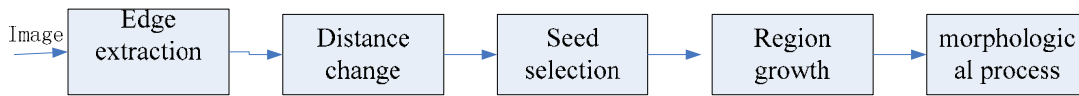


Figure 2. extract process of region characteristics



Figure 3. aerial photography

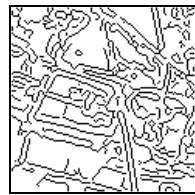


Figure 4. result of edge extraction



Figure 5. result of distance change

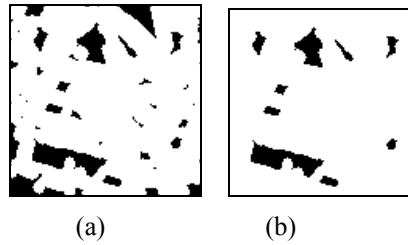


Figure 6. extraction of candidate region

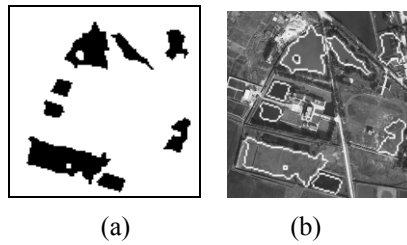


Figure 7. extraction results of region characteristics

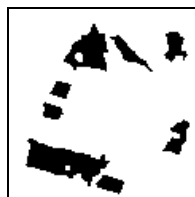


Figure 8. ultimate extraction results



Figure 9. real-time image



Figure 10. referenced image



Retrieval of SST Algorithm Coefficients at South China Sea

Ng Hou Guan, Mohd. Zubir Mat Jafri & Khiruddin Abdullah

School of Physics, Universiti Sains Malaysia

11800, Minden, Penang, Malaysia

Tel: 60-4-653-3888 E-mail: nghouguan@yahoo.com, mjafri@usm.my, khirudd@usm.my

The research is financed by USM grant under Graduate Research Scheme of Research University.

Abstract

The current operational sea surface temperature (SST) algorithm coefficients were not suitable to be applied at South China Sea. Therefore, the algorithm coefficients that could be specially used for South China Sea were required to be calibrated. The study was conducted to find a set value of MCSST and NLSST algorithm coefficients that were suitable to be used at South China, and also to investigate the effect of the haze to SST algorithm. The calibrated algorithm with the new set of coefficients was proved to give more accurate result compared to SST data calculated by using SST algorithm in ENVI. The SST algorithm of ENVI was cited from the NOAA SST algorithm that applied the global algorithm coefficients. Besides that, the study also showed that the haze would affect the SST algorithm.

Keywords: SST, Algorithm coefficients, South China Sea, Calibration, Validation

1. Introduction

There are many SST algorithms introduced, but they are the generally multi-channel (MCSST) and nonlinear (NLSST) algorithms. MCSST algorithm was developed by McClain and it is based on linear differences in brightness temperatures. It was NOAA's operational algorithm for several years. The latest NOAA's operational SST algorithm is NLSST algorithm.

In this study, the MCSST and NLSST algorithm coefficients were retrieved at South China Sea. The algorithm coefficients were derived from the regression between the SST in-situ data at China Sea and nearly coincident satellite data. The satellite data used for regression was sensor zenith angle (θ) and brightness temperature of channel 4 (T_4) and channel 5 (T_5) for AVHRR image.

The SST data was estimated by MCSST and NLSST algorithms with new calibrated algorithm coefficients. The algorithms were also compared with the SST algorithm of ENVI. The new calibrated algorithm was proved to be more accurate than SST algorithm of ENVI. The validation was done with the SST in-situ data. The RMSE of MCSST and NLSST was 3.13 and 5.54, while the RMSE of SST estimated by SST of ENVI was 9.59. The histograms of the SST in-situ data, SST data calculated by the new calibrated MCSST algorithm, NLSST algorithm and algorithm of ENVI were generated with statistical software, Minitab. The histograms showed that the SST data calculated by MCSST and NLSST algorithm were closer to the SST in-situ data compared with the SST data calculated by SST algorithm of ENVI. The SST maps of MCSST algorithm, NLSST algorithm and algorithm of ENVI were generated. The SST map of in-situ data was interpolated by the software PCI with the input of SST data acquired from the site. The maps were generated so that the distribution of the SST data of each algorithm could be compared visually.

After that, another study was done to investigate the validity of the calibrated SST algorithm after a certain period of time. Besides that, the effect of haze to the algorithm was also investigated. The calibration was done at South China Sea by 13 July 2004, 10 July 05 and 11 July 05. The validation was done at South China Sea by 12 July 04, 10 Aug 04, 10 July 05, 12 July 05, 12 Aug 05, 13 Aug 05, 6 Sep 06, 7 Oct 06 and 6 Nov 06. The RMSE between the SST data estimated from the algorithm and measured SST data was compared.

The results showed that the new calibrated SST algorithm was applied well throughout the year except the occurrence of the haze.

2. Data and Methodology

South China Sea was chosen as the study area. The AVHRR image was acquired from Malaysian Center of Remote Sensing (MACRES). The AVHRR data was obtained with the date of July 12, 2004, and at the time of 03:31 UTC. The

SST in-situ data obtained from Department of Environment (DOE), Malaysian Meteorology Department (MMD) and project of "Research on the Seas and Islands of Malaysia" (ROSES).

First of all, radiometric calibration was done by converting the digital number to brightness temperature for channel 4 and channel 5 of AVHRR data. After that, the geo-coding and geometrical corrections were performed. The missing data, cloudy and sun-glint pixels, and the land area were masked. The good pixels were only used for SST algorithm coefficients retrieval. The good pixels were pixels free from masking.

The SST in-situ data were then interpolated by using the method of point interpolation with Kriging method by PCI software. The SST in-situ data were used as the input vector layer in PCI algorithm. The data of sensor zenith angle and brightness temperature from AVHRR image and SST data from the image produced by the Kriging algorithm of PCI at coincident location were then calibrated to produce the algorithm coefficients of MCSST and NLSST algorithms. The SST data of new calibrated MCSST and NLSST algorithms were then compared with the SST data calculated by the algorithm of ENVI with the histograms, box-plot and the value root mean square error (RMSE).

After that, the second study was done to investigate the effect of the haze and the validity of the algorithm throughout the year. The AVHRR data was downloaded at the date shown in Table 1 from Comprehensive Large Array-data Stewardship System (CLASS) website. The SST data were acquired from DOE, MMD, ROSES and MODIS website.

The DN on channel 4 and channel 5 of AVHRR file were converted to brightness temperature. All the parameters: brightness temperature and sensor zenith angle and sea surface temperature data were geo-referenced by using a large amount of ground control points (GCP) points appended in the level 1b file. The data of brightness temperature and sensor zenith angle from AVHRR file was used. These parameter were then stacked and the subset area of the intersection of these parameter were then extracted.

The tool of Layer Stacking in ENVI V4.4 was used to stack all the parameters with the output file range encompasses file overlap. Then all the bad pixels, cloudy pixels and land pixels were filtered for each file. The land area was colour-coded with green colour, cloud and missing data were in yellow colour and sun-glint area in red colour (Figure 1).

The algorithm coefficients were calibrated at 10 July 2004, and then the algorithm coefficients were validated at 12 July 2004, 10 August 2004, 10 July 2005, 12 July 2005, 12 August 2005, 13 August 2005, 6 September 2006, 7 October 2006 and 6 November 2006. After that, the algorithm coefficients were calibrated at 10 July 2005 and 11 July 2005, and then validated at 12 July 2005, 12 August 2005, 13 August 2005, 6 September 2006, 7 October 2006 and 6 November 2006.

The first 50 data of T_4 , T_5 , and θ used for algorithm calibration at 10 July 2005 were shown in Table 2. The first 50 data used for validation the algorithm at 12 July 2005 were shown in Table 3. The algorithm coefficients retrieved after calibration and root mean square difference were calculated.

3. Result and Discussion

The MCSST and NLSST algorithm coefficients were retrieved by using regression analysis with statistical software, Minitab. The MCSST algorithm retrieved was:

$$\text{MCSST} = a_0 (T_4) + a_1 (T_4 - T_5) + a_2 (T_4 - T_5)(\text{Sec } \theta - 1) + a_3 \quad (1)$$

where the algorithm coefficients:

$$a_0 = 0.231, a_1 = -1.20, a_2 = -2.15, a_3 = 240$$

The NLSST algorithm retrieved was:

$$\text{NLSST} = b_0 (T_4) + b_1 (T_4 - T_5) (\text{MCSST}) + b_2 (T_4 - T_5) (\text{Sec } \theta - 1) + b_3 \quad (2)$$

where the algorithm coefficients:

$$b_0 = 0.183, b_1 = 0.00282, b_2 = -0.26, b_3 = 249$$

The histograms of SST calculated by MCSST algorithm, NLSST algorithm, ENVI's algorithm and SST in-situ data were shown in Figure 2. The MCSST data was approximately in the range of 27°C and 31°C, while the NLSST data was approximately in the range of 24°C and 36°C. However the range of SST data calculated by algorithm of ENVI was approximately in the range of 15°C and 30°C. The range value of ENVI's SST was obviously shifted to the left compared to SST in-situ data that was in the range of 27 to 36°C. The MCSST was in the range inside the SST in-situ data. The range of NLSST data was quite similar with the SST in-situ data if compared with other algorithms.

The box plots were then generated (Figure 3). The SST data estimated by the algorithm of ENVI was obviously lower than SST in-situ data. Besides that, the algorithm also generated many outliers that were illogically out of the bound. Overall, the SST data estimated MCSST and NLSST algorithms were better to be used to estimate SST in-situ data.

The RMSE of each algorithm was then calculated. The RMSE of MCSST and NLSST was 3.13 and 5.54, while the

RMSE of SST estimated by SST of ENVI was 9.59. The comparatively low value of RMSE for MCSST and NLSST algorithms showed they were more accurate than ENVI's algorithm. This was because the ENVI's algorithm not specially designed for the area of South China Sea. However the calibrated MCSST and NLSST algorithms were specially designed for South China but had no guarantee can be used for other places out of South China Sea.

The SST maps of each algorithm and in-situ data were then generated by ENVI (Figure 4, 5, 6 and 7).

After that the next study done was to calibrate the SST algorithm 10 July 2004, 10 July 2005 and 11 July 2005.

The algorithm calibrated at 10 July 2004 was

$$\text{MCSST} = 303 + 0.00114 T_4 + 0.0246(T_4 - T_5) + 0.772 (T_4 - T_5) \text{ (Sec } \theta - 1) \quad (3)$$

$$\text{NLSST} = 303 + 0.00113 T_4 + 0.000081 (T_4 - T_5) \text{ MCSST} + 0.772(T_4 - T_5) \text{ (Sec } \theta - 1) \quad (4)$$

The algorithm calibrated at 10 July 2005

$$\text{MCSST} = 299 + 0.0165 T_4 + 0.842* (T_4 - T_5) - 0.221* (T_4 - T_5) \text{ (Sec } \theta - 1) \quad (5)$$

$$\text{NLSST} = 299 + 0.0165 T_4 + 0.00274* (T_4 - T_5) \text{ MCSST} - 0.219* (T_4 - T_5) \text{ (Sec } \theta - 1) \quad (6)$$

The algorithm calibrated at 11 July 2005

$$\text{MCSST} = 303 + 0.0107 T_4 - 0.213(T_4 - T_5) - 0.932 (T_4 - T_5) \text{ (Sec } \theta - 1) \quad (7)$$

$$\text{NLSST} = 303 + 0.0108 T_4 - 0.000699 (T_4 - T_5) \text{ MCSST} - 0.934(T_4 - T_5) \text{ (Sec } \theta - 1) \quad (8)$$

The RMSE between the SST in-situ and SST estimated by the algorithm calibrated at 10 July 2004, 10 July 2005 and 11 July 2005 was shown in Table 4, Table 5 and Table 6. The MCSST 1 in the Figure 8 referred to the MCSST algorithm calibrated at 10 July 2004, while the MCCST 2 and MCSST 3 referred to the MCSST algorithm calibrated at 10 July 2005 and 11 July 2005 respectively.

Overall, the RMSE was lower than 2.5, except the date at 6 September and 7 October 2006. This may be due to the effect of South East Asian Haze. The hazy days started around the end of the August 2006 and came to the end around the end of October 2006 as the monsoon season was coming.

The SST algorithms were not applied well at the hazy days. The RMSE was shooting high at 6 September and 7 October 2006, but decreased abruptly at 6 November 2006. Therefore, the SST algorithm was not working well on hazy days. Therefore the new algorithm that was adapted to the changes of the air quality was required to improve the performance of the existing SST algorithm.

The RMSE of MCSST was higher because the algorithm was calibrated by combining AVHRR data at two different times: 02:06 UTC and 03:47 UTC. This might be the source of errors while doing the validation.

4. Conclusion

The new calibrated MCSST and NLSST algorithms were more suitable to estimate the SST data compared with the SST in-situ data. It was verified by using the histograms, box plot and RMSE. The RMSE of MCSST and NLSST algorithms were 1.671 and 1.355 respectively. They were far lower compared with RMSE of ENVI's algorithm, 6.797.

Overall, the SST algorithms can be used at South China Sea along the whole year unless the occurrence of haze. The South China that is situated near the equator has an equatorial climate. The equatorial climates do not pronounce four seasons. It is hot and wet throughout the year. The atmosphere parameters were affected only when the occurrence of haze. Therefore the calibrated SST algorithm coefficients were valid to be used along the whole year at South China Sea. However, the SST algorithm coefficients should be recalibrated after the occurrence of haze.

References

- Abdullah, K., Nasirun, M.S., Alui, B., Ruslan, R., and Yusuff, M. (1997). Cloud Masking Techniques for AVHRR data for Oceanographic Applications in Malaysia., *Proceedings of ACRS*.
- Barton, I.J. (1995) Satellite-derived sea surface temperatures: Current Status, *J. Geophys. Res.*, 100, 8777-8790.
- Bindoff, N.L., J. Willebrand, V. Artale, A. Cazenave, J. Gregory, S. Gulev, K. Hanawa, C. Le Quéré, S. Levitus, Y. Nojiri, C.K. Shum, L.D. Talley and A. Unnikrishnan (2007) Observations: Oceanic Climate Change and Sea Level. *Climate Change 2007: The Physical Science*.
- Brisson, A., P. LeBorge and A. Marsouin. (2002). Determination of SST algorithms for NOAA-17. O&SI SAF/Low & Mid Latitudes report.
- Buettner, K. J. K. and C. D. Kern (1965). The determination of infrared emissivities of terrestrial surfaces. *Geophys. Res.*, 70, 1329-1337.
- Coakley, J.A. and Bretherton, F.P. (1982) Cloud Cover from high-resolution scanner data; detecting and allowing for partially filled of view. *Journal of Geophysical Research*, 87, 4917-4932.

- Franca, G.B. and Cracknell, A.P. (1994) Retrieval of Land and Sea Surface Temperature using NOAA-11 AVHRR data in northeastern, Brazil. *International Journal of Remote Sensing*, 15, 1695-1712.
- Franca, G.B. and Cracknell, A.P. (1995) A simple cloud masking approach using NOAA AVHRR daytime time data for tropical areas. *International Journal of Remote Sensing*, 16, 1697-1705.
- Kachi, M.H. Murakami, K. Imaoka and A. Shibata (2001) Sea Surface Temperature Retrieved from TRMM microwave imager and visible infrared scanner. *J.Meteorol Soc. Japan*.
- Karl, H.S. (1988). Observations over the Oceans. *Satellite Monitoring of the Earth*, 148-202.
- Kidwell, K. (1991). NOAA Polar Orbital Data User's Guide. *NOAA NESDIS Technical Report*, USDoC, Washington, DC.
- Kidwell, K.B. (1998). NOAA Polar Orbiter Data Users' Guide (TIROS-N, NOAA-6, NOAA-7, NOAA-8, NOAA-9, NOAA-10, NOAA-11, NOAA-12, NOAA-13, NOAA-14) November 1998 Revision. NOAA/ NESDIS/ NCDC.
- Kriebel, K.T., Saunders, R.W., Gesell, G. (1989). Optical Properties of Clouds Derived from Fully-Cloudy AVHRR Pixels. *Beitr. Phys. Atmosph*, 62, 165-171.
- Mc Millan, L.M. (1975). Estimation of sea surface temperature from two infrared window measurements with different absorption. *J.Geophys.Res*, 80, 5113-5117.
- Ng, H. G., M. Z. MatJafri, et al. (2008). Improvement on Masking and Flagging Technique on Reducing SST Residual. *Aerospace Conference, 2008 IEEE*.
- Planet, W. G. (ed.) (1988). Data Extraction and Calibration of TIROS-N/ NOAA Radiometers. *NOAA Technical Memorandum NESS 107 – Rev. 1* U.S. Department of Commerce , National Oceanic and Atmospheric Administration, Wahington, D.C.
- Prabhkara, C. G., Dalu, and V. G. Kunde. (1974). Estimation of sea surface temperature from remote sensing in the 11-13 μ m window region. *J. Geophys. Res.*, 79, 5039-5044.
- Saunders, P. M. (1967b): Aerial measurement of the sea surface temperature in the infrared. *J. Geophys. Res.*, 72, 4109-4117.
- Saunders, P. M. (1968). Radiance at sea and sky in the infrared window 800-1200 cm-I. *j. Opt. Soc. Amer.*, 58, 645- 652.
- Saunders, R.W. (1986) An automated scheme for the removal of cloud contamination from AVHRR radiances over western Europe. *International Journal of Remote Sensing*, 7, 867-886.
- Walton, C.C. (1987). Non-linear multichannel algorithms for estimation sea surface temperature with AVHRR satellite data. *J. Appl. Meterol*, 27, 115-124.
- Walton, CC., W.G.Pichel, and J.F. Sapper. (1998). The development and operational application of non-linear algorithms for the measurement of sea surface temperatures with the NOAA polar-orbiting environmental satellites. *J. Geophysics.Res.*, 103, 27999-2807.
- Wu, X., W.P.Menzel and G.S. Wade. (1999). Estimation of sea surface temperature using GOES-8/9 radiation measurement. *BULL. Amer. Meor. Soc.*, 80, 1127-1138.
- Závody, A.M., C.T. Mutlow, and D.T. Llewellyn-Jones. (1995). A radiative transfer model for sea surface temperature retrieval for the Along-Track Scanning Radiometer. *J. Geophys. Res.*, 100, 937-952.

Table 1. The data and time for the data used in calibration and validation

Date	Time	
	AVHRR	MODIS
10 July 2004	02:37 UTC	03:33UTC, 03:45 UTC
12 July 2004	03:33 UTC	03:30 UTC
10 Aug 2004	02:34 UTC	03:00 UTC
10 July 2005	02:06, 03:47 UTC	03:10 UTC
11 July 2005	03:28 UTC	03:50UTC, 03:55 UTC
12 July 2005	03:05 UTC	03:00 UTC
12 Aug 2005	02: 58 UTC	02:10 UTC ,02:15 UTC , 03:50 UTC, 03:55 UTC
13 Aug 2005	02:35 UTC	03:00 UTC
6 Sep 2006	02:07 UTC	03:15, 03:20 UTC
7 Oct 2006	01:56 UTC	02:35 UTC
6 Nov 2006	02:03 UTC	02:45UTC

Table 2. The data used for calibration

latitude	longitude	SST	θ	T ₄	T ₅
4.65637	108.111	31.56	60.4412	287.411	285.398
4.65637	108.120	31.58	60.5203	287.781	285.525
4.64733	108.111	31.58	60.4412	287.535	285.271
4.64733	108.120	31.60	60.5203	287.288	284.888
3.51722	104.096	27.99	46.0001	281.306	279.662
3.43585	104.169	33.05	46.4749	289.702	287.253
3.41777	104.151	32.75	46.4070	289.217	286.876
3.40873	104.151	32.79	46.4070	289.217	286.876
3.07422	104.251	31.53	47.2246	277.524	275.201
3.05614	104.242	31.74	47.2246	273.477	272.276

Table 2. Continued

latitude	longitude	SST	θ	T4	T5
3.04710	104.242	31.79	47.2246	274.025	272.979
2.81203	107.089	31.67	58.6621	289.796	287.394
2.75779	107.107	31.81	58.7387	289.326	286.897
2.75779	107.116	31.75	58.7387	289.326	286.897
2.75779	107.125	31.74	58.7387	289.326	286.897
2.69450	105.720	31.79	53.9015	289.891	287.403
2.69450	105.729	31.82	53.9015	289.891	287.403
2.68546	105.720	31.78	53.9015	289.891	287.403
2.68546	105.729	31.80	53.9015	289.891	287.403
2.62217	107.308	31.57	59.5100	287.717	285.763
2.61313	107.317	31.65	59.5100	287.717	285.763
2.59505	107.326	31.79	59.5877	287.471	285.254
2.58601	107.326	31.83	59.5877	287.471	285.254
2.58601	107.335	31.80	59.5877	287.471	285.254
2.53177	107.381	31.68	59.8213	289.436	287.029
2.53177	107.390	31.71	59.8213	289.436	287.029
2.53177	107.399	31.75	59.8213	289.436	287.029
2.53177	107.408	31.78	59.8213	289.436	287.029
2.46848	106.560	31.80	57.1431	267.989	265.594
2.46848	106.569	31.81	57.1431	267.989	265.594
2.46848	106.578	31.82	57.1431	267.989	265.594
2.46848	106.587	31.83	57.1431	267.989	265.594
2.45944	104.543	32.18	49.2281	289.808	287.398
2.45944	104.552	32.16	49.2281	289.808	287.398
2.45944	106.560	31.77	57.1431	256.092	254.409
2.45944	106.569	31.77	57.1431	256.092	254.409
2.45944	106.578	31.78	57.1431	256.092	254.409
2.44136	104.561	32.30	49.2973	288.957	286.769
2.43232	104.552	32.25	49.2973	287.110	285.117
2.43232	104.561	32.25	49.2973	287.365	285.376
2.42328	104.552	32.21	49.2973	289.194	286.766
2.42328	104.561	32.20	49.2973	287.110	285.117
2.42328	104.570	32.17	49.3666	287.110	285.245
2.41424	104.561	32.16	49.3666	287.233	284.862
2.41424	104.570	32.12	49.3666	287.233	284.862
2.24246	104.077	32.31	47.3725	278.466	276.160
2.23342	104.059	32.59	47.3042	277.008	274.925
1.86274	107.655	31.93	61.0826	287.860	285.503
1.86274	107.664	31.95	61.0826	287.860	285.503
1.86274	107.673	31.96	61.0826	287.860	285.503

Table 3. The data used for validation

θ	T_4	T_5	SST	MCSST	NLSST
40.7447	286.513	284.207	305.36	304.887	304.914
40.8106	283.760	281.359	305.51	304.806	304.833
46.8051	290.408	288.255	305.52	304.724	304.751
46.8051	289.197	287.380	305.57	304.927	304.954
42.7756	281.340	279.654	305.79	305.082	305.108
36.8272	283.097	282.130	305.18	305.598	305.626
35.6009	283.717	281.482	305.85	305.081	305.107
8.7984	288.704	286.260	304.10	305.541	305.569
34.8929	281.560	280.833	304.95	305.709	305.737
55.3492	290.513	288.129	304.73	303.915	303.942
55.3492	290.392	288.004	304.73	303.910	303.937
55.5702	288.816	287.133	305.07	304.525	304.552
32.2772	283.975	281.892	305.02	305.240	305.267
55.6439	291.101	288.645	305.02	303.824	303.851
55.3492	287.823	286.136	304.98	304.527	304.554
55.6439	286.217	284.736	304.92	304.681	304.708
55.5702	284.008	283.056	304.89	305.154	305.181
55.5702	287.251	285.748	304.86	304.677	304.704
55.6439	287.251	285.748	304.83	304.673	304.699
55.5702	284.008	283.056	304.80	305.154	305.181
55.5702	284.008	283.056	304.77	305.154	305.181
55.5702	287.251	285.748	304.75	304.677	304.704
55.6439	287.251	285.748	304.71	304.673	304.699
55.4964	284.008	283.056	304.71	305.157	305.184
55.4964	287.374	285.367	304.75	304.216	304.242
55.4964	286.509	284.857	304.77	304.535	304.562
55.5702	286.509	284.857	304.77	304.530	304.556
55.5702	289.574	287.514	304.78	304.185	304.211
55.5702	289.574	287.514	304.79	304.185	304.211
55.6439	289.574	287.514	304.80	304.178	304.205
55.4228	288.844	286.508	304.80	303.934	303.960
55.4964	288.844	286.508	304.80	303.927	303.953
55.4964	290.541	288.140	304.80	303.885	303.911
55.5702	290.541	288.140	304.80	303.877	303.904
55.4964	288.844	286.508	305.58	303.927	303.953
55.4964	291.382	288.887	305.49	303.806	303.833
55.5702	291.382	288.887	305.39	303.799	303.826
54.9091	286.974	284.991	305.06	304.282	304.308
59.0439	286.453	284.864	305.84	304.328	304.355

Table 3. Continued

θ	T ₄	T ₅	SST	MCSST	NLSST
59.7438	289.281	286.888	304.90	303.390	303.416
59.6658	289.159	286.762	304.93	303.394	303.420
59.7438	288.427	286.131	305.22	303.489	303.515
59.7438	288.427	286.131	305.37	303.489	303.515
46.9615	283.221	281.372	305.52	304.835	304.861
59.6658	288.794	286.383	305.01	303.375	303.402
59.7438	289.159	286.762	304.99	303.383	303.410
59.6658	289.281	286.888	304.86	303.400	303.426
59.6658	289.281	286.888	304.90	303.400	303.426
59.7438	288.794	286.383	304.93	303.365	303.391

Table 4. The RMSE between SST in-situ and SST estimated by the algorithm calibrated at 10 July 2004

RMSE	MCSST	NLSST
12 July 2004	1.074 K	1.076 K
10 August 2004	1.667 K	1.665 K
10 July 2005	0.890 K	0.890 K
12 July 2005	1.215 K	1.150 K
12 August 2005	1.238 K	1.236 K
13 August 2005	1.220 K	1.120 K
6 September 2006	2.846 K	2.844 K
7 October 2006	1.785 K	1.783 K
6 November 2006	0.914 K	0.915 K

Table 5. The RMSE between SST in-situ and SST estimated by the algorithm calibrated at 10 July 2005

RMSE	MCSST	NLSST
12 July 2005	0.527 K	0.525 K
12 August 2005	1.576 K	1.568 K
13 August 2005	2.316 K	2.308 K
6 September 2006	3.840 K	3.832 K
7 October 2006	3.758 K	3.749 K
6 November 2006	1.790 K	1.783 K

Table 6. The RMSE between SST in-situ and SST estimated by the algorithm calibrated at 11 July 2005

RMSE	MCSST	NLSST
12 July 2005	0.964 K	0.952 K
12 August 2005	0.777 K	0.784 K
13 August 2005	0.758 K	0.773 K
6 September 2006	3.408 K	3.434 K
7 October 2006	3.756 K	3.784 K
6 November 2006	2.097 K	2.123 K

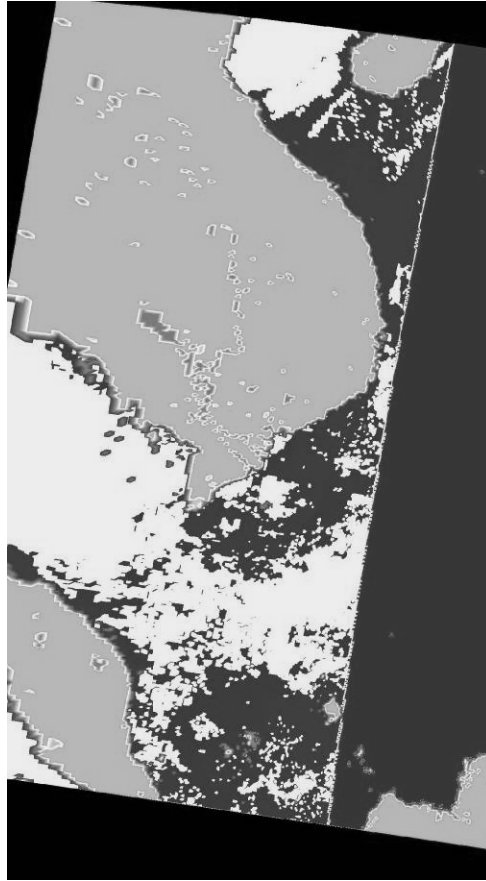


Figure 1. The masking of the land, cloud, sun glint and bad pixels

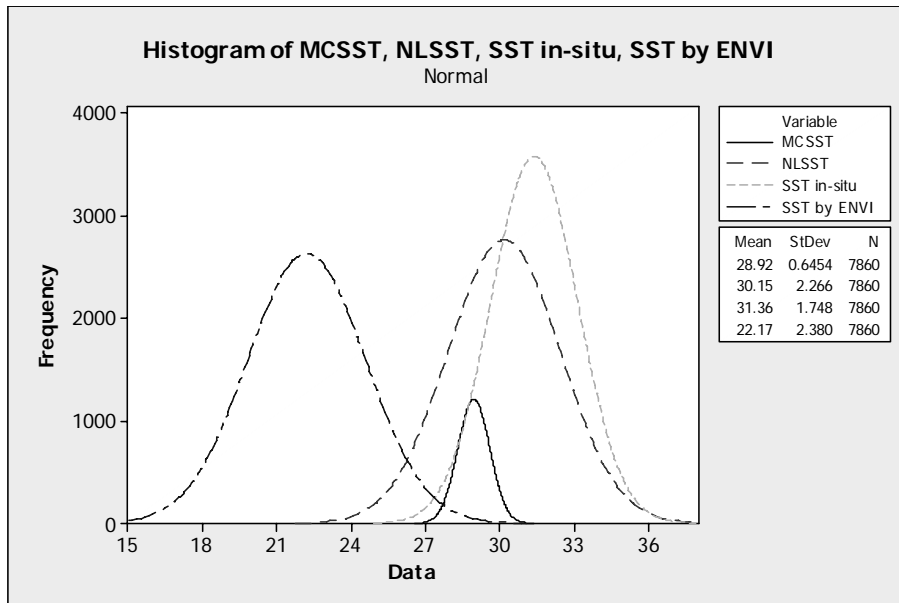


Figure 2. The histograms of SST calculated by MCSST algorithm, NLSST algorithm, ENVI's algorithm and SST in-situ data.

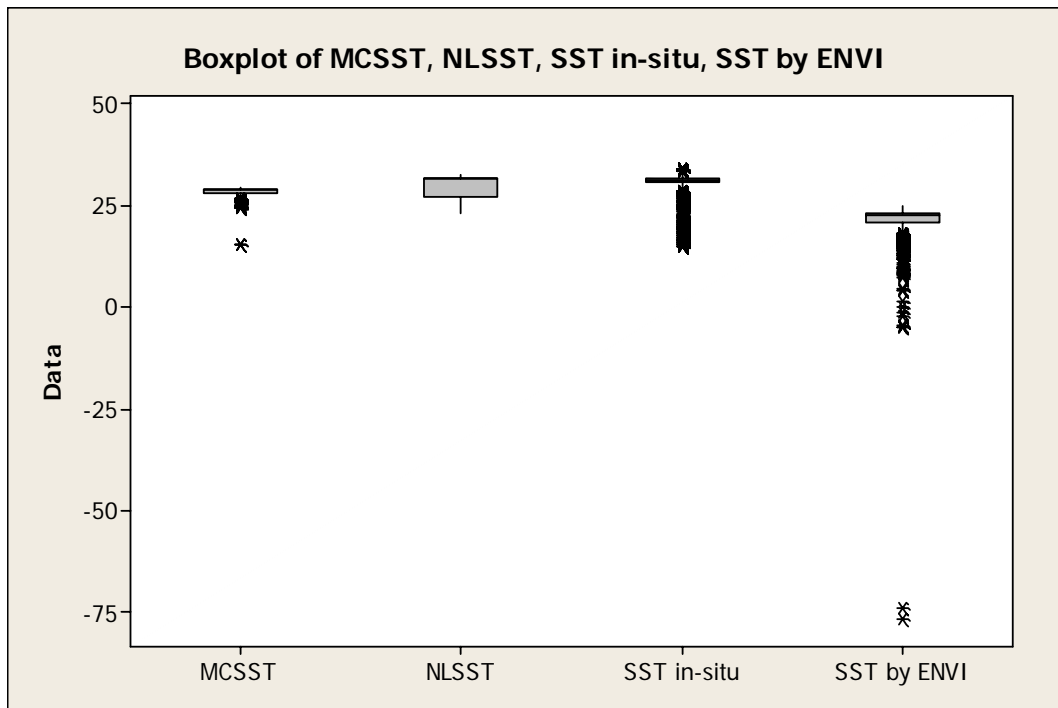


Figure 3. The box plot of SST calculated by MCSST algorithm, NLSST algorithm, ENVI's algorithm and SST in-situ data

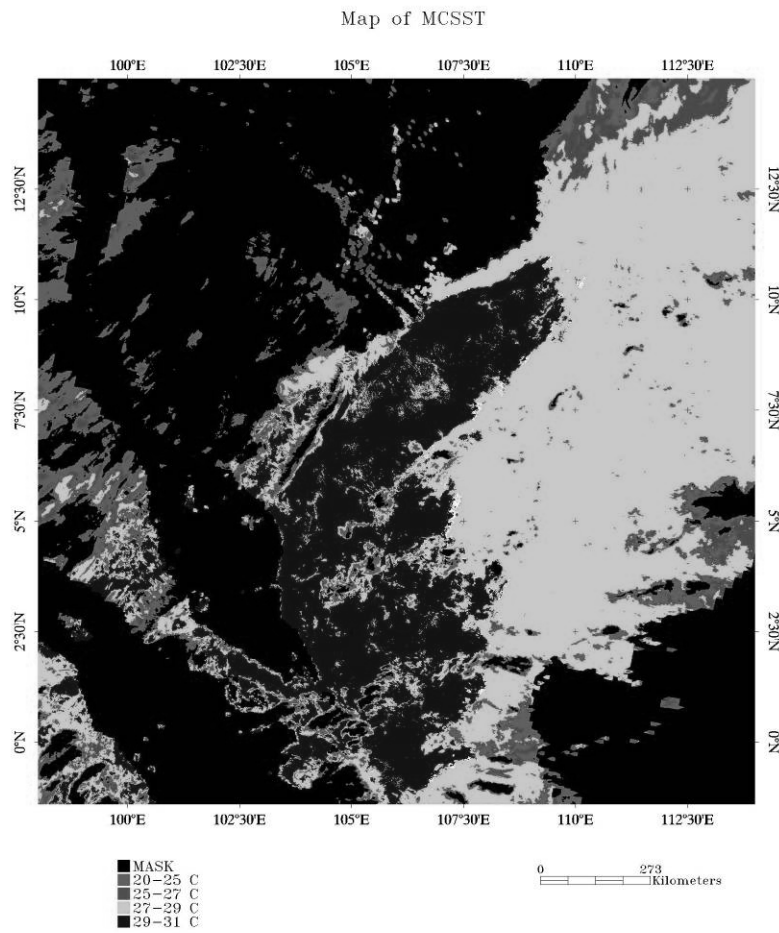


Figure 4. The map of MCSST with new calibrated coefficients

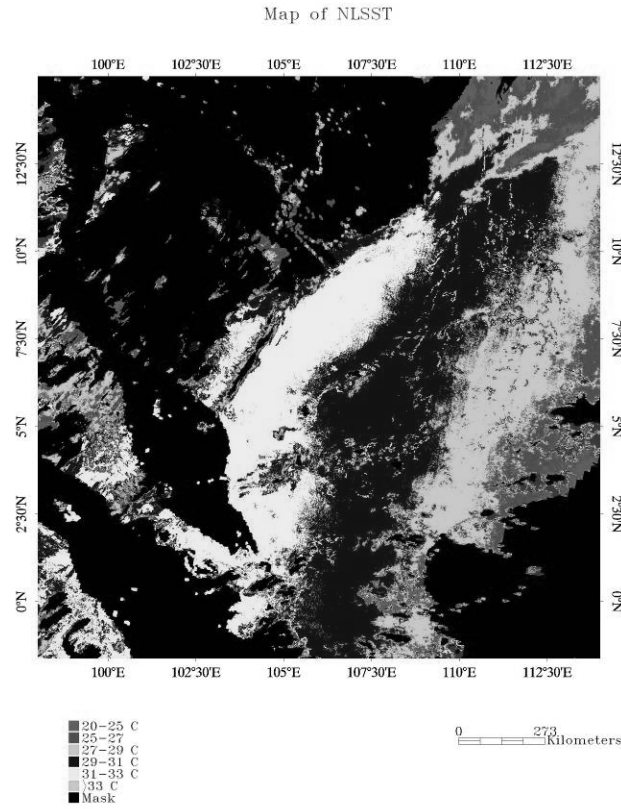


Figure 5. The map of NLSST with new calibrated coefficients

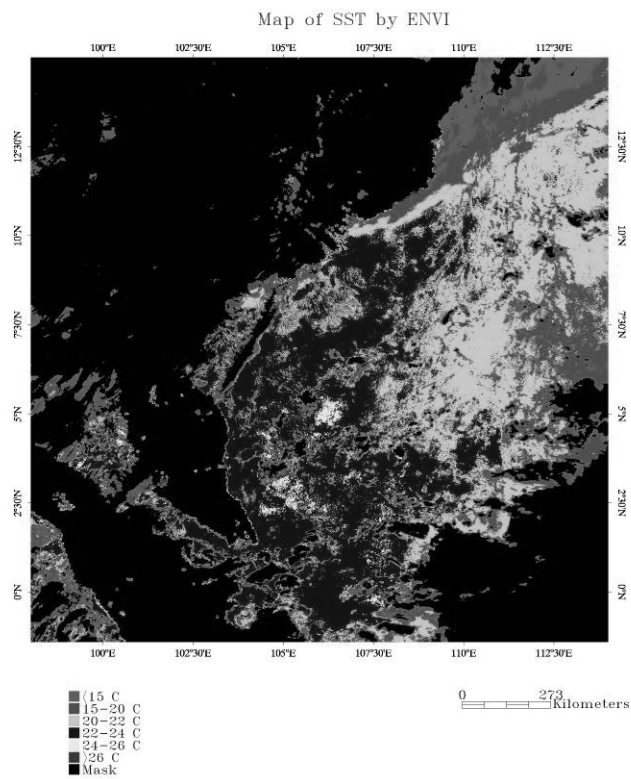


Figure 6. The map of SST generated by ENVI's algorithm

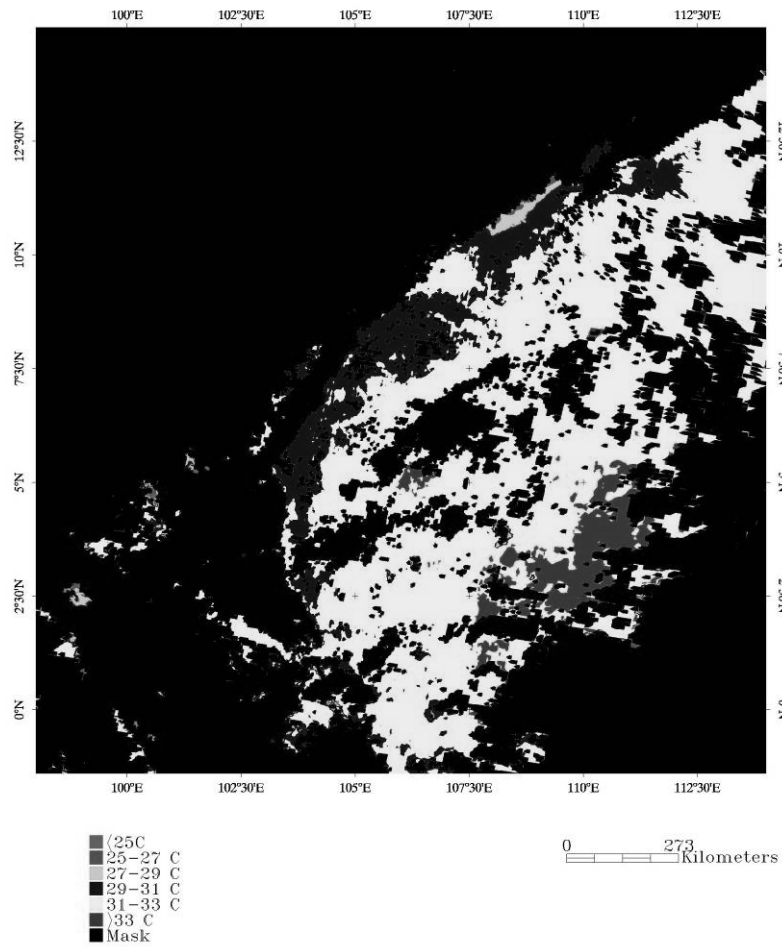


Figure 7. The map of SST generated by of SST in-situ data with Kringing interpolation

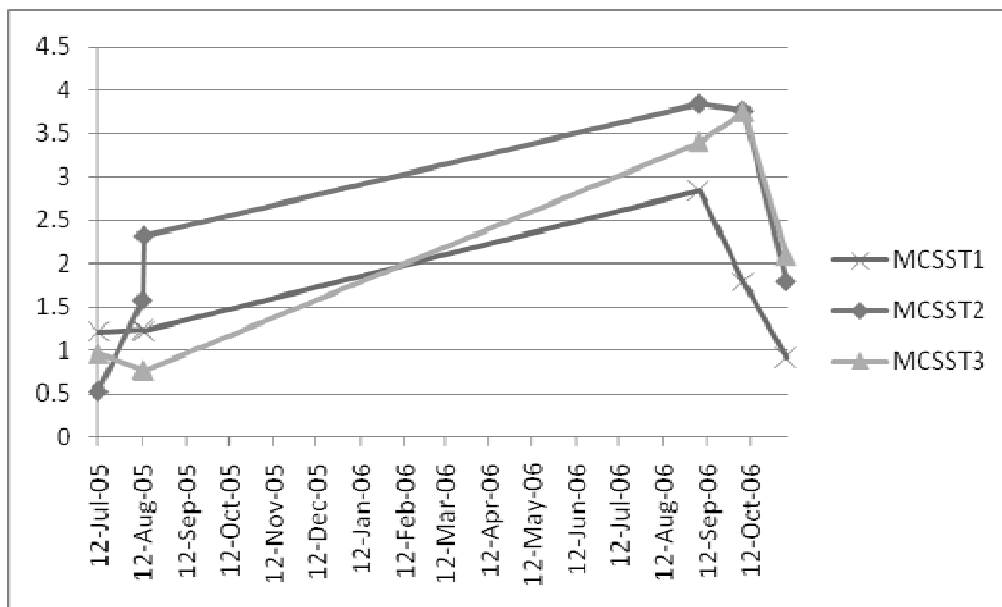


Figure 8. The trend of RMSE changes with time



Predicting Model of Traffic Volume Based on Grey-Markov

Yinpeng Zhang

Zhengzhou Municipal Engineering Design & Research Institute, Zhengzhou 450052, China

Abstract

Grey-markov forecasting model of traffic volume was founded by applying the model of GM (1,1) and Markov random process theory. The model utilizes the advantages of Grey-markov GM (1,1) forecasting model and Markov random process in order to discover the developing and varying tendency of the forecasting data sequences of traffic volume. The analysis of an example indicates that the grey-markov model has good forecasting accuracy and excellent applicability in predicting traffic volume.

Keywords: Grey theory, Grey-markov model, Prediction of traffic volume

1. Introduction

Generally, the planning of a highway is designed on the basis of the traffic volume prediction. The so-called definition of traffic volume prediction is to study and calculate the inside increase and change of traffic, and to obtain a volume in terms of design years according to the variety of transportation capacity and the development of economy and society in the past, present and future etc. Although many learners have processed large quantity of researches for predicting the traffic volume, the result is still bad. The transportation engineering is a complicated system, which includes many factors, many structural layers and many targets. The traffic information contains the obviously layer complexity of structure, the fuzzy relation of construction, the variety of development and the indetermination of coefficients and data. Because of the influence of some artificial factors, unaffectedly environmental change and the restriction of the technique methods at present, it leads to the result that the statistic or forecast data embrace some errors, mistakes, scarcity or fakes. So the complicated system of traffic volume prediction is a representatively grey problem (Zhang and Luo, 2001).

The grey model has been applied in the traffic volume prediction, and primarily makes use of model GM (1,1) to perform the forecast (Wen et al., 2006; Xue and Zeng, 2006). Because the solution of model GM (1,1) is an exponential curve that is smooth, it doesn't match with those data that are vibration sequences and its forecast accuracy is lower. The study object of markov transition model is a dynamic system which forecasts the future by analyzing the inside regulation of development in time to come, and it reflects the influence degree and laws which lies in the transition process of factors from one state to the other. The markov transition model is suitable for the solution to predict these stochastic data sequences that are steady, but in the realistic world these raw sequences are vibrating and changing in a certain variety trend. From the analysis above, we know that the model GM (1,1) and the markov model could be integrated with each other to forecast by their advantages. That is: model GM (1,1) can be used to forecast the change trend of data sequences, while the markov model can be used to decide the vibration regulation of their development, and both can be joined together to become a grey-markov forecast model. Since it makes full use of the old information given from these raw data and increases the forecast accuracy, the application of the grey-markov forecast model, which provides a new method to predict these greatly stochastic data sequences, has been improved further.

2. Establishment of the Mathematics Model

2.1 Model of GM(1,1)

The grey GM (1,1) model can make use of the discrete data series to establish a equation of grey continuous differential equation by adding these data from the first in Accumulating Generation Operator (AGO), and the equation can be solved to perform the forecast (Deng, 1990). Let $x^{(0)}(k)$ be a raw series, which is as follow:

$$X^{(0)}(k) = \{x^{(0)}(1), x^{(0)}(2), \dots, x^{(0)}(n)\}, k = 1, 2, \dots, n \quad (1)$$

Let $x^{(0)}$ accumulated adding once, and the accumulated generating series is obtained:

$$x^{(1)} = \{x^{(1)}(1), x^{(1)}(2), \dots, x^{(1)}(n)\} \quad (2)$$

where
$$x^{(1)}(k) = \sum_{i=1}^k x^{(0)}(i), k = 1, 2, \dots, n$$

By differentiating $x^{(1)}$, a whitened differential equation is obtained

$$\frac{dx^{(1)}}{dt} + ax^{(1)} = u \tag{3}$$

The whitened time-response of Eq. (3) is as follow (Deng 1990):

$$\hat{x}^{(1)}(k+1) = \left[x^{(0)}(1) - \frac{u}{a} \right] e^{-ak} + \frac{u}{a} \tag{4}$$

Let the solution $\hat{x}^{(1)}$ accumulate subtracting once, and the accumulated subtraction series is obtained:

$$\hat{x}^{(0)}(k+1) = \hat{x}^{(1)}(k+1) - \hat{x}^{(1)}(k) \tag{5}$$

The curve of $\hat{x}^{(0)}$ reflects the vibration trend of the raw series. Finally we can adopt the method of Deng (Deng, 1990) to check the model accuracy.

2.2 Grey markov chain

Let $\{X_n, n \in T\}$ be a markov chain, where $m, n \in T (n \geq 1)$ and $i, j \in L$ (L is called status series, then the expressing (Sha, 1994)

$$p_{ij}^{(n)} = P(X_{m+n} = j | X_m = i) \tag{6}$$

is called the n th step transition probability, and the matrix composed by $p_{ij}^{(n)}$ is called the n th step probability transition matrix of Markov chain, which is expressed as:

$$P^{(n)} = [p_{ij}^{(n)}]_{l \times l} \tag{7}$$

If the elements transition probabilities of markov chain are grey, it will be called a grey markov chain, and can be made up of a grey transition matrix (He and Bao, 1992). In the actual application, we know that it is difficult to make certain the values of transition probability for it lacks some information, but it is easy to have the information of grey zone $p_{ij}(\otimes)$ by studying the transition probability. When the transition matrix is a grey matrix, it is required that the

elements of whitenization matrix $\tilde{P}(\otimes) = [\tilde{p}_{ij}(\otimes)]_{l \times l}$ is provided that (1) $\tilde{p}_{ij}(\otimes) \geq 0, i, j \in L$;

$$(2) \sum_{j=1}^l \tilde{p}_{ij}(\otimes) = 1, i \in L .$$

When the preliminary distribution of a markov limited chain is $P(0) = (p_1, p_2, \dots, p_l)$, and the whitenization transition probability matrix is $\tilde{P}(\otimes) = [\tilde{p}_{ij}(\otimes)]_{l \times l}$, then we can get the next step distribution of the chain:

$$P(1) = P(0) \cdot \tilde{P}(\otimes) \tag{8}$$

The second step can be expressed as:

$$P(2) = P(1) \cdot \tilde{P}(\otimes) = P(0) \cdot \tilde{P}^2(\otimes) \tag{9}$$

The rest may be deduced by analogy, and the n th step distribution is shown as:

$$P(n) = P(0) \cdot \tilde{P}^n(\otimes) \tag{10}$$

From Eq. (10), it can be seen that we can easily forecast any future distribution of the system if we have already known the raw distribution and the grey transition probability matrix.

2.3 Grey-markov model

Let $x^{(0)} = \{x^{(0)}(1), x^{(0)}(2), \dots, x^{(0)}(n)\}$ be a raw data series. After we have checked the model accuracy, we get the

simulation sequence as: $\hat{x}^{(0)} = \{\hat{x}^{(0)}(1), \hat{x}^{(0)}(2), \dots, \hat{x}^{(0)}(n)\}$ by model GM(1,1). Let $\hat{y}(k) = \hat{x}^{(0)}(k)$, for a vibration sequence \hat{Y} which is a markov chain, we can divide it into l states according to the concrete circumstance, and its any state \otimes_i can be expressed as:

$$\otimes_i = [\tilde{\otimes}_{1i}, \tilde{\otimes}_{2i}], \tilde{\otimes}_{1i} = \hat{y}(k) + A_i, \tilde{\otimes}_{2i} = \hat{y}(k) + B_i, i = 1, 2, \dots, l \tag{11}$$

where A_i and B_i are constant, which can be decided by the difference between the forecast value and the raw data. \hat{Y} is a function which is changed in time, and so are the grey whitened elements of $\tilde{\otimes}_{1i}, \tilde{\otimes}_{2i}$.

If $N_{ij}(m)$ is the data number of the raw series which transfer m step from \otimes_i to \otimes_j , and N_i is the number of data that are in the grey zone \otimes_i , then we call:

$$p_{ij}(m) = \frac{N_{ij}}{N_i}, i, j = 1, 2, \dots, l \tag{12}$$

the m th step transition probability. The transition matrix $R(m)$ is as follow:

$$R(m) = \begin{bmatrix} p_{11}(m) & p_{12}(m) & \dots & p_{1l}(m) \\ p_{21}(m) & p_{22}(m) & \dots & p_{2l}(m) \\ \vdots & \vdots & \vdots & \vdots \\ p_{l1}(m) & p_{l2}(m) & \dots & p_{ll}(m) \end{bmatrix} \tag{13}$$

$R(m)$ reflects the transition regulation between different states and is the foundation of the forecast model of grey markov. We can predict the future trend of the system by studying the stochastic transition matrix $R(m)$.

In practical application, if the forecast values is to be placed in the zone \otimes_k , then investigate the k th line of the matrix $R(1)$ inside, and if $\max_j \{p_{kj}(1)\} = p_{kr}(1)$, we can conclude the next state of the system may transfer its state from \otimes_k to \otimes_r . If $R(1)$ has more than two lines whose probability values are same alike or close to each other and it is difficult to decide the next direction of the system with certain, it is needed to study and check the matrix $R(2)$ or $R(m)$ ($m \geq 3$). At the same time, it can decide the transition of the system by checking $R(1)$ or $R(m)$ ($m \geq 2$), and also be made sure the forecast zone $[\tilde{\otimes}_{1i}, \tilde{\otimes}_{2i}]$. Finally, the eventual forecast is in the middle point of the grey zone, then got:

$$\hat{Y}'(k) = \frac{1}{2}(\tilde{\otimes}_{1i} + \tilde{\otimes}_{2i}) \tag{14}$$

which also can be expressed as:

$$\hat{Y}'(k) = \hat{y}(k) + \frac{1}{2}(A_i + B_i) \tag{15}$$

3. Example Analysis

The data of a highway's traffic volume through 11 years are listed in Tab. (1).

3.1 Establishment of GM (1,1) model

From table 1, we get $x^{(0)} = \{7590, 7458, 7689, 8573, 8215, 8986, 9013, 10353, 11821, 12304, 13755\}$. After do them in AGO, we obtain $x^{(1)} = \{7590, 15048, 22737, 31310, 39525, 48511, 57524, 67877, 79698, 92002, 105757\}$. Then we can have two constants: $a = -0.0717448$, $u = 6151.22$.

By combining with Eq. (3), we can establish the model GM(1,1): $\frac{dx^{(1)}}{dt} - 0.0717448x^{(1)} = 6151.22$.

After solving the equation, time-response function can be obtained as:

$$\hat{x}^{(1)}(k+1) = 93327.4e^{-0.0717448k} - 85737.4.$$

From Eq. (5), it can be got: $\hat{y}(k) = \hat{x}^{(0)}(k+1) = \hat{x}^{(1)}(k+1) - \hat{x}^{(1)}(k)$.

The examination result of the prediction accuracy is as follow: $\bar{x} = 9614.27, S_1 = 2046.02, \bar{q} = 22.534, S_2 = 447.134$.

The post-examination margin ratio is as follow: $C = S_2 / S_1 = 0.218539 < 0.35$.

The probability of little error is as follow:

$P\{|q(k) - \bar{q}| < 0.6745S_1\} = P\{|q(k) - \bar{q}| < 1380.04\} = 1 > 0.95$ The accuracy grade of the forecast is excellent (Deng, 1990).

3.2 Compartmentalization of the prediction

According to the raw traffic volume and for simplification, the prediction values can be divided into four states by Eq. (11) as follows:

$$\otimes_1 = [\tilde{\otimes}_{11}, \tilde{\otimes}_{21}]: \tilde{\otimes}_{11} = \hat{y}(k) - 0.12\bar{x}, \tilde{\otimes}_{21} = \hat{y}(k) - 0.05\bar{x}$$

$$\otimes_2 = [\tilde{\otimes}_{12}, \tilde{\otimes}_{22}]: \tilde{\otimes}_{11} = \hat{y}(k) - 0.05\bar{x}, \tilde{\otimes}_{22} = \hat{y}(k)$$

$$\otimes_3 = [\tilde{\otimes}_{13}, \tilde{\otimes}_{23}]: \tilde{\otimes}_{11} = \hat{y}(k), \tilde{\otimes}_{23} = \hat{y}(k) + 0.05\bar{x}$$

$$\otimes_4 = [\tilde{\otimes}_{14}, \tilde{\otimes}_{24}]: \tilde{\otimes}_{11} = \hat{y}(k) + 0.05\bar{x}, \tilde{\otimes}_{24} = \hat{y}(k) + 0.12\bar{x}$$

$$\otimes_4 = [\tilde{\otimes}_{14}, \tilde{\otimes}_{24}]: \tilde{\otimes}_{14} = \hat{y}(k) + 0.05\bar{x}, \tilde{\otimes}_{24} = \hat{y}(k) + 0.12\bar{x}$$

where $\hat{y}(k)$ is the forecast traffic as model GM (1,1), and \bar{x} is the annual average traffic volume. If we show the values of the fact, the prediction $\hat{y}(k)$ and four states through these years, we will obtain a diagram listed as Fig.1 in which there are four parallel and symmetry band districts form the top to the bottom.

3.3 Calculation of the transition probability

From Fig. 1, we know that the number of raw sequence, which is in the zone of $\otimes_1, \otimes_2, \otimes_3, \otimes_4$, is $N_1=1, N_2=4, N_3=3, N_4=3$, and 0, 1, 0, 0 is the number of raw data from \otimes_1 to $\otimes_1, \otimes_2, \otimes_3, \otimes_4$ respectively by a step. If the rest may be deduced in the same way, we can calculate the number of raw transition data. Finally, we have

$p_{ij}(1)$ which makes up of the matrix $R(1) = \begin{bmatrix} 0 & 1 & 0 & 0 \\ 1/4 & 1/4 & 1/4 & 1/4 \\ 0 & 1/3 & 0 & 2/3 \\ 0 & 1/3 & 2/3 & 0 \end{bmatrix}$ by Eq. (12). According to $R(1)$, we can

forecast the transition state of the traffic volume in the future.

3.4 Decision of the prediction and vibration zone

By studying $R(1)$, we know that the average prediction of 2001 will mostly be in the vibration zone \otimes_3 , which is

$[14225.1, 14705.8]$. Then using formula (14) or (15), we have $\hat{Y}'(2001) = \frac{1}{2}(14225.1 + 14705.8) = 14465$. In the same

way, we can get $\hat{Y}'(2002) = 15283, \hat{Y}'(2003) = 16660, \hat{Y}'(2004) = 17641, \hat{Y}'(2005) = 19194$

4. Conclusion

The grey model GM (1,1) reflects the macroscopical regulation, the markov model shows the vibration development of the microcosmic system, and both not only have the mutual advantage but also can make full use of the information which is included in these raw data. Therefore, the forecasting grey-markov model has much higher accuracy, reliability and application in the traffic volume prediction. On the other hand, because the prediction accuracy is in line with the raw data series and the divided states, but there is not a given standard that can really unify and settle these problems, and the application of the model still needs a further research and improvement.

References

Deng, J. L. (1990). *Grey system theory tutorial*, Huazhong University of Science and Technology Press, Wuhan, China.

He, Y. and Bao, Y. D. (1992). Grey markov chain prediction model and the implication. *Systems Engineering Theory and Practice*, 1992(4): 34-37.

Sha, J. Z. (1994). *Marten decision programming and its application in management*, National Defence Industry Press, Beijing, China.

Wen, K. G., Qu, S. R. and Wang, J. (2006). An urban traffic flows prediction model based on system grey theory. *Transactions of Shenyang Ligong University*, 2006, 25(2): 11-14.

Xue, C. M. and Zeng, Y. K. (2006). On grey prediction model for road traffic freight volume. *Journal of Kunming University of Science and Technology (Science and Technology)*, 2006, 31(4): 98-103.

Zhang, X. T. and Luo, X. H. (2001). The application of grey theory and model in traffic volume prediction. *Highway*, 2001(8): 4-7.

Table 1. Historical Traffic Volume

Year	1990	1991	1992	1993	1994	1995	1996	1997	1998	1999	2000
AADT (n/d)	7590	7458	7689	8573	8215	8986	9013	10353	11821	12304	13755

AADT=Annual Average Daily Traffic

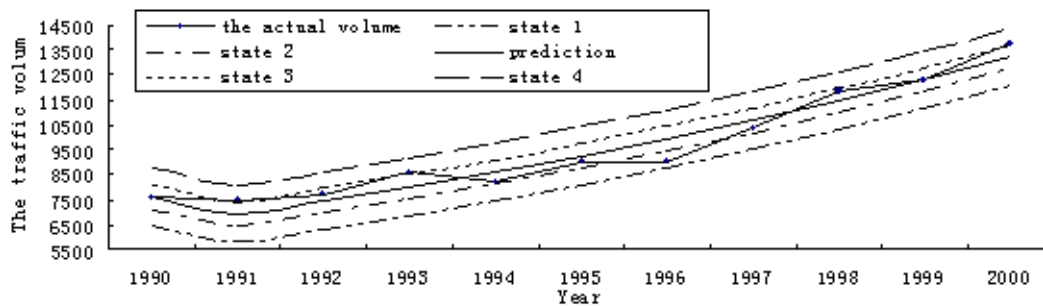


Figure 1. Annual Average Traffic Volume



Studies on Some Aspects of Jet Mixers I: Hydrodynamics

Prof .Dr. K.Saravanan

Head of Department, Department of Chemical Engineering
Kongu Engineering College, Perundurai-638052, Erode (DT), Tamil Nadu, India
Tel: 98-4-270-5656 E-mail: rumisivaesh@yahoo.com

N. Sundaramoorthy

Principal, The Kavery College of Engineering
Meacheri-636 453, Salem (District), Tamil Nadu
Tel: 90-03-828-823 E-mail: moorthysir@rediffmail.com

G. Mohankumar

Head of Department, Department of Petro-Chemical Engineering
Nandha Polytechnic College, Perundurai-638052, Erode (DT), Tamil Nadu, India
Tel: 99-42-498-882 E-mail: kgmkomardeepa@yahoo.com

N. Subramanian

Lecturer, Department of Chemical Engineering
Kongu Polytechnic College, Perundurai-638052, Erode (DT), Tamil Nadu, India
Tel: 97-8978-0967 E-mail: nsm_kpc@yahoo.co.in

Abstract

Mixing is one of the common unit operation employed in chemical industries. Conventional mixers are equipped with impellers but are expensive for mixing in large storage tanks and underground tanks. Jet mixers have become an alternative to impellers for over five decades in the process industry. For the design of jet mixers, the detailed hydrodynamics of the mixing process is not properly understood. In the present paper, hydrodynamic techniques are used to simulate jet mixing in a cylindrical tank. For this purpose, experiments were carried out to study the effects of various parameters such as nozzle diameter, jet position and jet velocity on mixing time. Results show that, for a given geometric arrangement, jet diameter is significantly more important in determining hydrodynamic characteristics of jet mixer. The results obtained give a good understanding of hydrodynamic aspects of mixing process in jet mixed tanks.

Keywords: Jet mixing, liquid hold up, Flow rate, Mixing time, Jet diameter, Jet position

1. Introduction

Mixing is one of the common unit operations employed in chemical industries. Mixing is usually carried out in order to produce a uniform mixture and it can be achieved using mechanical mixers, fluid jet mixers, static mixer or pipe line with tees. It can be used for a variety of purposes. Examples, homogenization of physical properties and composition prevention of stratification or deposition of suspended particles, for and improved rates of heat, mass transfer and chemical reaction. Examples of mixing operations include dissolution, leaching gas, absorption, crystallization and liquid-liquid extraction. Depending on the specific application and process mixing may be done in batch wise or in continuous mode and the content may be stirred either by rotating turbines and propellers or by jets of liquid. Impellers are the conventional devices used for mixing in industries. But they are very expensive for large storage tanks and underground tanks. Jet mixers have become an alternative to impellers for over 50 years in the process industry. In jet mixing; a part of the liquid in the tank is drawn through a pump and returned as a high velocity jet through a nozzle into the tank. This jet entrains some of the surrounding liquid and creates a circulation pattern with in the vessel thus leading

to mixing of the content. In jet mixers, a fast moving jet stream of liquid is injected into a slow moving or stationary bulk liquid. The relative velocity between the jet and the bulk liquid creates a turbulent mixing layer at the jet flow, entraining and mixing the jet liquid with the bulk liquid. Jet mixers have several advantages over conventional impellers. It has no moving parts as in conventional agitators, there by reducing maintenance costs, and it is easy to install when compared with impellers. Agitators require support at the top of the tank, implying a pre-requisite for thicker walls of stronger materials. Mechanical agitators show disadvantages at an industrial scale with regard to investment and energy costs, and also sterilization and maintenance in biochemical processes and jet mixers are preferable in such situations. Jet mixers are used for the following applications. Hoffman, P.D. (1996) blending the inhibitor into the monomer storage tank to stop violent runaway exothermic polymerization reactions Fonad, C. (1993) Bio- chemical applications. Jet mixers are more appropriate for mixing processes involving chemically sensitive liquids, Rice, P. (1981) Preparation of food stuffs. The hydrodynamic characteristics of jet mixer were studied by varying nozzle diameter, jet position and fluid properties. For this purpose, the experiments were conducted in 0.5m diameter, 0.6m height column. Five different nozzles have been employed and it is optimized based on the holdup characteristics. In order to study the effect of viscosity non Newtonian fluid such as Carboxyl Methyl Cellulose (CMC), Guargum was employed.

2. Literature Review

Considerable literature and measurements on jet mixing in tanks are available. Habib, D. Z. (2006) Numerical simulation of mixing in a large horizontal cylindrical tank has shown that blending time is a function of the flow pattern generated inside the tank by the jet. Consequently the jet location is very important in determining the blending time, not so much due to its length but mainly due to the patterns of flow it creates inside the tank. A significant reduction in the values of blending time was obtained as a result of relocating the jet out let which resulted in better flow patterns inside the tank. Jayanthi, S. (2001) to find optimum shape of tank for better mixing found that conical bottom is better than hemispherical ellipsoidal, flat bottom for mixing and deeper study of the underlying hydrodynamics such as the effect of tracer diffusivity, Reynolds number, height to diameter ratio, multiple jets. VijaySarathi, J. (2008) predicted parametric Sensitivity analysis where in the effects of tank parameters. The parameters investigated were jet velocity, jet angle, location of jet, effect of hear source and tank height to diameter ratio. Kalachelvi, P. (2007) conducted experiments by varying parameters like jet diameter, jet position and jet inclination to find their effects on mixing time. The optimum angle is found to be an injection angle of 30° for jet located either at two-third of the volume of the tank or top and bottom of the tank, which gives the shortest mixing time. This optimum angle is not universal and varies with the location of the jet inlet. T.Maruyama, *et al.* (1986) to investigate systematically the effect of several geometric parametric in jet mixing in tanks using horizontal, inclined and vertical jets. They proposed that the mixing time is a function of Reynolds Number and of the largest free jet length, but also emphasized the role of the flow patterns existing inside the mixing tank on the mixing time behavior. Patwardhan, A.W. (2002) predicted mixing behavior in jet mixed tanks, mixing time and concentration profiles have been compared with the experimental measurements over a wide range of jet velocities, Nozzle angles and Nozzle diameters. Rande, V.V. (1996) predicted results of the mixing time agree with published experimental data for different jet configuration. Rakib, M.A. (2002) presented a model of Jet Mixing and validated their numerical model against the experimental results.

3. Experimental

The experimental setup is shown in Figure1. It consists of a cylindrical borosilicate glass tank of 0.5m diameter and 0.6m height in which a nozzle is installed at the centre of the tank. A pump is used to maintain a recycling condition which withdraw fluid from the storage tank and deliver it through the nozzle where the fluid is ejected to the mixing tank as a jet stream. The photographic view of experiment set up shown in the Figure 2 and the different types of nozzles are shown in Figure 3. The design details, process fluids and other parameters pertaining to jet mixer is shown in Table 1. The inlet flow rate is measured by precalibrated rotameter (35-350liter per minute) and (10-100liter per minute) respectively. The nozzle specifications and position of the nozzle are shown in Table 2 and Table 3 respectively. The fluid from storage tank is pumped in to the mixing tank through a nozzle; the output flow rate is adjusted to maintain the initial liquid holdup. After attaining the steady state the initial hold up is noted. The inlet flow rate is varied then the corresponding variations in the liquid holdup and pressure difference are noted. The effect of jet position on mixing pattern is studied by changing the clearance between the nozzle and the bottom of the mixing tank. The effect of geometrical properties on holdup is studied by changing the various diameters of nozzle and the same experimental procedure is followed.

4. Result and Discussions

4.1 Effect of Nozzle

The effect of nozzle design was studied for jet mixer having diameter (T) of 0.5m and height (H) of 0.6mm. For this purpose five different nozzles were designed and tested in the above column. In order to compare the effectiveness of the nozzle the end effect was compared based on the active area. The effect of nozzle design was compared for three different positions to ensure the reproducibility of the result. The effect of liquid flow rate on liquid holdup for different

jet position was shown in Figures 4-6. From these graph it can be seen that nozzle design having 20 % active area shows more holdup than the remaining nozzle deign. The holdup was found to decrease if the active area exceeds 20%. The holdup increases with an increase in flow rate this is due to the dependence of flow rate with the dispersed phase. On the other hand, the continuity of the dispersions process altered when the active area exceeds 15%.The travelling path of the flow was disturbed and there is formation of secondary loop which result in decrease in holdup. The effect was compared for three jet position. The same result was observed irrespective of the jet position.

4.2 Effect of Jet Position

The effect of jet was also studied for all the nozzle design. The comparison of various nozzles and their position result was given in Figure 4-6. From these graphs it can be seen that jet position of T/1.8 shows more hold up than T/2.3 and T/1.6. When the jet was located at the centre of the vessel the flow path generated by the jet nozzles will not get disturbed it takes complete radial direction and then follow axial direction and hence a complete loop was resulted. This was not happening when jet position was less or greater than the diameter of the tank.

4.3 Effect of viscosity

The effect of viscosity was carried out for the optimized nozzle design and nozzle location. In order to study the effect of viscosity test fluid namely carboxyl methyl cellulose and gaur gum were used. The concentrations of test fluid were varied in the range of 0.2 to 0.5 % (volume %). The effect of flow rate on holdup for different test fluid and various concentrations is shown in Figure 7-9. From these figures it can be seen that the holdup decrease as concentration of fluid increases. This may be due to jet velocity has to increase to retain the specified holdup. Also the flow path and circulation path is minimized when concentration of fluid is increased with respect to water.

5. Conclusion

Jet mixers can be suitably replaced in place of conventional mixers for large tanks. Among the nozzle design studied nozzle with active area of 20 % shown more holdups with less power consumption. Jet position (from bottom of the vessel) of T/1.8 shows more hold up. The power consumption increase with increase in concentration of the fluid.

Nomenclatures

C_1 = Position of nozzle, m

C_2 = Position of nozzle, m

C_3 = Position of nozzle, m

g = Acceleration due to gravity, m/s^2

H = Column height, m

h = Liquid height, m

i.d = Internal diameter of column, m

lpm = Liters per minute

N_1 = Nozzle 1

N_2 = Nozzle 2

N_3 = Nozzle 3

N_4 = Nozzle 4

N_5 = Nozzle 5

Q = Flow rate, m^3/s

T = Diameter of the column, m

T/1.6 = Jet position, m

T/1.8 = Jet position, m

T/2.3 = Jet position, m

References

Habib, D.Z. (2006). Numerical Simulation of Mixing in a Jet Agitated Horizontal Cylindrical Tank: *International Journal of Computational Fluid Dynamics* "Vol. 20." Number 2, pp 127-136.

Hoffman, P. D. (1996). Mixing in a Large Storage Tank: AICHE Symposium Series: Number 286/88/77-82.

Jayanti, S. (2001). Hydrodynamics of Jet Mixing in Vessels: *Chemical Engineering Science* 56:193-210.

- Kailas, L. Wasewar., & VijaySarathi, J. (2008). CFD Modelling and Simulation of Jet Mixed Tanks: *Engineering Application of Computational Fluid Mechanics* Vol. 2". Number 2, pp. 155-171.
- Kalaichelvi, P. (2007). Mixing Time Estimation and Analysis in a Jet Mixer: *ARPN Journal of Engineering and Applied sciences* "Vol.2". Number 55, pp 35-43.
- Lane, A.G.C., & Rice, P. (1981). An experimental investigation of jet mixing employing a vertical submerged jet: *International Chemical Engineering Symposium series* 64:K1.
- Maruyama,T., Kamishima,N., & Mizushina,T. (1986). Jet Mixing of Fluid in Tanks: *Journal of Chemical Engineering of Japan* 17:120.
- Maruyama,T., Kamishima,N., & Mizushina,T. (1986). Jet Mixing of Fluids in Vessels: *Encyclopaedia of Fluid Mechanics* "Vol. 2". Gulf Publishing Company, Houston, TX, pp. 544-562.
- Patwardhan, A.W. (2002). CFD Modelling of Jet Mixed Tanks: *Chemical Engineering Science* 57:1307-1318.
- Ranade,V.V. (1996). Towards better Mixing Protocols by designing spatially periodic Flows: The case of a jet mixer: *Chemical Engineering Division, National Chemical Laboratory* "Vol. 51". Number 11, pp. 2637-2642.
- Simon, M., & Fond, C. (1993). Experimental Study of Mixing Performance using Steady and Unsteady state Jets: *Canadian Journal of Chemical Engineering* 71: 507-503.
- Zughbi, H.D. & Rakib, M.A. (2002). Mixing in a Fluid Jet Agitated Tank: *Chemical Engineering Communication* 189:1038-1056.
- Zughbi, H.D. & Rakib, M.A. (2002). Mixing in a Fluid Jet Agitated Tank: Effect of Jet angle and elevation and number of Jets: *Chemical Engineering Science* 59:829-842.

Table 1. Jet Mixer Specification

Column Diameter, (i.d) (T)	0.5m
Column Height, (H)	0.6m
CMC Solution	0.2%, 0.3%, 0.5% (v/v %)
Gargum	0.2%,0.3% (v/v %)
Glycerol	0.5% (v/v %)
Rotameter	10-100 (lpm) 35-350 (lpm)

Table 2. Nozzle Specification

Nozzle	Active area (%)
N ₁	53.2
N ₂	29.8
N ₃	20.3
N ₄	11.4
N ₅	14.7

Table 3. Position of the Nozzle

Position 1	T/2.3
Position 2	T/1.8
Position 3	T/1.6

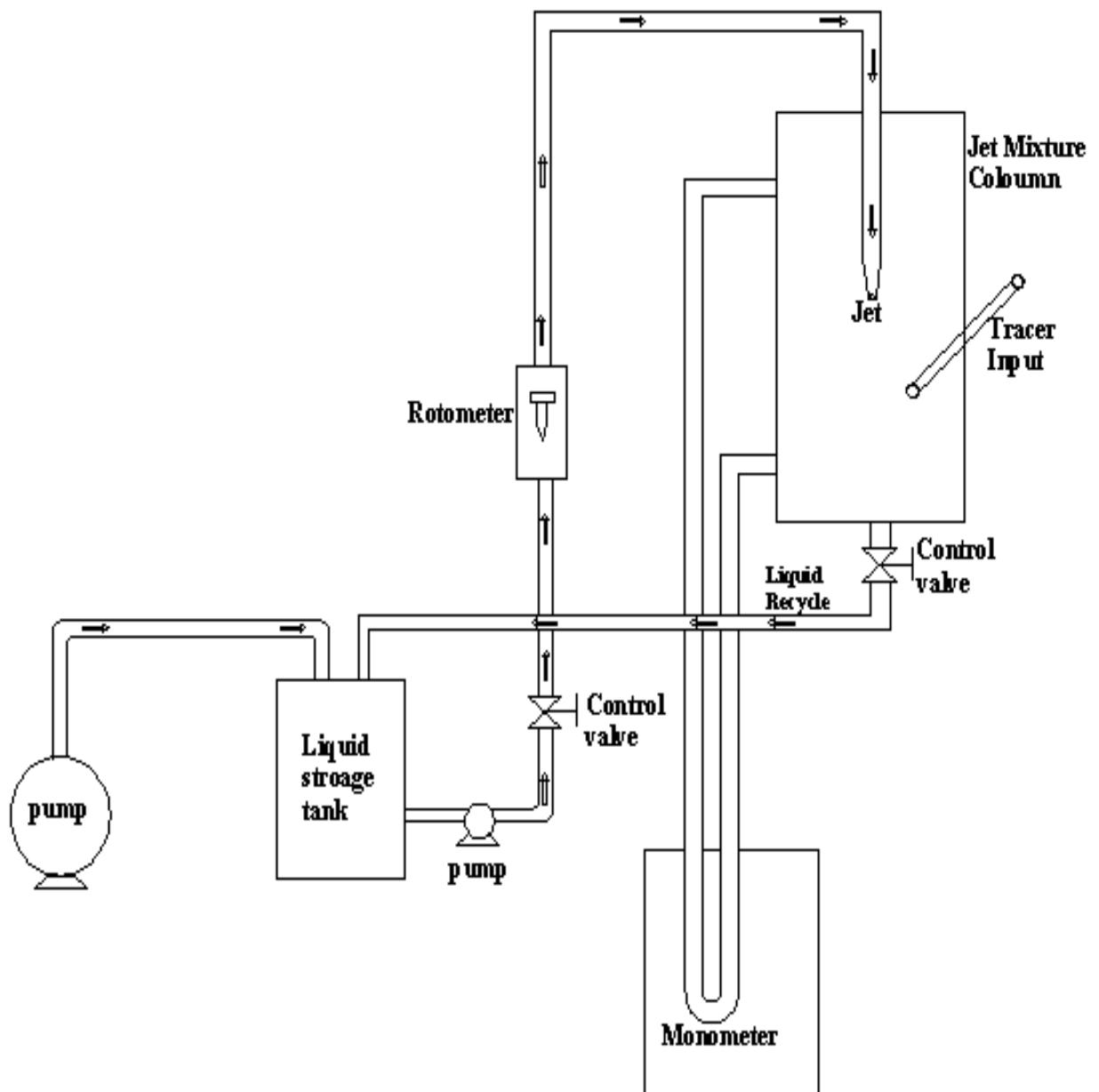
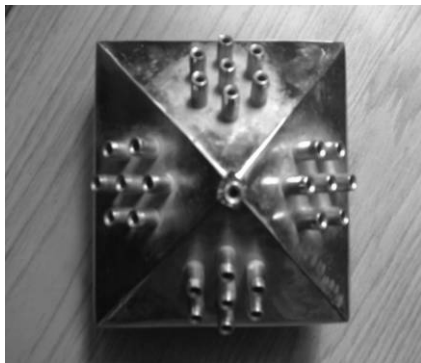


Figure 1. Experimental Set up



Figure 2. Project Equipment



Nozzle N₁



Nozzle N₂



Nozzle N₃



Nozzle N₄



Nozzle N₅

Figure 3. Types of Nozzles

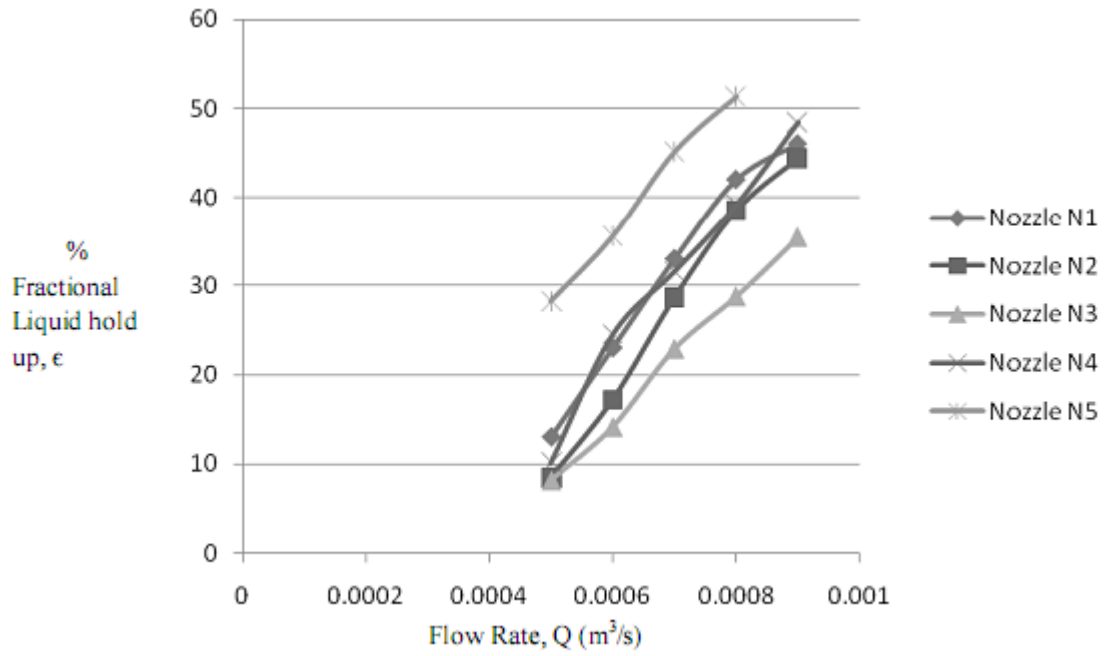


Figure 4. Comparison of various Nozzles and position for $C_1 = T/2.3$

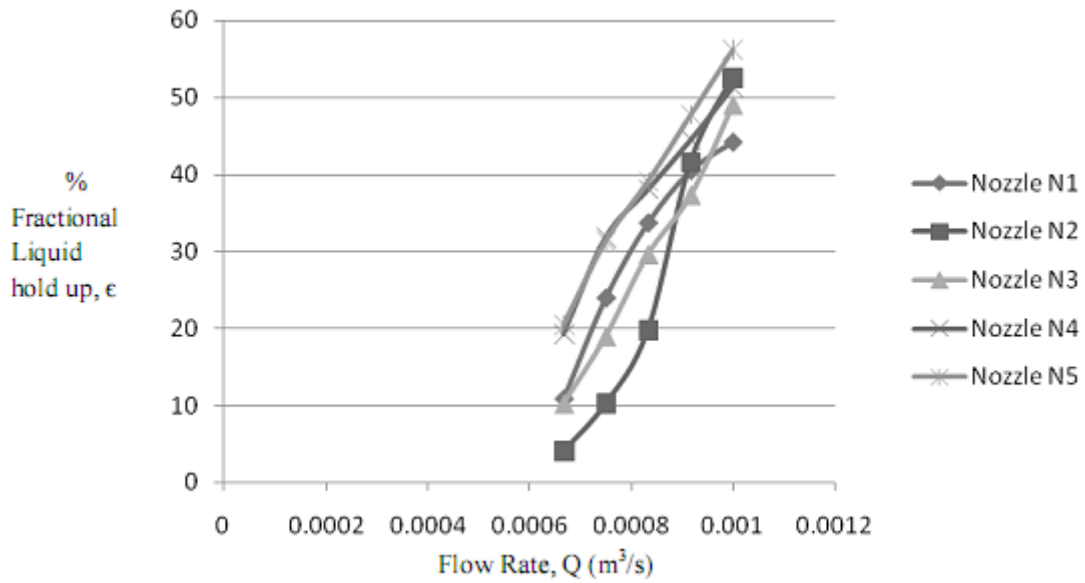


Figure 5. Comparison of various Nozzles and position for $C_2 = T/1.8$

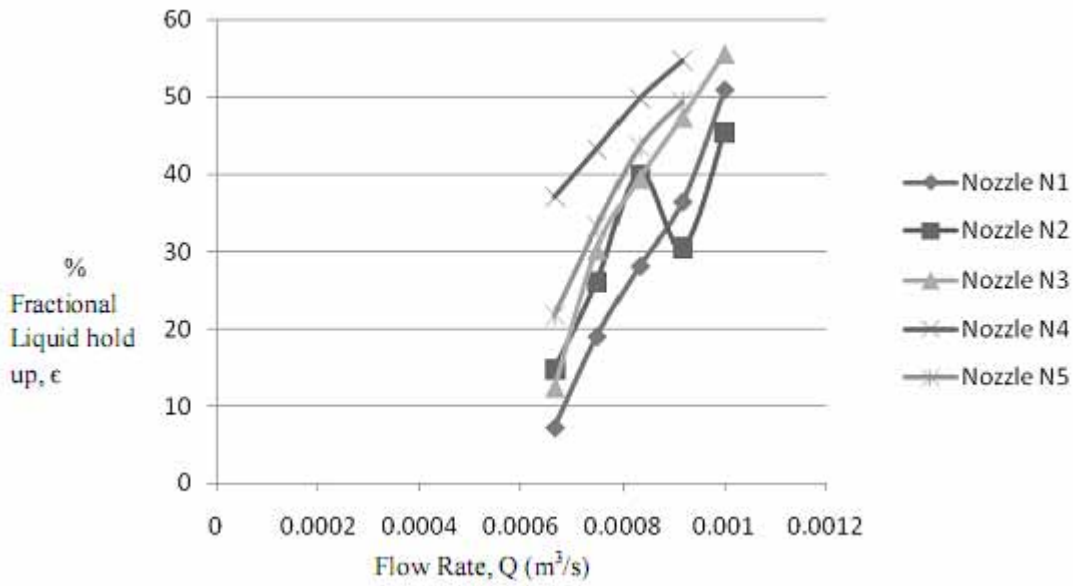


Figure 6. Comparison of various Nozzles and position for $C_3 = T/1.6$

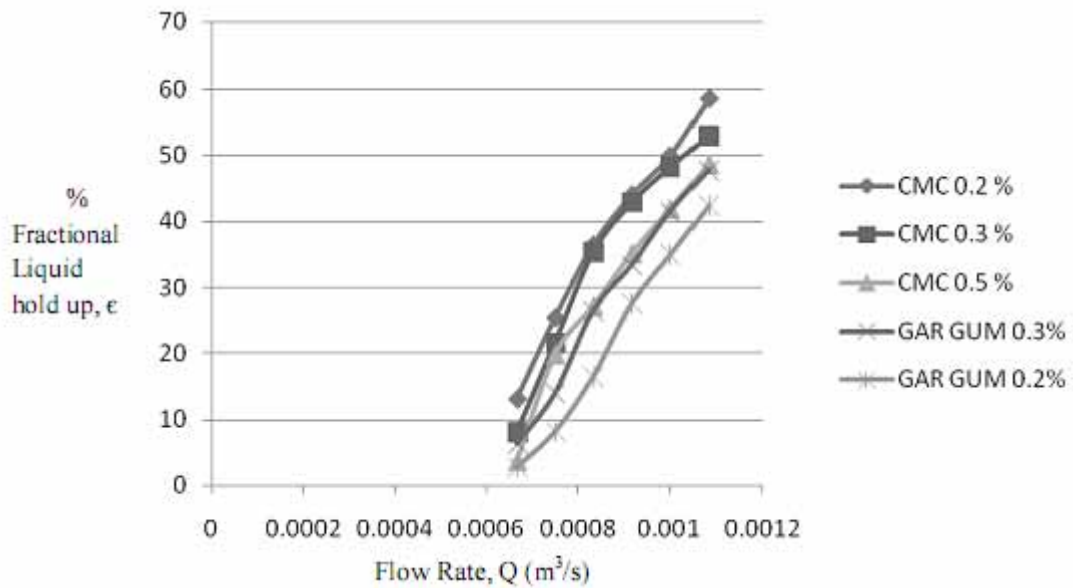


Figure 7. Effect of properties of fluids for nozzle N_3 at $C_1 = T/2.3$

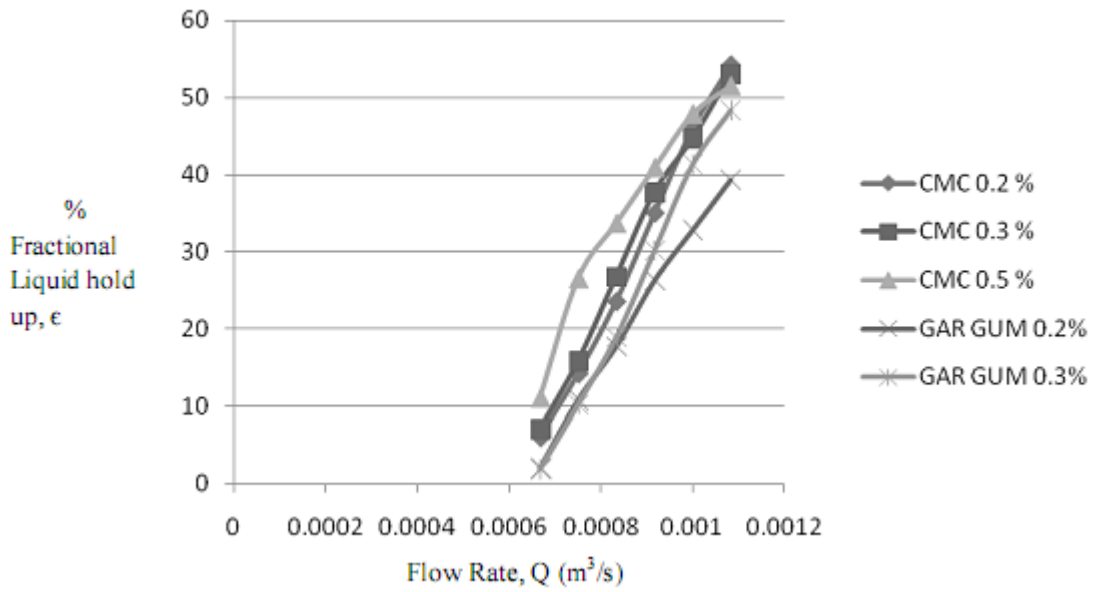


Figure 8. Effect of properties of fluids for nozzle N₃ at C₂= T/1.8

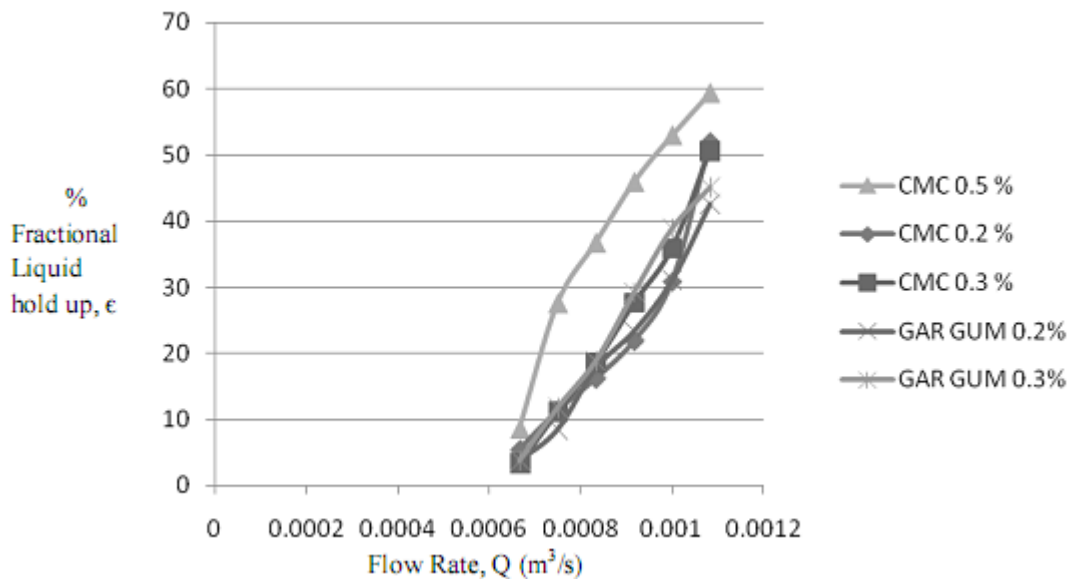


Figure 9. Effect of properties of fluids for nozzle N₃ at C₁= T/1.6



The Operator of Genetic Algorithms to Improve its Properties

Aijun Li

Information and Technology College, Tianjin University of Technology and Education

He Xi Qu Liu Lin Dong, Tianjin 300222, China

E-mail: aij_li@126.com

Abstract

Based on the traditional genetic algorithm, proposed an improved adaptive genetic algorithm, the experimental results show that the improved adaptive genetic algorithm results than standard genetic algorithm much better and effective to improve the convergence of genetic algorithm optimization of speed and efficiency.

Keywords: Genetic algorithm, Adaptive, Crossover, Mutation

1. Introduction

Genetic algorithm is a kind of bionic algorithm that simulates natural process of biological evolution developed problem-solving strategies and approaches. It has a variety of coding techniques to represent the complex structure, and through a set of codes that a simple genetic operation and survival of the fittest in natural selection to guide the study and determine the search direction. It is starting from an initial population, constantly repeat the selection, crossover and mutation process, so that more and more closer to a target population evolution.

2. Basic genetic algorithm

Basic genetic algorithm is summarized by Goldberg as a basic genetic algorithm, the genetic evolution operation formed the basis of the genetic algorithm.

3. Improved Adaptive Genetic Algorithm

Constraints in the genetic algorithm runs through the genetic operations has always been, this will certainly affect the efficiency of operations. Because as the evolution progresses, the lower the fitness of some individuals have been gradually eliminated, while the higher fitness individuals more and more, and are concentrated in the vicinity of the most advantages. The main idea of this method is the evolution of several generations in a group, it will remove the weak solution space, in the future evolution of the process with the same group size only in the strong solution space groups, breeding. You can increase the strong solution space of the individual density to improve the accuracy of solution, which helps produce excellent performance of individuals and groups likely to shorten the evolutionary process. Such adaptive genetic algorithm for optimization of complex functions; numerical results show that the method is effective and reliable.

Compared with the general genetic algorithm, adaptive genetic algorithm crossover probability and mutation probability is not a fixed value, but by groups, fitness adaptive adjustment, adaptive genetic algorithm steps:

(1) Using randomly generated N (N is even) the initial group of candidates, such as the method of solution to form the initial population.

(2) The definition of fitness function to calculate each individual's fitness f_i .

(3) In accordance with rules of roulette selection method select N individuals from the calculation, the average population fitness f_{avg} and the largest fitness f_{max} .

(4) For each individual, according to formula (1) calculate the probability of adaptive crossover P c. With Pc as the probability of crossover, that is randomly generated R (0, 1), if $R < P c$ Then the operation of the individual cross.

$$pc = \begin{cases} \frac{k_1(f_{max} - f)}{f_{max} - f_{avg}}, & f \geq f_{avg} \\ k_2, & f < f_{avg} \end{cases}$$

(5) For the group of all N individuals of, in accordance with formula (2) Calculate the probability of adaptive mutation

Pm. With mutation probability Pm is the mutation operation, that is randomly generated R (0, 1).if R< Pm Then the mutation operation on the chromosome.

$$pm = \begin{cases} \frac{k_3(f_{\max} - f')}{f_{\max} - f_{\text{avg}}}, & f \geq f_{\text{avg}} \\ k_4, & f < f_{\text{avg}} \end{cases}$$

(6) Calculated from the crossover and mutation generate a new individual's fitness, the new individual and parent groups together constitute a new generation.

(7) To determine the number of iterations to run, to meet the requirements then the optimization process is complete; otherwise transfer step (4). In equation (1), (2), f_{\max} every group of individuals on behalf of the largest fitness value; f_{avg} the average population per generation fitness value; f' is the cross of the two individuals was chosen larger fitness value; f was chosen the fitness value of individual variation. As long as the set k_2, k_4 take (0, 1) interval values, you can self-adaptive adjustment. And usually take $k_1 = 0.9, k_2 = 0.6$.

4. Analysis of experimental results

Improved adaptive genetic algorithm optimization of the maximum demand function:

$$f(x) = 10 * \sin(5 * x) + 7 * \cos(4 * x) - (x - 7)^2 + 62 \quad x \in [0, 12]$$

Set population size set to 40, respectively, the proportion of genetic operators selection, single-point crossover and single-point mutation, mutation probability of dynamic adjustment, that is, the late iterations in the algorithm increases the probability of mutation, this method can greatly to avoid early algorithm converge to a local optimal solution, the largest 300-generation evolution of algebra. The results are shown:

Standard genetic algorithm for solving the optimal value is 77.2446, run time of 5s.

Improved genetic algorithm for solving the optimal value is 78.5736, run time is 2s.

References

Hyun-ray and South Chengrun Wei, (2004). *Genetic Algorithm and Engineering Optimization*, Tsinghua University Press, Beijing.

Wang Xiaoping, Cao Liming. (2002). "genetic algorithms - theory, application and software implementation", Xi'an Jiao tong University Press, 2002, P98.

Yang Ping, ZHENG Jin-hua. (2007). *Comparison of genetic operators and research*. Computer Engineering and Applications, 2007, 43 (15):59-65.

Zhang Xiaoqin, HUANG Yu-qing. (2005). Heuristic based on tabu search algorithm for solving knapsack problem the University of *Electronic Science and Technology Journal*, 2005(3):359-362.

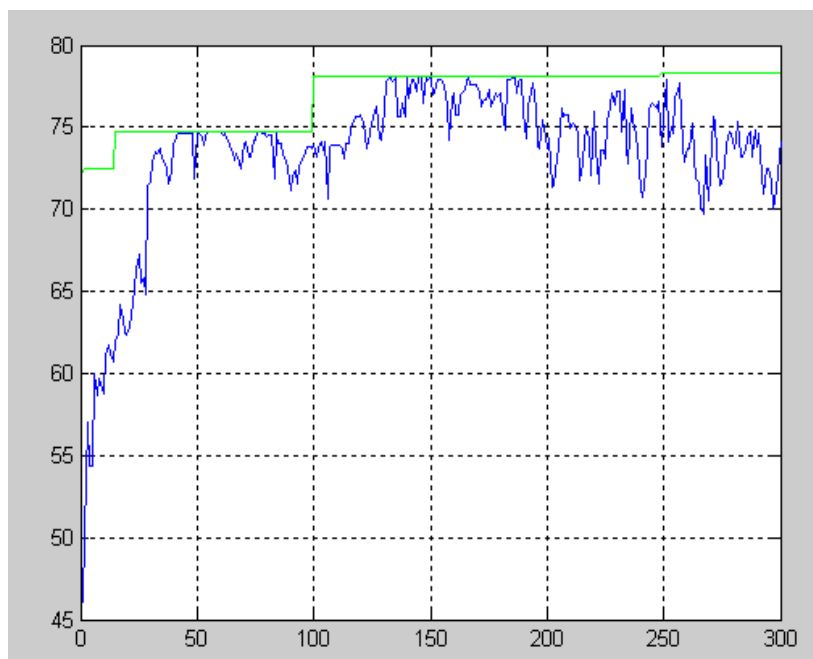


Figure 1. Adaptive Genetic Algorithm for the Traditional Result

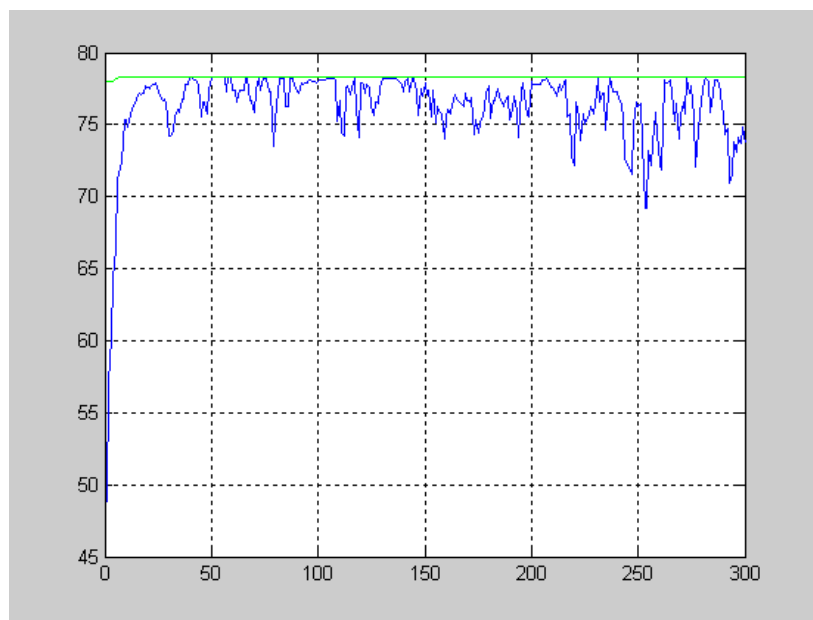


Figure 2. Improved Adaptive Genetic Algorithm Results